

https://dspace.org/

Magnetically Enhanced Vacuum Arc Thruster for Nanosatellites

Rencken, Tristan Mark

2024

University of the Witwatersrand, Johannesburg

https://hdl.handle.net/10539/46274

Rencken, Tristan Mark . (2024). Magnetically Enhanced Vacuum Arc Thruster for Nanosatellites [Master`s dissertation, University of the Witwatersrand, Johannesburg]. WIReDSpace.

Downloaded from a DSpace repository. https://dspace.org/

Magnetically Enhanced Vacuum Arc Thruster for Nanosatellites

Tristan Mark Rencken

A dissertation submitted to the Faculty of Engineering and the Built Environment, University of the Witwatersrand, Johannesburg, in fulfilment of the requirements for the degree of Master of Science in Engineering.

Johannesburg, February 2024

Declaration

I declare that this dissertation is my own, unaided work, except where otherwise acknowledged. It is being submitted for the degree of Master of Science in Engineering in the University of the Witwatersrand, Johannesburg. It has not been submitted before for any degree or examination at any other university.

Signed this 17th day of February 2024



Tristan Mark Rencken

This dissertation is dedicated to my mother and father. For their endless love, support, and encouragement

Abstract

This dissertation describes the development and testing of a magnetically-enhance Vacuum Arc Thruster (VAT) with various cathode materials and magnetic field strengths. The thruster uses a Power Processing Unit (PPU) used to generate a high-voltage spike to initiate and maintain a high current arc discharge. A multi-layer solenoid coil is placed around the arc discharge to investigate the effects of pulsed magnetic fields on the ion density distribution. The VAT produces consistent arc discharges with a peak arc current of $I_{A_{pk}} \approx 270$ A with a pulse length of $t_p \approx 3.5$ ms for three cathode materials, Fe (iron), Al (aluminium), and Cu (copper). The magnetic field generator uses a separate capacitive discharge circuit which produces field strengths between $\vec{B}$ = 0 - 250 mT along the center line of the thruster.

Research was conducted to determine the effects of applied magnetic fields to the ion density distribution of ions with the VAT plasma plume. Ion-to-arc current ratios were normalised to a baseline VAT to directly compare qualitative distributions for the various materials and magnetic field strengths. The application of a magnetic field results in the increase in peak ion-to-arc current ratios with a decrease in ion-to-arc ratios at higher angles from the center line. The increased peak and narrowing of the ion distribution suggests that the magnetic field causes ion collimation within the plasma plume.

For $0 < \vec{B} < 250$mT, performance increase over the non-magnetic case is observed with the best percentage increase in thrust factor of 16.4% for Al, 10.8% for Cu, and 6.3% for Fe, obtained at $\vec{B} \approx 150$ mT. For $\vec{B} > 150$ mT, the ion distribution is shown to result in higher ion-to-arc ratios at higher angles perpendicular to the center line resulting in greater momentum loss. The greatest thrust factor increase of Al was found to be as a result of the mass-to-charge ratio of the Al ion which is subjected to greater accelerations due to Lorentz forces. The application of an axial magnetic field was found to increase the thrust factor and result in improved VAT thrust performances.

Acknowledgements

This research was funded and supported by the SITA Aero Foundation.

I would like to express my deepest gratitude to my co-supervisor, Professor Philippe Ferrer, for his invaluable guidance, support, and mentorship throughout my master's program. His expertise, patience, and encouragement have been instrumental in the completion of my research and the writing of this thesis.

I am truly grateful for the time and effort he has invested in my academic growth, and for always being available to address my questions and concerns. His dedication to my success has been a constant source of motivation and inspiration.

I would like to extend my appreciation to Dr. Randall Paton for his guidance and input in shaping the direction of my research. Thank you, Dr. Paton, for your contribution to my academic journey.

Contents

Declaration i

Abstract iii

Acknowledgements iv

Contents v

List of Figures ix

List of Tables xiv

List of Symbols xvi

List of Acronyms xix

1 Introduction 1

1.1 Electric Propulsion in Satellites 1

1.2 Nanosatellites 2

1.3 Orbital & Alignment Mechanics 3

1.4 Electric Propulsion Modules 3

1.5 Plasma Thrusters 4

1.6 Vacuum Arc Thrusters 5

1.6.1 History of Vacuum Arc Thrusters 6

2 Research **9**

2.1 Purpose of Study 9

2.2 Problem Statement 9

2.3 Research Question 10

2.4 Research Objectives 10

3 Literature Survey **11**

3.1 Vacuum Arc Technology 11

3.2 Cathode Spot Phenomenon 12

3.3 VAT Design Theory and Performance 13

3.3.1 Power Processing Unit 18

3.3.2 Materials 19

3.3.3 Geometry 19

3.3.4 Triggering System 20

3.4 Magnetically-Enhanced VATs 21

4 Research Methodology **25**

4.1 Research Methods 25

4.2 Experimental Measurements 26

4.3 Data Capturing & Processing 26

4.4 Uncertainty Analysis 27

4.5 Data Filtering & Analysis . . . 27

5 Thruster Design **30**

5.1 Geometry Design . . . 30

5.2 Anode Material Selection . . . 32

5.3 Cathode Material Selection . . . 33

5.4 Thrust Correction Factor . . . 34

5.5 Magnetic Coil Design . . . 35

5.5.1 Plasma Shielding . . . 37

6 Experimental Apparatus & Setup **40**

6.1 Vacuum Chamber and High-Pressure Pump System . . . 40

6.2 Pulsed Power Circuit . . . 41

6.2.1 Inductor Selection . . . 43

6.2.2 Capacitor Selection . . . 44

6.2.3 Supply Voltage Selection . . . 45

6.2.4 Pulse Length Study . . . 45

6.3 Pulsed Magnetic Field Circuit . . . 48

6.4 Two-Axis Rotation System . . . 53

6.5 Thruster Positioning . . . 54

6.6 Faraday Cup Probe . . . 55

6.6.1 Background . . . 55

6.6.2 Faraday Cup Probe Setup . . . 56

6.6.3 Faraday Cup Circuit Design . . . 56

6.6.4 Faraday Cup Performance 58

7 Experimental Results **63**

7.1 Unmagnetised Ion Distribution 64

7.2 Magnetic Ion Current Density Distributions 66

7.2.1 Magnetised Fe ICDD 67

7.2.2 Magnetised Cu ICDD 68

7.2.3 Magnetised Al ICDD 69

7.2.4 Magnetic Field Performance 70

8 Discussion **73**

8.1 Baseline VAT Performance 73

8.2 Ion Current Density Distribution 73

8.3 Magnetic VAT Performance 74

8.4 Summary 76

8.5 Further Development 77

9 Conclusions **78**

A Technical Drawings **80**

B Thrust Correction Factor **85**

C Empirical VAT performance metrics **90**

References **96**

List of Figures

1.1 PhoneSat 2.5, a CubeSat built at NASA's Ames Research Center 2

1.2 Vacuum Arc Thruster plasma plume with cathode, insulator and anode in coaxial configuration. 5

3.1 Surface of Ti cathode spots obtained with SEM (Scanning Electron Microscope) with 800x magnification 12

3.2 Side and front view of the plasma arc discharge of vacuum arc produced by VAT 13

3.3 Geometry used in defining ion current distribution 15

3.4 Cosine, Gaussian and exponential distributions (**a**) Normalised angular ion density distributions for known typical VAT ICDDs. (**b**) Normalised radial ion distribution of theoretical distribution of $1/z^2$. 15

3.5 Thrust factor which corrects for plume divergence and loss of plasma to anode walls for cosine distribution and exponential distribution with spread factor $k = 4.5$ 17

3.6 Inductive Energy Storage with typical power supply, fast acting inductor, high voltage switch and VAT. The cathode is connected to ground with the anode connected to inductor. 19

3.7 Various VAT Geometries. VAT geometries are planar, tubular and coaxial from left to right. 20

3.8 VAT arc ignition method of applying graphite layer to insulator. The PPU represents the driving circuit for the VAT plasma discharge. 21

3.9 VAT with attached magnetic coil around the anode positioned near to the emission of the plasma discharge. $\vec{B_Z}$ represents the magnetic field lines produced by the magnetic foil. 22

3.10 "Photographs of the thruster plume (white region) at different magnetic induction values, red line indicate the anode plane (in Figure 3.10 (**c**) the red line is near the right edge of the image). No coil case (**a**) and two cases with assembled magnetic coil: $\vec{B}$ = 120 mT (**b**) and $\vec{B}$ = 250 mT (**c**). Blue and green lines in (**b**) represent a selected plume diameter". 23

3.11 Direct thrust measurement for single firing cycle for $\vec{B}$ = 0 mT, 70 mT, 120 mT, and 250 mT field strengths (**a**) Corrected thrust to account for drift correction (**b**) Raw thrust signals for given magnetic field strengths 23

4.1 Pico Technology Picoscope 5443D MSO data capture for all experimental tests conducted. Scope shows the signals for arc current, ion current and inductor pulse which is used to trigger the automatic saving of the data. . . 28

4.2 Gaussian-weighted moving average smoothing for arc current and raw collected data of arc current. 29

5.1 VAT concept one design with coaxial design and recessed anode edge to allow for smaller magnetic coil attachment. 31

5.2 VAT concept two design with unrecessed anode edge to allow increase mechanical strength and increase thermal conduction properties. 32

5.3 selected VAT coaxial design with inner cathode rod, ceramic alumina insulator and outer anode. UHMWPE housing with anode attached to positive terminal of PPU circuit. 33

5.4 Magnetic field on axis of current carrying loop 35

5.5 Initial simulated magnetic field results for coil design (**a**) Radial magnetic field strength of coil with 100 loops and an inner radius of 16 mm and length of 18 mm. (**b**) Magnetic field strength along the center line of the thruster with the face of the cathode found at 0 mm. 36

5.6 Peak ICDD for different coil configurations with various plasma shielding angles with $\vec{B}$ = 0 mT and peak arc current $I_{A_{pk}}$=38 A. 37

5.7 Thruster geometries of magnetic coil positioning for a coil of 20 mm length and 32 mm diameter with $\sim$ 100 turns. 38

5.8 Thruster geometries of magnetic coil positioning demonstrating the plasma shielding angle. α and β represent the maximum and minimum sight angles for the variation in arc discharge along the surface of the cathode. 38

6.1 Stainless steel vacuum chamber used for VAT testing with automated real-time data collection. 41

6.2 VAT PPU circuit diagram with power supply, capacitor, inductor, IGBT, pulse generator and VAT. 41

6.3 Arc Current for various inductors (500 μH, 900 μH, 1200 μH) with a supply voltage of 60 V. In these tests an Fe cathode was used with a 300 μF capacitor. 44

6.4 Arc Current for various capacitors (300 μH, 1000 μF, 2000 μF) with a supply voltage of 50 V. In these tests an Fe cathode was used with a 1200 μH inductor. 44

6.5 Arc Current Measurements for various supply voltages (50 V, 55 V, 60 V). These tests used an Fe cathode with a 500 μH inductor and and a 1000 μF capacitor. 45

6.6 Sample pulse length study for Al cathode VAT with an average pulse length of $t_p = 4.59 \pm 1{\times}10^{-7}$ ms. These tests used a 2000 μF capacitor, 500 μH inductor with a supply voltage of 55 V. 46

6.7 Magnetic field generator circuit with a 60 V power supply, high current IGBT and magnetic coil. 48

6.8 Search coil magnometer placed around the main magnetic coil with leads which could read the real-time induced voltage 49

6.9 Induced voltage in search coil, for a pulse length of 3 ms and various power supply voltages and currents. 50

6.10 Magnetic field strengths ($\vec{B}$) of initial field generator design, with various input voltages and currents. 50

6.11 Timing sequence of vacuum arc thruster 51

6.12 Timing sequence of vacuum arc thruster 51

6.13 TARS with stepper motor for accurate angle variation. (left) TARS with laser optical alignment system used to ensure accurate angle positioning of VAT during testing. (Lun 2015) 53

6.14 Optical Alignment System used during the experiment to vary the angle od the thrust for ICDD readings. Laser and microcontroller connected to 11 LDRs shown with LCD displaying the angle of the TARS. 54

6.15 Faraday cup set up within the vacuum chamber and engineering drawing for the design. 55

6.16 Faraday cup system set up with DC boost, Faraday cup, and shunt resistor to measure ion current for a given angle during testing. 57

6.17 Ion Current measurements for various angles from the thruster normal (0°, 15°, 30°, 45°, 60°, 75°, 90°). These tests used an Fe cathode with the selected circuit parameters for the PPU. A 750 kΩ resistor was used with a Faraday cup voltage of -250 V. 58

6.18 ICDD measurements of VAT without the magnetic coil (a) Normalised angular ion distribution with fitted theoretical distributions with the closest correlation to the cosine ICDD. (b) Normalised radial ion density distribution for various probe distances which drops according to $1/z^2$. 59

6.19 Observed ion current signals for four different shunt resistor values, these signals were processed and filtered to obtain maximum ion current values. . 61

6.20 Raw data from ion current signals for four different resistor values. 61

6.21 Various Faraday cup bias voltages between 0 - 350 V for baseline VAT with an iron cathode with a 750 kΩ shunt resistor for measurement. 62

7.1 Surface fits of ICDD data for baseline VAT operating with peak arc currents of 270 A with trend lines. (**a**) represents the surface fit for the baseline VAT without the magnetic coil attached. (**b**) represents the surface fit for the baseline VAT with the magnetic coil ($\vec{B}$ = 0 mT) to demonstrate plasma shielding. 64

7.2 Experimental results of normalised Fe ICDD with $\vec{B} = 0$ mT, $\vec{B} = 150$ mT, and $\vec{B} = 250$ mT with trend lines. 67

7.3 Experimental results of normalised Cu ICDD with $\vec{B}$ = 0 mT, $\vec{B}$ =150 mT, and $\vec{B}$ =250 mT with trend lines. 68

7.4 Experimental results of normalised Al ICDD with $\vec{B}$ =0 mT, $\vec{B}$ =150 mT, and $\vec{B}$ =250 mT with trend lines. 69

7.5 Experimental results of normalised ICDDs for Fe, Al and Cu for (**a**) $\vec{B}$ =0 mT, (**b**) $\vec{B}$ =150 mT and (**c**) $\vec{B}$ =250 mT. All results were normalised to the maximum Al unmagnetised ICDD with the magnetic coil attached with trend lines. 70

7.6 Summary of max ICDDs for Fe, Cu and Al for all magnetic field strengths and fitted slopes for each relationship. 71

B.1 Geometry used in defining ion current distribution 85

B.2 Cosine, Gaussian and exponential distributions (**a**) Normalised angular ion density distributions for known typical VAT ICDDs. (**b**) Normalised radial ion distribution of theoretical distribution of $1/z^2$. 86

B.3 Geometry used to calculate the momentum flux through the anode plane . . 87

B.4 Thrust factor which corrects for plume divergence and loss of plasma to anode walls for cosine distribution and exponential distribution with spread factor $k = 4.5$. 89

List of Tables

3.1 Examples of Spacecraft Propulsion systems performance 18

5.1 denisty $\rho\,(\mathrm{g/cm^3})$, electric conductivity $\sigma(\mathrm{MS/m})$, melting point $T_m\,(^\circ\mathrm{C})$, thermal conductivity $\lambda_T(\ \mathrm{W/(m\cdot K)})$ for potential anode selection for VAT design. 33

5.2 Ion mass M_i (AMU), Erosion rate E_r $(\mu\mathrm{g/C})$, Arc discharge voltage V_{arc} (V) and Ion velocity $v_i(\mathrm{m/s})$ for potential cathode selection for VAT design. . . . 34

6.1 VAT pulse characteristics for various cathode materials 46

6.2 Range of baseline VAT circuit parameters in initial performance testing for various circuit components 47

6.3 Magnetic field generator parameter for various input voltages and currents for final selection and application to the magnetic vacuum arc thruster 52

6.4 Surface fitting results for angular and radial ion distributions 59

7.1 The surface fitting analysis for the unmagnetised ICDD witout the magnetic coil shows the fit type, spread factors, sum of squared errors (SSE), the coefficient of determination (R^2) and the root mean square error. 64

7.2 Results of best surface analysis with peak arc current, fit type, spread factors and correlation of determination as well as thrust factor for Fe, Al, and Cu unmagnetised ICDD without the attached magnetic coil. 65

7.3 Results of best surface analysis with peak arc current, fit type, spread factors and correlation of determination as well as thrust factor for Fe, Al, and Cu unmagnetised ICDD with the attached magnetic coil. 66

7.4 Surface fitting analysis for magnetised Fe ICDD with fit type, spread factors, correlation of determination, RMSE, peak ICDD and percentage increase relative to baseline ICDD. 67

7.5 Surface fitting analysis for magnetised Cu ICDD with fit type, pread factors, correlation of determination, RMSE, peak ICDD and percentage increase relative to baseline ICDD. 68

7.6 Surface fitting analysis for magnetised Al ICDD with fit type, pread factors, correlation of determination, RMSE, peak ICDD and percentage increase relative to baseline ICDD. 69

7.7 Results of best surface analysis with peak arc current, fit type, spread factors and correlation of determination as well as thrust factor for Fe, Al, and Cu magnetised ICDD woth applied magnetic field strength of 150 mT 71

7.8 Results of best surface analysis with peak arc current, fit type, spread factors and correlation of determination as well as thrust factor for Fe, Al, and Cu magnetised ICDD with $\vec{B}$ =250 mT 72

8.1 Ion charge-to-mass ratios, ion velocity and thrust predicted performance of Vacuum Arc Thrusters. 75

C.1 Material and Arc Properties for Potential Cathode Materials 91

C.2 Material and Arc Properties for Potential Cathode Materials 92

List of Symbols

α	sight angle ($^\circ$)
$\bar{J}$	ion-to-arc charge ratio
$\bar{v}_i$	average ion ejection velocity (m/s)
$\dot{m}_i$	ion mass flow rate (μg/s)
$\dot{m}_t$	mass flow rate (μg/s)
λ_T	thermal conductivity (W/m·K)
μ_0	vacuum pereability (N·A^{-2})
Φ	magnetic flux (T)
ϕ	ion incedence angle from normal ($^\circ$)
ϕ_e	deviation of ϕ from normal ($^\circ$)
ρ	density (g/cm^3)
σ	electrical conductivity (MS/m)
$\vec{a_s}$	particle species acceleration vector (m/s^2)
$\vec{B}$	magnetic field strength vector (kg $\cdot$ s^{-2} $\cdot$ m^{-2})
$\vec{E}$	electric field strength vector (V/m)
$\vec{V}$	velocity vector (m/s)
A	area of coil (m^2)

C capacitance (F)

C_T thurst correction factor

C_T^{coil} magnetic coil thrust correction factor

e electron charge (C)

E_r erosion rate (μg/C)

F_i ion-to-total mass loss

f_i ion current fraction

f_Z single-to-total ion charge state current

g gravitation acceleration (m/s^2)

I current in coil (A)

I_A average arc current (A)

I_C average ion current (A)

I_i ion current (A)

$I_{A_{pk}}$ peak arc current (A)

$I_{C_{pk}}$ peak ion current (A)

I_{sp} specific impulse (s)

J_d arc discsharge curent (A)

J_i ion current (A)

J_Z ion current in various charge states Z (A)

k exponential distribution spread factor

L inductance (H)

l distance from thruster plume (m)

l_c	coil length (m)
m_0	initial mass of spacecraft (kg)
m_f	final mass of spacecraft (kg)
M_i	ion mass (AMU)
m_s	particle species mass (kg)
N	number of coil turns
q	particle charge (C)
Q/m	charge-to-mass ratio (C/mg)
R	shunt resistance (Ω)
r_c	coil radius (m)
r_L	Larmor radius (m)
R_o	oscillospcoe resistance (Ω)
R_{true}	true resistance (Ω)
t	time (s)
T_m	melting point ($^\circ$C)
t_p	plamsa discharge duration (s)
u_i	ion ejection velocity (m/s)
v	spacecraft velocity (m/s)
v_e	exhaust velocity (m/s)
v_i	ion velocity (m/s)
V_{arc}	arc discharge voltage (V)
V_{FC}	Faraday voltage (V)

V_{sc} search coil magnometer induced voltage (V)

w gaussian distribution spread factor

Z mean ion charge state

List of Acronyms

EMI Electromagnetic Interference

FEEP Field-Emission Electric Propulsion

ICDD Ion Current Density Distribution

IDD Ion Density Distribution

IES Inductive Energy Storage

IGBT Insulated-Gate Bipolar Transmitter

LDR Light Dependent Resistor

MEMS Micro-Electromechanical System

MPD Magnetoplasmadynamic

OAS Optical Alingment System

PPT Pulse Plasma Thruster

RMSE Root Mean Square Error

SSE Sum of Square Errors

UHMWPE Ultra-High-Molecular-Weight Polyethylene

VAT Vacuum Arc Thruster

Chapter 1 Introduction

1.1 Electric Propulsion in Satellites

The use of more sustainable methods of propulsion within the aerospace industry has been gaining attention over the past few decades. The satellite industry has traditionally been dominated by larger satellites, which are heavier, higher in power consumption, and more expensive due to material and production requirements. The introduction of lighter, cheaper materials and improved energy storage capacities has provided opportunities for both commercial and research purposes, specifically for satellites. The introduction of these new technologies has increased the demand to reduce costs and increase the reliability of satellites. A renewed focus has been placed on micro-electromechanical systems (MEMS) technologies in conjunction with light, advanced materials, energy storage capacities, and increased computer processing power. These MEMS technologies have emerged in the form of micro- and nano-class satellites.

Unlike conventional chemical systems, electrical propulsion systems such as hall and ion thrusters are lighter in weight, require fewer storage tanks and pressure valves, and are far less combustible than conventional propulsion systems. The thrust produced by an electrical propulsion system is not generated by the combustion of a propellant but by the application of electrical energy to either a liquid or solid propellant (Pietzka 2016). Electrical propulsion systems can eject propellant at up to twenty times the speed of conventional chemical propulsion systems, delivering a much greater specific impulse. Specific impulse is a definition used to quantify the effectiveness of propellant used in a propulsion system. Specific impulse is the ratio of thrust produced to the weight of the fuel consumed, which results in a much lower fuel weight requirement (Russel 2020).

1.2 Nanosatellites

The nanosat (nanosatellite) is a satellite that is loosely defined as any satellite that generally weighs less than 10 kg. The development of nanosats began in the late 1990s when engineers within the space sector began to develop a design-to-cost approach for the development of satellites within research and commercial industries (Camps 2019). An example of a nanosat is a CubeSat. A CubeSat is a satellite that is described in terms of its cubic units, called "U". A 1U CubeSat describes a 10 x 10 x 10 cm^3 cube with a total weight of around 1.33 kg.

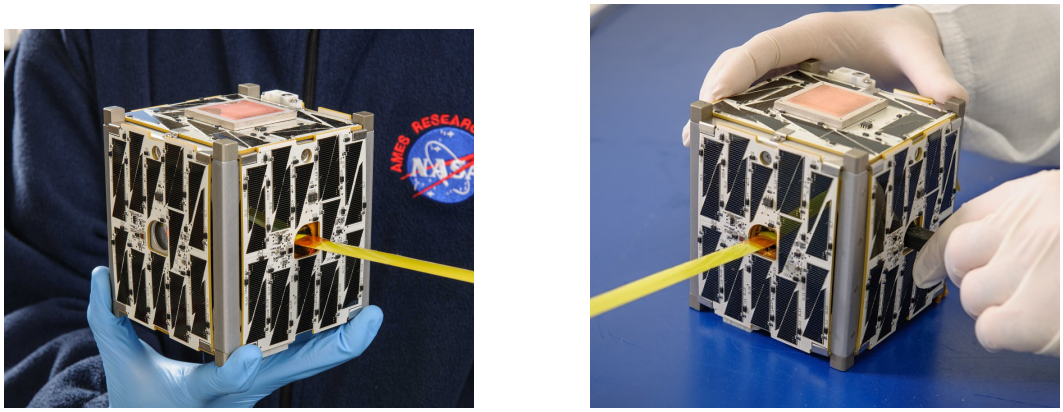

Figure 1.1: PhoneSat 2.5, a CubeSat built at NASA's Ames Research Center (Rumburg 2014)

The improvement in material and electrical technologies has allowed for these CubeSats to be built with off-the-shelf components, making them accessible to almost anyone. The availability of these components provides educators with an inexpensive means to engage with high school and university students in all phases of satellite development, operation, and utilization through hands-on research and testing experience (NASA 2018).

The main design philosophy behind the nanosat was that a smaller satellite with a single mission objective would provide a lower risk of loss or damage (Camps 2019). One important aspect of nanosats is their ability to form constellations. A constellation is defined as a group of satellites working together as a system to operate and fulfill a specified mission objective (Lee 2017). The use of constellations can be incredibly useful since the failure or loss of a single CubeSat would not have major implications on the overall constellation operation and could be replaced by a singular CubeSat.

An example of one such constellation is Spire Global's constellation with 90+ satellites. This constellation is composed of LEMUR nanosatellites, with each satellite being multi-payload and equipped with different sensors for data collection. These sensors collect global radio frequencies in near-real-time to monitor pressure, humidity, and temperature (Kulu 2023).

These data are collected from these constellations and used in weather forecasting, monitoring climate change, and space weather research, which is essential for understanding the planet's current climate issues and monitoring the development of new weather patterns. These data are essential to gaining insight into the processes contributing to climate change and how to tackle these issues ahead of time (Spire 2023).

1.3 Orbital & Alignment Mechanics

Nanosats are becoming a valuable asset to the space science community. However, due to the size and mass limitations of nanosats, there is often an associated power limitation available on-board. Nanosats with propulsion modules often have thrust vector control to ensure that the nanosat is aligned in the correct direction while the propulsion system is firing. This control typically involves gimbaling or alignment of the thrusters to correct for any errors in telemetry due to gravitational forces or orbital influences.

These tasks are completed through attitude and orbital control systems to orient the entire nanosat and alter the trajectory. Thrust vectoring is the process of changing the direction of thrust instead of the direction of the entire satellite, which is a much more direct method of control. The implementation of a lightweight singular thruster with no required pumps, valves, or mechanical actuators to vector the thrust of a nanosat would reduce the weight, complexity, and cost of each satellite.

1.4 Electric Propulsion Modules

Depending on the mission objective of the CubeSat, it can either be implemented with or without a propulsion module. A propulsion model is used for alignment, drag compensation, or speed control. Due to the size constraints of the CubeSat it is undesirable to use larger, heavier propulsion systems such as those used on larger satellites. The thrust provided by the propulsion system would need to be very small and immensely accurate due to the low weight of the CubeSat, thus making it a key aspect of CubeSat design. These levels of thrust and accuracy cannot be reached with conventional propulsive techniques (Larangot et al. 2002).

1.5 Plasma Thrusters

All plasma propulsion systems operate on the same principle. A thrust is created through the ionised plasma, which is accelerated away from the satellite. There are several types of plasma thrusters that are used:

1. Hall Thrusters: Hall thrusters are a type of electrostatic propulsion device that operates by flowing gas propellant through holes in the anode. Hall thrusters generate thrust by using an electrostatic field to accelerate ionised plasma.
2. Pulsed Plasma Thrusters (PPTs): PPTs are high-specific impulse thrusters that are generally regarded as the simplest of the plasma thrusters. PPTs generate thrust by generating a pulsed plasma discharge. These thrusters are simple and have a low thrust-to-weight ratio, which is ideal for attitude control for small adjustments in trajectory.
3. Magnetoplasmadynamic (MPD) Thrusters: MPD thrusters use electromagnetic fields to accelerate an arc discharge. These thrusters can operate at high power and provide high specific impulses; however, they are more complex and require a high level of engineering.
4. Electrothermal Thrusters: Electrothermal thrusters rely on thermal dynamics to generate thrust through the resistive heating of the propellant gas, which creates a plasma. These thrusters are simple and can produce a high level of thrust; however, they have a lower specific impulse in comparison to other plasma thrusters.
5. Field-Emission Electric Propulsion (FEEP): The FEEP thruster produces thrust through the use of a strong electric field to produce a spray of ions. FEEP is very efficient and can provide a very high specific impulse, but it is more complex than other plasma propulsion methods.
6. Electrostatic Thrusters: Electrostatic thrusters use an electrostatic field to accelerate current-carrying propellant particles to generate thrust. These thrusters are simple and can provide low to moderate levels of thrust, but they have a lower specific impulse than some other types of plasma thrusters.
7. Vacuum Arc Thruster (VAT): The VAT uses an electric discharge between two electrodes to create a high-density plasma discharge. The VAT generates thrust through the emission of an ionised plasma, which uses a solid metallic cathode as propellant. These thrusters produce precise amounts of thrust with higher specific impulses than other plasma thrusters. These thrusters are generally one of the most simple thrusters, as their operation requires only two electrodes and an insulator.

Each of these plasma propulsion methods has its advantages and disadvantages; their suitability for different space missions depends on factors such as mission duration, spacecraft size, and propulsion system requirements.

1.6 Vacuum Arc Thrusters

A specific type of electric propulsion is a Vacuum Arc Thruster (VAT). A VAT propulsion system is one that uses a vacuum arc discharge between an anode and cathode to produce thrust. The thrust is created when the arc discharge between the anode and cathode creates a high density plasma on the surface of the cathode. A plasma is produced from micrometer-sized cathode spots as the metal cathode is consumed as propellant to generate thrust.

The high power density within the regions along the cathode surface are sufficient to heat, vapourise and eject the cathode material which forms a plasma plume consisting of single and multiply charged ions. The expansion of this plasma contains ion which can travel at velocities between 10-20 km/s (Polk et al. 2008).

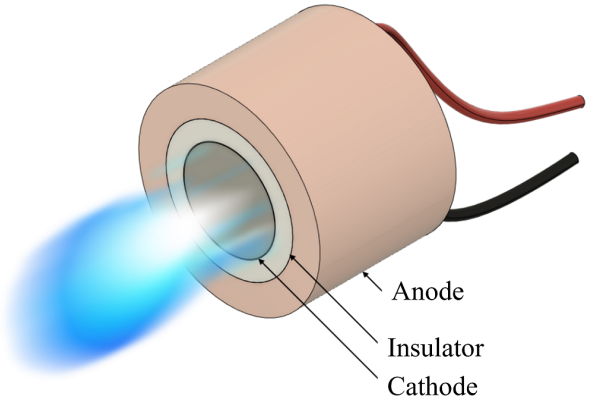

Figure 1.2: Vacuum Arc Thruster plasma plume with cathode, insulator and anode in coaxial configuration (Hiemstra 2020)

The Vacuum Arc Thruster (VAT) generates thrust through the expansion of plasma, which is fundamental to its operation (Forster, Kirner and Schein 2023). The structure of the exhaust plume is crucial to the overall propulsion performance of the VAT, as a highly divergent plume delivers less thrust than a well-directed plume. Therefore, the structure of the exhaust plume is a key issue in the performance improvement of VATs. Since the thrust is equal in magnitude and opposite in direction to the momentum flux exhausted from the system, the direct measurement of the plasma expansion can provide researchers with valuable insights into VAT performance. Several studies have been conducted to improve the performance of VATs, including the influence of external magnetic fields on the plume

(Xia et al. 2019), detailed and extensive experimental measurements of thrust, cathode erosion rate, ion current, and plasma jet, and the quantification and characterization of the plasma plume (Sekerak 2005). The plasma plume's expansion direction is normal to the cathode's surface (Hiemstra 2020). Pulsed vacuum arc thrusters are capable of efficiently producing highly ionised supersonic plasma at very low average power, making them a promising option for micro-propulsion (Kolbeck, Anders and Beilis 2019).

1.6.1 History of Vacuum Arc Thrusters

While vacuum arc thrusters (VATs) gained significant attention and development in the early 2000s, research on vacuum arc technology in the late 1980s was not focused on thrusters. The 1980s saw advancements in vacuum arc technology, which would later contribute to the development of VATs. Some of the first publications on VATs were done by Dethlefsen 1968 and Gilmour and Lockwood 1972. Their research tested a pulsed VAT with a magnetic field coil to determine the effects of axial magnetic fields on the shape of the plasma jet of the VAT. It was observed that the magnetic field could control the direction of the plasma jet.

It is important to note that the research on vacuum arc technology during the 1980s laid the foundation for the development of vacuum arc thrusters in the following decades. The advancements in vacuum arc technology, combined with the growing interest in electric propulsion for spacecraft, eventually led to the development of VATs as a promising propulsion system for micro- and nanosatellites. The research conducted between the 1960s and 1980s had little impact on the development of micropropulsion due to the inadequate power supply technology for small satellites. Studies on VATs and other electric propulsion systems did not develop until later in the twentieth century. The miniaturization of electrical components and advancements in power capacities allowed for renewed attention to the possible implementation of electric propulsion on nanosats.

The revitalisation of VAT research was a result of the collaboration between Alameda Applied Sciences Corporation (AASC), Jet Propulsion Laboratory (JPL), and Lawrence Berkeley National Laboratory (LBNL) (Qi et al. 1998, Tang et al. 2005, Polk et al. 2008). An important development made during this time was the development of the Inductive Energy Circuit (IES) (Schein, Qi et al. 2002), an innovative power processing unit with a high efficiency ($\sim$15%) propulsion system for microthrusters. The IES generates a voltage spike with an incorporated arc ignition technique (Anders 1998) and a magnetic field generator coil to collimate the ions within the plasma plume (Tang et al. 2005, Keidar et al. 2005).

In the past decade, research on vacuum arc thrusters (VATs) has focused on various aspects related to thrust performance. Some of the key developments and studies in this area include:

1. **2020 - Design, production, and validation of a VAT for in-orbit proximity operations** (Hiemstra 2020): A study focused on the design, manufacturing, assembly, and integration of a VAT into a spacecraft for in-orbit proximity operations. This research aimed to develop a VAT that could be easily integrated into small satellite systems.
2. **2021 - New concept of metal ion thruster based on pulsed thermionic vacuum arc discharge** (Velicu et al. 2021) : A study introduced the concept of pulsed thermionic vacuum arc (PTVA) to generate and accelerate metal ions without using acceleration grids. This research aimed to develop a new type of metal ion thruster based on PTVA discharge.
3. **2021 - Performance model of vacuum arc thruster with inductive energy storage circuit**(Bai et al. 2021): A study was conducted to develop a performance model for VATs that incorporated a inductive energy storage circuit. This study aimed to improve the understanding of the relationship between the design of the thruster and the operating circuit on the overall performance of the VAT.
4. **2021 - High Efficient and Reliable Vacuum Arc Thruster (HERVAT)** (Kühn, Toursel and Schein 2021): A high-efficiency and reliable VAT, known as HERVAT, was developed and tested for different pulse energies. This thruster aimed to improve the overall performance and reliability of VAT systems for small satellite applications.
5. **2022 - Time evolution of plasma parameters in the jet of a low-power VAT** (Michaux, Mazouffre and Blanchet 2022): A study investigated the time evolution of plasma parameters in the jet of a low-power VAT. This research aimed to better understand the behavior of the plasma jet and its impact on the performance of the thruster.
6. **2022 - Development of a High-Reliability Vacuum Arc Thruster System** (Kühn and Schein 2022) : A study in which researchers developed a high-reliability vacuum arc thruster system, focusing on improving the performance and reliability of VAT systems for small satellite applications.
7. **2023 - Plasma expansion characterization** (Forster, Kirner and Schein 2023): Researchers investigated the plasma expansion characteristics of a VAT using stereo imaging. This study aimed to improve the understanding of a VAT plasma expansion and the impact on overall performance.

Currently, most research is aimed at developing VATs for implementation on CubeSats, which are more efficient and require less power for continuous operation. There are many

aspects of VAT design that require further development and analysis. These practical aspects include cathode feed mechanisms, reliable triggering techniques, plasma jet collimation for increased efficiency, and extended operating lifetimes.

Chapter 2 Research

2.1 Purpose of Study

The main purpose of this study is to investigate the behavior of VAT plasma plumes under the influence of axially applied magnetic fields. This was achieved by implementing a standard coaxial Vacuum Arc Thruster with a magnetic field generator. The magnetic fields were applied over the vacuum arc discharge to investigate the influence on the angular distribution of ions ejected from the thruster. This research was done to determine: the extent to which a magnetic field manipulates the spacial distribution of charged particles within the plasma plume for different cathode materials; and to determine if the implementation of a magnetically enhanced vacuum arc thruster provides substantial improvements over standard non magnetically enhanced VATs.

2.2 Problem Statement

The thrust generated by a VAT is directly proportional to the directional momentum properties of the emitted charged particles within the plasma. Current VATs lose approximately 33% of total ion momentum due to plasma divergence (Polk et al. 2008). This occurrence is due to the angular distribution of ions ejected from the VAT. Momentum loss results in higher fuel requirements which is detrimental for longer missions.

The collimation of ejected ions can increase overall thrust and in turn lower fuel expenditure and increase the VAT life-cycle. The collimation/focusing of ejected ions is achievable through the application of an axial magnetic field along the center line of the thruster. Due to the recent focus on VAT performance improvements, it is beneficial to investigate the effects of different magnetic fields on VAT plasma plumes of various cathode materials to create more efficient and reliable propulsion methods for the future.

This investigation delves into the spatial distribution of charged particles under the influence of applied magnetic fields.

2.3 Research Question

The research and experimentation conducted will aim to answer the following:

1. How does a magnetic field affect the ion density distribution within a vacuum arc plasma?
2. How does the ion density distribution respond to applied magnetic fields for different cathode materials?

2.4 Research Objectives

The main objectives of this dissertation are to determine the relationships between:

1. The axial magnetic field strength and the spacial distribution of ions (ion density distribution) within the vacuum arc plasma plume.
2. The axial magnetic field strength and ion density distribution for cathode materials with different physical and thermophysical properties.

Chapter 3 Literature Survey

3.1 Vacuum Arc Technology

Vacuum arc technology is used today in a number of industrial applications, such as the thin film deposition of hard metal coatings for end mills and drill bits (Kolbeck, Keidar and Anders 2016). This process uses a vacuum arc discharge to liberate metal vapour from the cathode in order to deposit a coating onto another material. An additional aspect of the discharge is that this process can be used in the generation of thrust. Devices that use this form of thrust generation are called vacuum arc thrusters (VAT).

The ionized plasma created by the vacuum arc creates minuscule amounts of thrust, however the produced thrust is accurate and reliable. VATs were originally studied in the 1960-70s, and have regained attention due to the improvements in electrical and mechanical systems available to use today.

The VAT may very well be the next major step in electrical propulsion systems that drive unmanned exploration of the solar system due to the simplicity and reliability of the thruster operation (Schein, Gerhan et al. 2003). The main force behind the development of these VATs was to provide a more efficient, high thrust-to-weight ratio alternative to current Xenon-ion engines and Hall thrusters. New types of micro-thrusters could operate with efficiencies around 20%, and low total thruster and circuit mass ($<$1 kg), with a wide range of impulse bits from nN to μN (Schein, Qi et al. 2002). Scaling existing propulsion systems such as Xenon-ion engines and Hall thrusters to $\sim$1-10 W levels similar to those of VATs prove to be impractical. Scaling the required storage tanks, flow controls and plumbing for these propulsion systems directly reduce their overall efficiencies to unacceptably low levels (Schein, Gerhan et al. 2003).

These VATs have lower weight requirements due to the lack of propellant storage tanks, valves and flow controls. The low weight requirements and high thrust efficiencies make the VAT a desirable method of propulsion of nanosats.

3.2 Cathode Spot Phenomenon

The foundation of the vacuum arc is based on the cathode spot, which is the least understood aspect of all vacuum arc phenomena. The surface of both the anode and cathode have surface imperfections such as small craters, protrusions and inclusions. These imperfections amplify the local electric field which lower the work function until electrons can leave the surface by field or thermionic emission (Polk et al. 2008). The work function refers to the minimum energy needed to move an electron into vacuum.

The cathode spot is the central ejection spot of the vacuum arc plasma jet. The current carried by a single cathode spot can range anywhere from several amperes to several hundred amperes and is dependent on the cathode material. When current carried by a vacuum arc exceeds the current normally carried, the cathode spot will adapt through either, spot enlargement, division or the creation of new spots (Lafferty 2003).

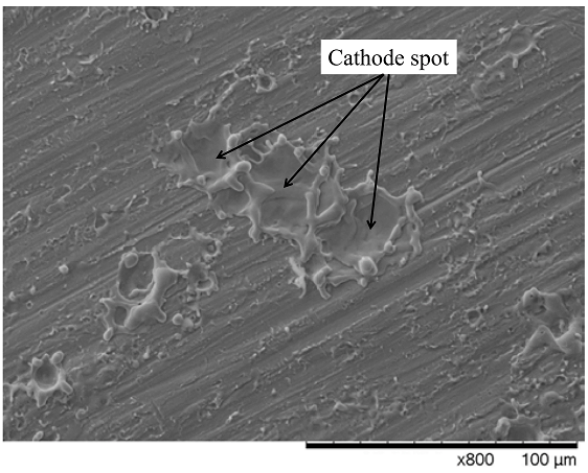

Figure 3.1: Surface of Ti cathode spots obtained with SEM (Scanning Electron Microscope) with 800x magnification (Pietzka 2016).

The high power density located at these cathode spot is sufficient to heat, vapourise and eject the cathode material which forms ionised quasi-neutral plasma consisting of single and multiply-charged ions. A portion of these ions ejected from the cathode spot return to the cathode surface, this process assists in sustaining the heating of the cathode surface which results in the re-initialization of new cathode spots until the vacuum arc is extinguished. Each arcing event results in minuscule craters left on the cathode surface which changes the cathode surface profile and leads to eventual degradation. Cathode erosion is a result of the ejection of plasma, neutrals and macroparticles. The erosion of the cathode material provides an initial conducting medium between the anode and cathode through macroparticles being redeposited onto the insulator surface between the vacuum arc electrodes.

3.3 VAT Design Theory and Performance

The VAT operation relies on a high current arc discharge between two metal electrodes, a cathode and an anode. The arc discharge between these metals is initiated by a momentary high voltage that is triggered by a PPU (Power Processing Unit). Once the arc is triggered/initiated, the high current arc vapourises and ionises the cathode material which accelerates into free space from the cathode spot in the form of a ionised plasma (Polk et al. 2008). The plasma produced from the cathode spot acts as a conducting medium to sustain the arc.

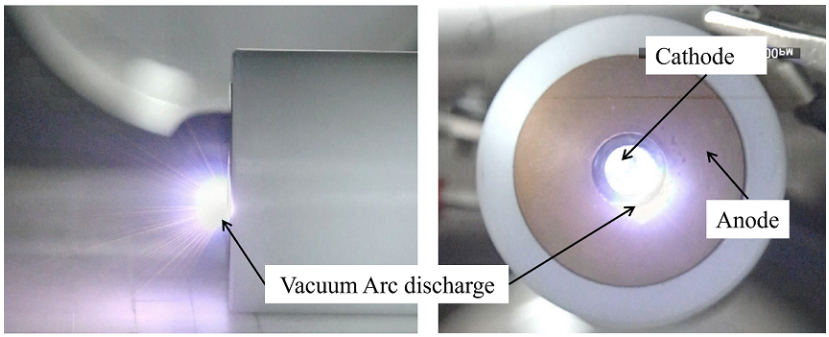

Figure 3.2: Side and front view of the plasma arc discharge of vacuum arc produced by VAT (Li, Pan and Herdrich 2020)

The acceleration of the plasma from these cathode spots results in an ejection of ions on the order of 10^4m/s (Anders and Yushkov 2002). Charged liquid macroparticles and some neutral particles are found in the emitted plasma, however the majority of the thrust is produced by the ions due to density and weight of the emitted ions. Various performance metrics such as ion density, ion velocity and ion current fraction are greatly dependent on the physical properties of the cathode material used for the thruster.

According to Polk et al. 2008, a number of VAT performance metrics could be evaluated for various cathode materials. These performance metrics were semiempirically derived through VAT experimentation for various cathode materials in an attempt to understand the operation of several implementations of VATs. These performance metrics include:

The total erosion rate $\dot{m}_t$,

$$\dot{m}_t = E_r J_d \tag{3.1}$$

which describes the total mass flow rate of for a given material specified by the erosion rate E_r. This mass is eroded from the cathode in the form of metal vapor ions, neutral vapor and macroparticles. This flow rate scales with the arc discharge current J_d.

The ion current J_i,

$$J_i = \sum_Z J_Z = f_i J_d \tag{3.2}$$

which describes the components of the total discharge current carried by the ions alone within the plasma plume. The nearly constant fraction f_i of the discharge current ranges between 0.07 and 0.1. This gives rise to the ion mass flow rate $\dot{m}_i$,

$$\dot{m}_i = \sum_Z \frac{J_Z M_i}{Ze} = \frac{f_i J_d M_i}{e} \left\langle Z^{-1} \right\rangle \tag{3.3}$$

which describes the mass flow rate of the ions alone. In the equation, e is the charge on an electron, M_i is the ion mass, and $\left\langle Z^{-1} \right\rangle$ represents the mean inverse charge state,

$$\left\langle Z^{-1} \right\rangle = \sum_Z \frac{f_Z}{Z} \tag{3.4}$$

where f_Z is the ratio of a single ion charge state to the total ion current,

$$f_Z = \frac{J_Z}{J_i} \tag{3.5}$$

These performance metrics give rise to the fraction of total mass that occurs in the form of ions F_i,

$$F_i = \frac{f_i M_i \left\langle Z^{-1} \right\rangle}{eE_r} \tag{3.6}$$

The ions are accelerated by means of gasdynamic and thermodynamic influences above the cathode spot. Previous research carried out on the measurements of the Ion Current Density Distribution (ICDD) in the plume of the expanding plasma from the cathode vacuum arc suggests that it typically follows a cosine, exponential or Gaussian distribution (Lun 2015), (Polk et al. 2008). An expression for the ion density at a radius l and angle ϕ from the surface normal due to the mass generated in area dA_1 in the cathode surface can be described in polar coordinates based on Figure 3.3, and by the distribution functions, shown by Equations 3.7, 3.8, and 3.9.

Exponential distribution (Polk et al. 2008):

$$j_{ip}(l, \phi) = \frac{j_{ic} 2 dA_1}{\sqrt{\pi} l^2 k \operatorname{erf}(2\pi/k)} \exp(-[2\pi(1 - \cos\phi)]^2/k^2) \tag{3.7}$$

Gaussian distribution (Lun 2015):

$$j_{ip}(l,\phi) = \frac{j_{ic}dA_1}{\pi l^2}\exp\left(-\frac{\phi^2}{2w^2}\right) \tag{3.8}$$

Cosine distribution (Polk et al. 2008):

$$j_{ip}(l,\phi) = \frac{\cos\phi}{\pi l^2} j_{ic}dA_1 \tag{3.9}$$

These distributions represent the angular and radial ion density distribution based on the geometry in Figure 3.3, and result in the normalised distributions shown in Figures 3.4a and 3.4b.

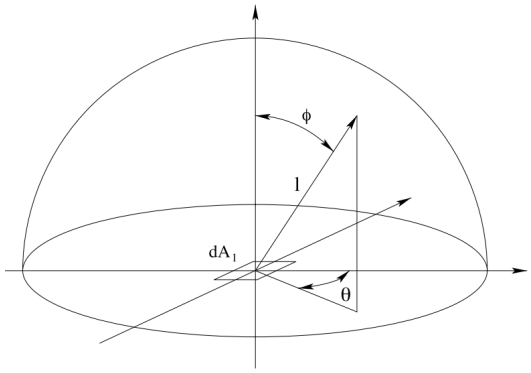

Figure 3.3: Geometry used in defining ion current distribution (Polk et al. 2008)

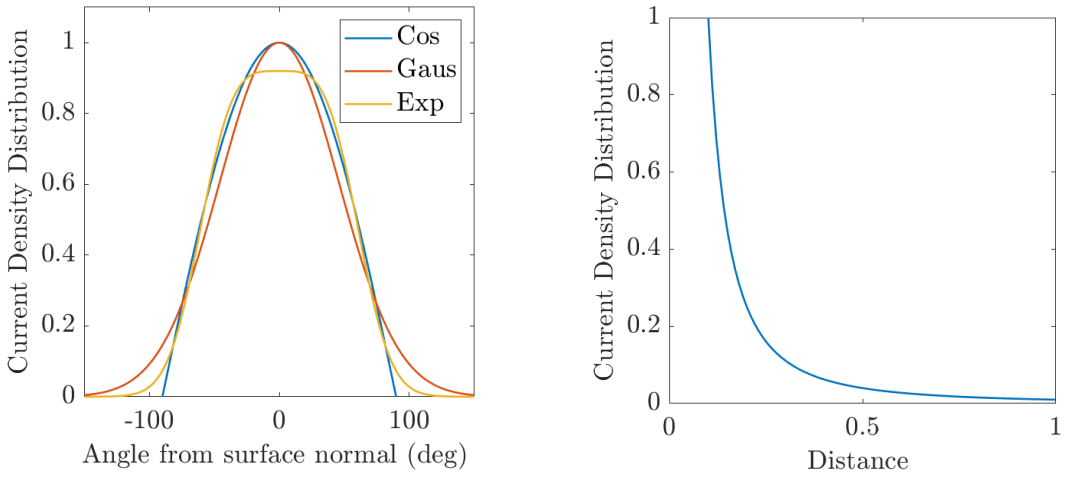

(a) **(b)**

Figure 3.4: Cosine, Gaussian and exponential distributions (**a**) Normalised angular ion density distributions for known typical VAT ICDDs. (**b**) Normalised radial ion distribution of theoretical distribution of $1/z^2$.

These functions have been normalised in order to present the shape of the distribution rather than the actual distribution of the ion density as this is dependent on a number of physical properties in experimentation. These functions were thus normalised to a value of $j_{ic} dA_1 = 1$.

With the assumption above and ion current distributions, the ion mass flow at the point (l, ϕ) can be expressed as:

$$\dot{m}_{ip}(l, \phi) = \frac{M_i j_{ip}}{e} \left\langle Z^{-1} \right\rangle \tag{3.10}$$

The thrust for a specified distribution function can thus be determine by integrating the momentum flux through the face of the anode plane. The differential thrust due to ion flux through dA_2 at the anode exit pane is given by:

$$\begin{aligned} dT &= d\dot{m}_{ip}(l, \phi) \left(u_i \cos\phi\right) \left(\cos\phi dA_2\right) \\ &= \frac{M_i j_{ip}}{e} \left\langle Z^{-1} \right\rangle u_i \cos^2\phi dA_2. \end{aligned} \tag{3.11}$$

where dA_2 is the differential area over the the anode exit plane. Integrating over the cathode surface and anode exit plane, results in the expression,

$$T = \frac{M_i f_i J_d u_i}{e} \left\langle Z^{-1} \right\rangle C_t \tag{3.12}$$

which can be simplified to,

$$T = C_T \dot{m}_i \bar{v}_i = C_T \left(m_i \frac{I_i}{e\bar{Z}} \right) \bar{v}_i \tag{3.13}$$

which represents the thrust produced by the ions through the anode plane with a velocity of u_i directed along the normal, and $\bar{v}_i$, the average ion ejection velocity and the thrust correction factor C_T. The thrust factor is used to account for plume divergence and the deposition of the eroded cathode material on the inner anode walls. The derivation for C_T can be found in Appendix B. The momentum flux that travels through the anode plane can be represented by the length of extended anode to the cathode radius. This can be shown in Figure 3.5. This relationship can be used in the initial design process of VAT thrusters to evaluate thrust characteristics for cathode erosion.

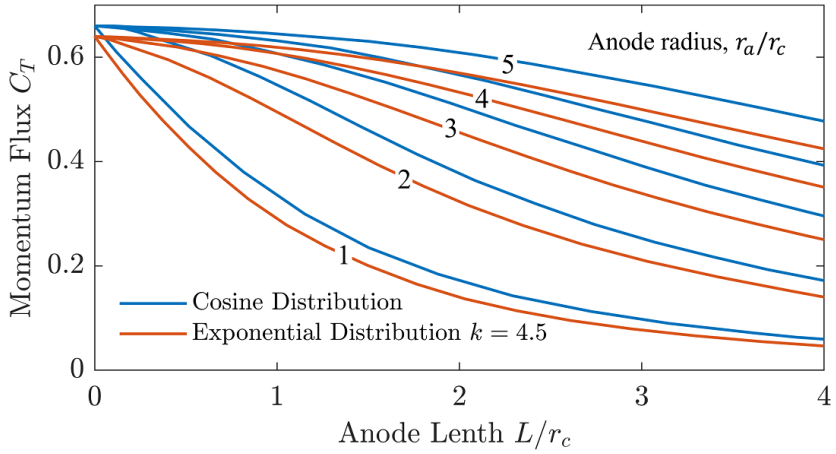

Figure 3.5: Thrust factor which corrects for plume divergence and loss of plasma to anode walls for cosine distribution and exponential distribution with spread factor $k = 4.5$. (Polk et al. 2008)

Given the above semiempirical performance metrics, the specific impulse of the VAT is then given by,

$$\begin{aligned} I_{sp} &= \frac{T}{\dot{m}_t g} = \frac{M_i f_i u_i C_t}{e E_r g} \left\langle Z^{-1} \right\rangle \\ &= \frac{F_i u_i C_t}{g} \end{aligned} \tag{3.14}$$

It is possible to examine the ideal rocket equation for electrical propulsion which is the modified version of the traditional rocket equation (Tsiolkovsky 1903). This demonstrates the advantage of using electric propulsion systems such as VATs for nanosats.

$$\Delta v = v_e \cdot \ln\left(\frac{m_0}{m_f}\right) \tag{3.15}$$

$$v_e = I_{sp} \cdot g \tag{3.16}$$

where Δv is the change in velocity of the spacecraft in m/s, I_{sp} is the specific impulse of the electric propulsion system in seconds, g is the acceleration due to gravity (9.81 m/s^2), v_e is the exhaust velocity in m/s, m_0 is the initial mass of the spacecraft with fuel and payload, and m_f is the final mass of the spacecraft after fuel consumption.

The specific impulse is a measure of how efficiently an engine creates thrust, which is typically a lot higher for electric propulsion systems than combustion engines. This is because electric propulsion systems accelerate their propellant using electric or magnetic fields,

which can produce much higher exhaust velocities than can be achieved with chemical reactions. Table 3.1 present examples of space craft engines and their specific impulses.

Table 3.1: Examples of Spacecraft Propulsion systems performance (Henry et al. 1995)

Engine	I_{sp} (sec)	Thrust (N)	Duration
Chemical		0.1 – 1.2×10^7	minutes
Liquid			
Monopropellent	140-235		
Bipropellent	320-460		
Solid	260-300		
Hybrid	290-350		
Electric		0.0001 – 20	months – years
Electrothermal	500-1000		
Electromagnetic	1000-7000		
Electrostatic	2000-10000		

The ideal rocket equation is widely used in propulsion engineering, as it allows for engineers to determine the necessary propellant mass and initial satellite mass required to achieve certain velocity changes.

The use of electric propulsion is constraint by application. The inertia of larger spacecraft render electric propulsion techniques less effective. Currently, the use of electric propulsion is limited to application on nanosats and thus is not applicable to spacecraft designed for operation with larger onboard manifest such as humans, or large equipment.

3.3.1 Power Processing Unit

The Power Processing Unit (PPU) is the circuit used in driving the high current discharge of the vacuum arc thruster. In order to reach power high enough to trigger and sustain an arc discharge between the electrodes, an efficient pulsed power supply needs to be used. This is also used in order to reduce the average power requirements of the overall circuit. Schein, Qi et al. 2002 designed a simple and efficient PPU which can pulse a voltage in the range of kiloVolts (kV) and a current which can sustain an arc for several hundred microseconds (μs) from an input voltage of around 15 - 30 V. This is the Inductive Energy Storage (IES) circuit which is most commonly used today.

As can be seen in Figure 3.6, the circuit consists of a standard power supply, fast-acting inductor, and a high voltage switch (IGBT). The VAT design is an efficient electric propulsion system that in combination with the PPU results in a low-mass system ($<$ 300g).

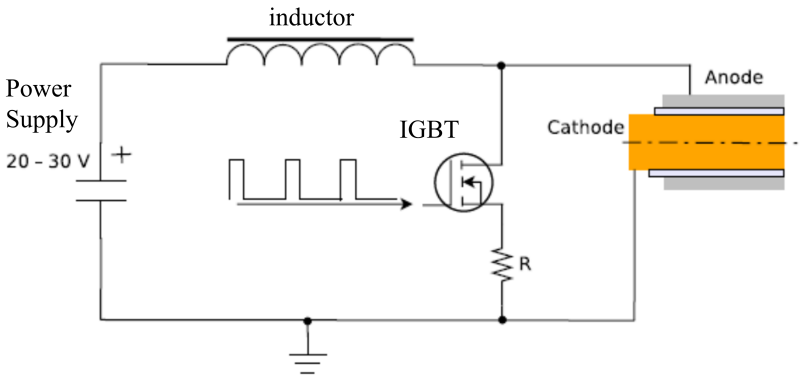

Figure 3.6: Inductive Energy Storage with typical power supply, fast acting inductor, high voltage switch and VAT (Schein, Qi et al. 2002). The cathode is connected to ground with the anode connected to inductor.

3.3.2 Materials

A unique aspect of VATs is the selection of materials for the anode, cathode and insulator. The basic operation of the VAT can be performed with any conducting electrodes insulated by any material with high electrical resistivity (100Ω - 1MΩ) (Schein, Qi et al. 2002). It was found that the cathode materials with the best overall performance were magnesium, chromium, yttrium, tantalum and tungsten (Polk et al. 2008).

It was noticed in the early 1960s that the material of the cathode drastically affects the performance of the VAT, however, deciding on the specific material has been challenging as each material has a unique combination of thermophysical and electrical properties. Given that VATs can use any conductive material as a fuel source, metal is the most suitable for use a propellant, as metal has a high density, good thermal and electrical conductivity properties, high melting point and high boiling points. These material properties allow for good plasma conduction and erosion properties which ensure long life-cycle performance.

3.3.3 Geometry

When considering the design and manufacturing of a VAT, an important aspect to take into account is the geometry. The most common geometries being the planar, coaxial and tubular design, each with their own advantages.

The advantage of a coaxial design is the well defined location of plasma production resulting in a more accurate and reliable thrust vector. It was found that a design with flush electrode faces resulted in the optimal thrust as there was no intercepting surface for the

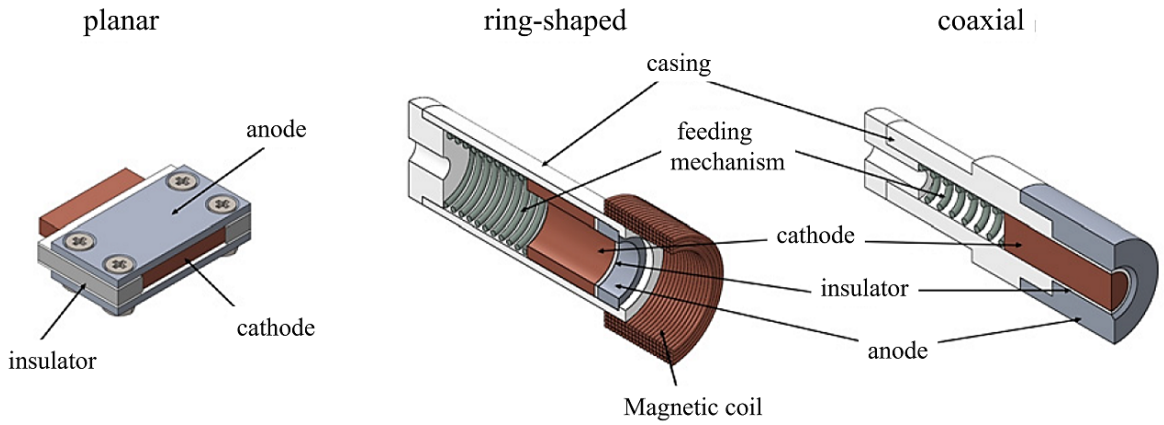

Figure 3.7: Various VAT Geometries (Pietzka 2016) VAT geometries are planar, tubular and coaxial from left to right.

plasma plume (Polk et al. 2008). This design however can have a more complex manufacturing process requirement for the electrodes as well as the insulator. This problem is not as predominant with the planar design.

The planar design has a much simpler design, however results in inaccurate prediction of the location of the plasma and thrust position along the cathode. In the early 2000s a design was proposed by Schein, Zierhut et al. 2007, a ring-shaped geometry where hollow rings of the anode, cathode and insulator were placed together to make a tube. It was found that this design was more reliable due to the ease of metal deposition on the insulator during triggering. Despite the improved reliability of this design, it was essential that the thrust operated with an external magnetic field in order to guide the plasma co-axially to the tube and produce thrust.

3.3.4 Triggering System

Triggering is done to initiate the arc between electrodes for each consecutive pulse. The process of triggering is carried out by providing a path of low resistance between the anode and cathode momentarily, allowing an electrical connection between the anode and electrode to be established. Once the high current travels along the low resistive path from the anode to cathode, connection is sustained by the vacuum arc discharge for a finite number of thruster pulses. This arc ignition or triggering can be done in a number of different ways, such as high-voltage breakdown, fuse wire explosions, contact separation, mechanical triggering and many others. The most common and reliable method of triggering used is by short circuiting the electrodes with a thin conductive layer which burns up during initiation.

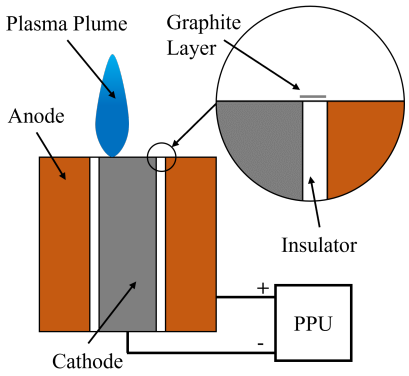

Figure 3.8: VAT arc ignition method of applying graphite layer to insulator. The PPU represents the driving circuit for the VAT plasma discharge.

A thin conducting layer on the surface of the insulator provides a momentary path of low resistance for the arc ignition. When a relatively low voltage of several hundred volts is applied between the electrodes, breakdown occurs at minuscule imperfections along the conduction surface. These tiny discharges create enough metal vapor to initiate a larger arc discharge. Once the main arc has been initiated, the metal vapor and droplets released from the cathode redeposit on the insulator surface and thus replenishing the conductive layer. The most common method of applying the initial conductive layer to the insulator is by using a pencil to deposit a layer of graphite over the insulator, then applying acetone to the graphite to evenly distribute the graphite over the surface (Sekerak 2005).

There are many practical aspects of the VAT operation that require further attention. One aspect being the method of reliable arc triggering without the requirement of applying a graphite layer to the insulator manually. Alternative methods of arc triggering include mechanical triggering, laser ablation and gas ignition (Anders 1998). These methods, are either too complex for the scope of this research or result in too few pulses ($\sim$1000) being produced for continuous experimental testing.

3.4 Magnetically-Enhanced VATs

The emergence of new development of micro-thrusters has led to the introduction to a variety of VAT device designs, one of which is known as the Magnetically-Enhanced Vacuum Arc Thruster (MEVAT). The MEVAT adapted original VAT technology by adding an external axial magnetic field. The magnetic field is generated by a coil which is placed around the cathode where the plasma is produced. MEVATs have several advantages over

other electric propulsion systems, including high thrust-to-power ratio, high specific impulse, and the ability to operate at higher power levels. They are also simple and compact, making them suitable for use in small spacecraft.

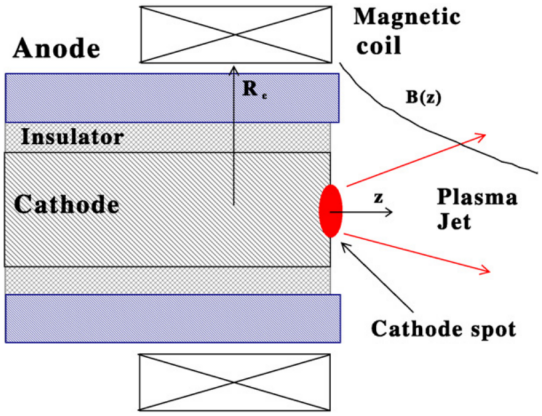

Figure 3.9: VAT with attached magnetic coil around the anode positioned near to the emission of the plasma discharge. (Keidar et al. 2005) $\vec{B_Z}$ represents the magnetic field lines produced by the magnetic foil.

A magnetised plasma is a plasma which is subjected to an ambient magnetic field strong enough to alter the trajectories of the particles. The electric field produced by a magnetised plasma with a mean velocity of $\vec{V}$ can be expressed as:

$$\vec{E} = -\vec{V} \times \vec{B} \tag{3.17}$$

The motion of electrons and ions are determined by the electric and magnetic fields, but also change the fields by the current they carry. If the fields are assumed to be prescribed and that the charged particles have negligible effect on the electromagnetic fields, the motion of the particles can be expressed as:

$$m_s \frac{d\vec{v}}{dt} = q(\vec{E} + \vec{v} \times \vec{B}) \tag{3.18}$$

$$\vec{a_s} = \frac{d\vec{v}}{dt} = Q/m(\vec{E}) + Q/m(\vec{v} \times \vec{B}) \tag{3.19}$$

This expression describes the motion of a charged particle due to the Lorentz force. The Lorentz force is the combined force applied to a particle due to both electric and magnetic fields.

When considering the electric force alone, the direction of the applied electric force on the charged particle is in the direction of the electric field, and thus does work and alters the

magnitude of the particle velocity. The magnetic force is perpendicular to the velocity of the particle, and thus no work is done and the magnitude of the particle velocity remains unchanged, however the direction of momentum does change. The magnetic force applied to a charge particle results in a circular motion with a radius expressed as:

$$r_L = \frac{m_s v_\perp}{qB} \tag{3.20}$$

This motion of charged particles in magnetic fields is important in many areas of physics, including particle accelerators, magnetic nozzles, space plasmas, and plasma propulsion for spaceflight. One example of this was the application of a magnetic nozzle to a VAT by Chowdhury and Kronhaus 2020.

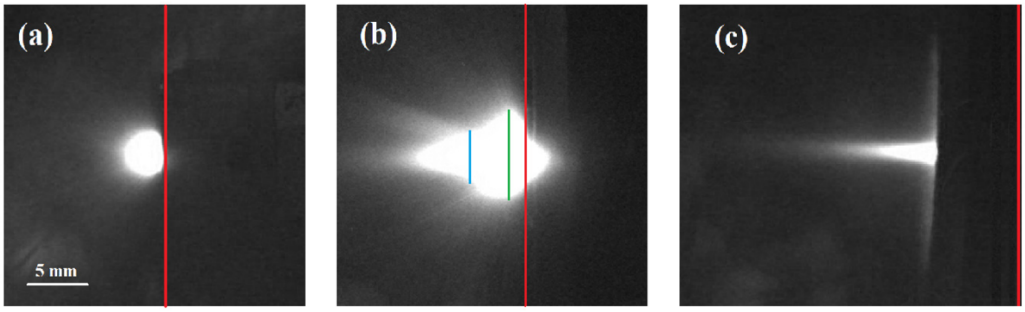

Figure 3.10: "Photographs of the thruster plume (white region) at different magnetic induction values, red line indicate the anode plane (in Figure 3.10 (**c**) the red line is near the right edge of the image). No coil case (**a**) and two cases with assembled magnetic coil: $\vec{B} = 120$ mT (**b**) and $\vec{B} = 250$ mT (**c**). Blue and green lines in (**b**) represent a selected plume diameter" (Chowdhury and Kronhaus 2020).

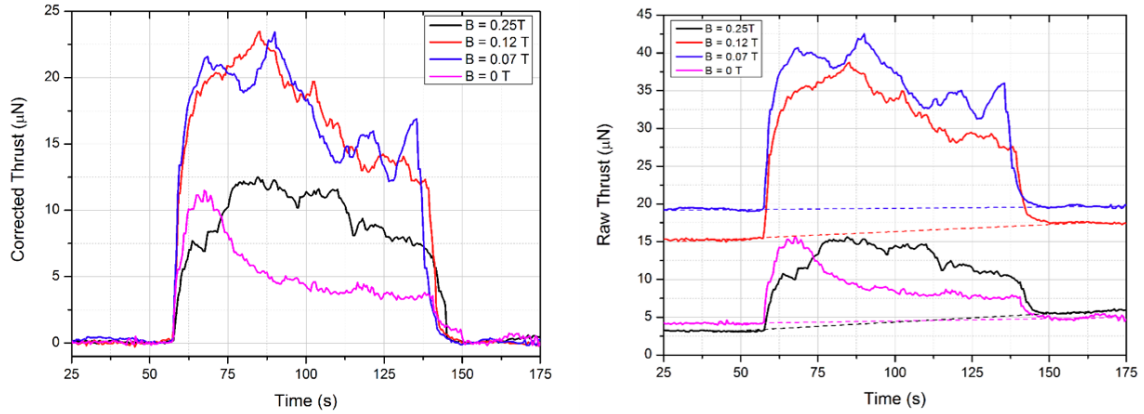

(a) **(b)**

Figure 3.11: Direct thrust measurement for single firing cycle for $\vec{B} = 0$ mT, 70 mT, 120 mT, and 250 mT field strengths (**a**) Corrected thrust to account for drift correction (**b**) Raw thrust signals for given magnetic field strengths (Chowdhury and Kronhaus 2020).

An externally applied magnetic field collimates and accelerates the plasma from the surface of the cathode, and in turn increases the overall thrust and decreases the contamination of the spacecrafts surfaces. Surface contamination occurs due to the backflux of ions and neutrals that condense onto the surface of the satellite (Kolbeck, Keidar and Anders 2016). This is especially detrimental for satellites with optical and sensitive electronics such as solar panels. It was found that the implementation of an external axial magnetic field increased the plasma collimation which has numerous implications (Zhuang, Shashurin, Denz et al. 2009). The collimation of the plasma plume reduces the possible contamination of onboard sensors, increased ion velocity and increased ion current.

Research conducted by (Kronhaus, Chowdhury and Laterza 2019) showed that there is a substantial performance improvement over the non-magnetic VATs due to the application of an external, axial magnetic field. This application resulted in the thrust-to-weight ratio of the their particular thruster doubling, enabling the a thrust generation of 21 μN at 2.7 W of average arc power and a 4% thrust efficiency. The maximum thrust improvement was observed with a magnetic field strength of $\vec{B} = 0.12$ T with substantially lower values measured at either lower or higher magnetic field strengths. However, the greatest increase in thrust was within a magnetic field range $\vec{B} \approx 0 - 0.04$ T (Kronhaus, Chowdhury and Laterza 2019). In addition, a magnetic field applied to the VAT leads to better cathode erosion rates and cathode spot rotation which, in turn leads to homogeneous erosion critical for thruster life-cycle performance (Zhuang, Shashurin, Brieda et al. 2009).

Recent research by Keidar's group at George Washington University (GWU) has indeed highlighted the impact of an external magnetic field on the burning arc voltage in vacuum arc thrusters (VATs). The presence of an external magnetic field can result in a higher burning arc voltage, leading to increased power consumption in VATs (Almurr et al. 2022).

While mentioning the benefits of magnetically enhanced vacuum arc thrusters (MEVATs) in terms of plasma focusing and acceleration, it is essential to consider the trade-off between the performance improvements and the increased power consumption due to the higher burning arc voltage. This aspect should be taken into account when designing and optimizing MEVATs for various applications.

Further research and development in this area can help strike a balance between the performance gains provided by the magnetic field and the associated increase in power consumption. This will be crucial for optimizing the design and performance of MEVATs for micro- and nano-satellite applications.

Chapter 4 Research Methodology

The primary objective of this dissertation was to identify the effect of applied magnetic fields on the performance of a VAT. To complete this objective, a VAT was built and tested in a vacuum chamber, with the appropriate instrumentation and boundary conditions. The experimentation was conducted at the Wits Space Propulsion (Plasma) Lab. The instrumentation needed for VAT testing was built by the Wits Engineering and Physics departments and was readily available for calibration and set up. This provided insight into how magnetic fields influence the overall thrust of a VAT, and whether this could be applied to current nanosat designs.

Disclaimer: The materials and methods used in this dissertation were constrained by limited time and the effects of COVID-19 on the availability of materials, parts, and diagnostic tools. As a result, some of the materials and methods may not be optimal. Nevertheless, all efforts were made to use the most available and appropriate resources.

4.1 Research Methods

When considering the properties of VAT designs, it is generally difficult to measure the plasma properties close to the cathode spot due to the intense conditions and the size of the plasma, however the plasma distribution surrounding the cathode spot can be measured using a Faraday cup (particle counter), which provides significant insight into the ion density distribution of the plasma. The experimentation was conducted with the use of a baseline thruster, vacuum chamber, power processing unit, and measurement instrumentation. To ensure repeatability, the baseline thruster had the same design as the majority of VATs found in literature, and had modular features to allow for easy replacement of components.

4.2 Experimental Measurements

In order to determine the performance of various cathode materials with an applied axial magnetic field, specific measurements were taken during each test. These measurements being: arc current; ion current and magnetic field strength at the plasma plume. Circuit diagnostics include a shunt resistor on the anode side of the VAT in order to measure the arc current. Additionally, a search coil magnometer was placed within the magnetic field generator to measure the induced voltage caused by the pulsed magnetic field. The ion current was measured with the use of a Faraday cup Probe, which is used to measure the ion current at various angles about the plasma plume. These voltage signals were sent to a high-speed digital oscilloscope which automatically saved each signal when triggered by the pulse send to the insulated-gate bipolar transistor (IGBT). The IGBT is used to accurately control the charging and discharge of the vacuum arc discharge during operation.

4.3 Data Capturing & Processing

The arc current, ion current and magnetic field strength measurements were captured by a digital oscilloscope. Once the raw data were captured, further processing was performed in MATLAB to display the results in a concise format and to extract key parameters for each configuration of the vacuum arc thruster with an applied magnetic field.

1. Arc current (I_A), the arc current measurement. The arc current measures the current carried through the plasma. This measurement is directly proportional to the amount of ions emitted by the plasma plume (Polk et al. 2008).
2. Peak arc current ($I_{A_{pk}}$), the maximum arc current of the plasma discharge.
3. Ion current (I_i), the ion current measurement. The ion current is the current carried by the ions through a specific plane. In this research the ion current is measured with the Faraday Probe which provides a measure to how many ions are emitted through a specific area about the thruster.
4. Peak ion current ($I_{i_{pk}}$), the maximum ion current of the plasma discharge.
5. Arc current length (t_p), the time duration of the plasma discharge.
6. Search coil voltage (V_{sc}), the induced voltage in the search coil produced by the magnetic flux. The magnetic field strength is measure using a search coil which provides a measure of the magnetic flux which the plasma plume and the emitted ions are subjected to.

7. Normalised ion-to-arc current ratio $(J_{pk})_{ion}$, the normalised ion-to-arc current ratio used in directly comparing the ion-to-arc currents for given configurations to obtain qualitative relationships.

When conducting the experiment, three different cathode materials were tested; Cu, Fe and Al (Refer to Section 5.3 for cathode material selection). For each material, a range of magnetic field strengths between 0 - 250 mT were applied to the vacuum arc to investigate the VAT performance over a range of magnetic field strengths. The ICDD was measured at angles between $\pm 90^{\circ}$ about the emission center of the VAT plasma plume. This was done to evaluate the ICDD at various angles to evaluate the influence of pulsed magnetic fields on the ion distribution within the plasma.

4.4 Uncertainty Analysis

The propagation of error is the influence on a results due to the uncertainty of any data used in determining the result. Propagation of uncertainties from both processed results and measured results were dealt with by using the following propagation of error equation,

$$\delta D = \sqrt{\left(\frac{\partial D}{\partial X_1}\right)^2 \delta X_1^2 + \left(\frac{\partial D}{\partial X_2}\right)^2 \delta X_2^2 + \dots} \tag{4.1}$$

where D is a function of variables X_1, X_2, and ∂D , ∂X_1 , ∂X_2 are the associated uncertainties. This was done for all error propagation unless otherwise specified.

4.5 Data Filtering & Analysis

The signals were captured by a Pico Technology Picoscope 5443D MSO with a 125MS/s sampling rate at 16-bit resolution which produced 625,000 data points per channel. All signals were captured for each VAT pulse which was triggered by the inductor pulse. An example of this is shown in Figure 4.1.

Due to the noisy nature of the vacuum arc, Gaussian filtering methods were used to ensure accurate measurements of the arc current, ion current and magnetic field induced voltages. To account for the stochastic nature of vacuum arc response and ion production, $\sim$150 samples were captured for each test, unless otherwise stated.

The stochastic nature of vacuum arc thrusters (VATs) refers to the random and unpredictable behavior of certain aspects of their operation. This randomness can be attributed to

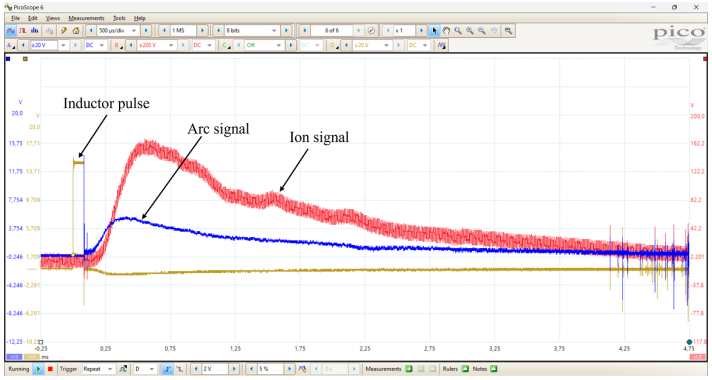

Figure 4.1: Pico Technology Picoscope 5443D MSO data capture for all experimental tests conducted. Scope shows the signals for arc current, ion current and inductor pulse which is used to trigger the automatic saving of the data.

various factors, such as the formation and movement of cathode spots, plasma generation, and the interaction between the plasma and the magnetic field (Cui, Liu and Gao 2019).

Moreover, the interaction between the plasma and the magnetic field in magnetically enhanced vacuum arc thrusters (MEVATs) can also exhibit stochastic behavior. The magnetic field can influence the arc discharge channel shape and the structure of cathode attachment, affecting the arc burning voltage and the average current passed by the cathode spot This interaction can result in fluctuations in the thruster performance and efficiency (Cui, Liu and Gao 2019)

Due to the stochastic nature of the vacuum arc discharge, a Gaussian-weighted moving average was applied, this method was beneficial for a few reasons:

1. **Smoothing out noise and fluctuations:** Gaussian-weighted moving averages are commonly used in signal processing to smooth out noise and fluctuations in data, making it easier to identify trends and patterns (Cui, Liu and Gao 2019).

2. **Applicability in various applications:** Gaussian-weighted moving averages have been used in different fields, including vacuum arc thruster experiments. For example, the micro-Cathode Arc Thruster (μCAT) has been developed for small spacecraft applications, and its performance has been characterized using this method (Dennison et al. 2018).

3. **Improved accuracy:** Using a Gaussian-weighted moving average can help improve the accuracy of the analysis by averaging out multiple readings. This can be particularly useful when dealing with complex plasma dynamics and various instability phenomena in vacuum arc discharges (Yang et al. 2021)

Additionally, misfired discharges had to be filtered out to ensure that these data were excluded from the analysis of each test. The following outlines the data filtering process implemented during the data processing stage:

1. A Gaussian-weighted moving average was applied over a specified sliding window. This was done to account for noisy signal responses.
2. The next filter applied was the exclusion of any misfired pulses. This was done by accepting any VAT discharge which generated an arc discharge with a maximum arc current higher than 50 A.
3. A final Gaussian-weighted moving average was applied to the ion current, arc current and search coil voltages to further smooth noisy data and filter out electromagnetic interference (EMI) noise produced at the start and end of each VAT pulse.

An example of the fully filtered data against the raw data can be seen in Figure 4.2.

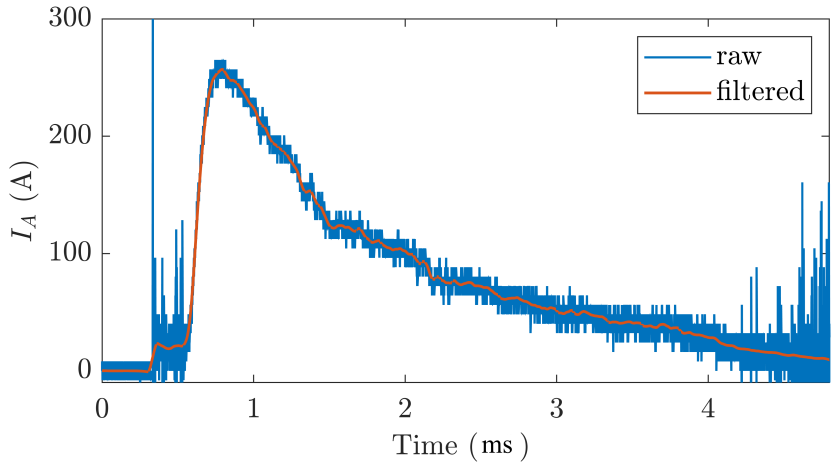

Figure 4.2: Gaussian-weighted moving average smoothing for arc current and raw collected data of arc current.

Once all the raw data had been processed, the ICDD distributions for each configuration was determined through a curve fitter. The best surface fit used the theoretical ion density distribution equations as shown in Equation 3.7, 3.8 and 3.9. These were implemented in MATLAB to obtain various curve properties such as R-squared, SSE (Sum of Squared Estimate of Error) and fit factors. The ion-to-arc current ratios were captured for each configuration and averaged into a single representative mean value (with 95% confidence boundaries) for each configuration at each angle.

Chapter 5 Thruster Design

The thruster design is generally heavily dependent on the space and weight restrictions place on current CubeSats. However, for the purpose of this study, the weight and size of the VAT was not restricted to satellite integration and the focus was placed on the behavior of the plasma and not the design of the thruster itself. The operation and performance of the VAT plasma is reliant on various physical aspects of the VAT design. The main aim of the VAT design process was to implement a prototype which is simple, especially with regards to manufacturing and assembly to minimise cost and risk of error during testing. It was decided that a modular design would be the best approach to testing various materials.

5.1 Geometry Design

VAT designs have generally implemented a coaxial thruster geometry. This design was used as there is a greater degree of symmetry along the centreline of the thruster. This symmetry is desirable in carrying out research with regards to the plasma plume and the ion distribution during firings as the angular error is greatly reduced. It was decided that the cathode would be placed within the insulator as this would focus the production of plasma nearer to the centreline of the thruster, reducing error in ICDD measurements. The simple geometry of the cathode rod makes it easy to manufacture and replace once the cathodic material has been eroded significantly. To keep the cathode face coplanar to the anode face, the cathode was designed to be screwed into the thruster allowing for the cathode to be fed out manually after significant erosion of the cathode material. An important consideration made during the design process was the location of the magnetic coil. Due to the non-uniform magnetic field along the center line of the coil outside its length, it is crucial to position the coil such that the entire plasma plume is encompassed within the magnetic field generated by the coil's length.

After performing a number of design iterations it was found that the ideal VAT design would have the following components size specifications:

1. The diameter of the cathode rods were 6 mm with a length of 46 mm.
2. The inner diameter of the insulator was 6 mm with an outer diameter of 10 mm and a length of 38 mm. The insulator was alumina ceramic. Alumina ceramic has become the standard insulator material choice in vacuum arc applications given its exceptional thermal and electrical properties. The insulator face was set between 0-0.5 mm below the anode to ensure adequate contact between the electrodes.
3. The inner diameter of the anode was 10 mm with a length of 10 mm. The outer diameter was chosen to be a particular design point due to the addition of a magnetic coil.
4. The thruster housing was made of ultra-high molecular weight polyethylene (UHMWPE), which was readily available, and is easily machined. The housing provided high electrical insulation between the anode and cathode as well as low outgassing effects.
5. All VAT components were manufactured with a tolerance of ± 0.01 mm.

With the above constraints in considerations, two designs were investigated within the initial testing of the VAT:

Concept one:

The first concept that was investigated was a coaxial thruster with a recessed edge on the anode. The recessed edge was implemented to allow a smaller magnetic coil to be placed around the anode. The smaller anode would increase the magnetic field for a magnetic coil with the same number of loops.

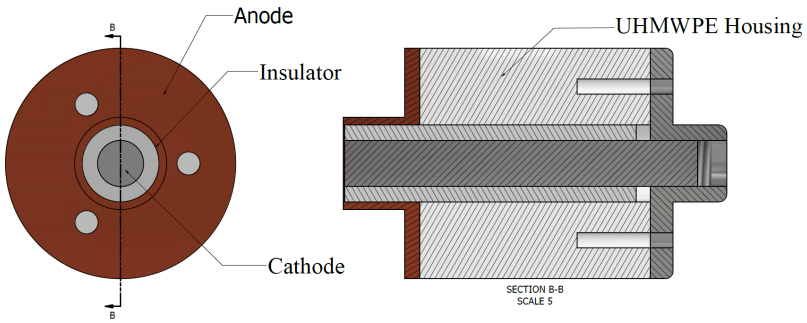

Figure 5.1: VAT concept one design with coaxial design and recessed anode edge to allow for smaller magnetic coil attachment.

When attempting to achieve the desired arc currents, it was observed that anode and cathode components were subjected to extensive Joule heating. Joule heating is the process in

which a current carrying material produces heat due to internal resistance. This occurrence was due to lack of heat dissipation in the metals. In a vacuum, the lack of atmosphere prevents cooling through convection, which in turn results in thermal transfer through conduction. The recessing of the anode edge reduces the volume of the anode, resulting in an increase in volumetric heat capacity. This results in the components being subjected to higher thermal loads. The VAT components conduct thermal energy to the contacting components. The thermal conduction resulting in excessive heating and causing the UHMPE housing and the anode itself to warp.

Concept two:

The second concept was very similar to that of the first, however did not have a recessed edge. The removal of the recessed edge resulted in far less thermal heating of the VAT components as the anode had a larger mass in which to dissipate its own thermal energy.

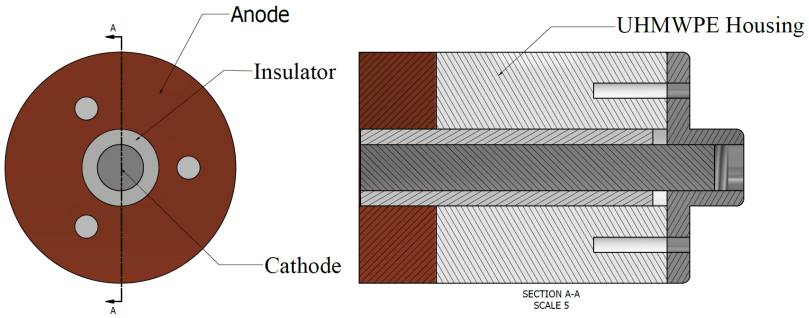

Figure 5.2: VAT concept two design with unrecessed anode edge to allow increase mechanical strength and increase thermal conduction properties.

However, the increase in size of the anode resulted in the unavoidable increase in size of the magnetic coil design, shown in Section 5.5. It was decided that the arc current and preservation of the VAT was of greater importance to the study than the magnetic field strength.

5.2 Anode Material Selection

One significant advantage of VATs is the fact that nearly any conductive metal can be used as fuel. Typically, metals such as Al, Fe, Cu, and W are used given that they are not considerably effected by expected mechanical loads, out-gassing and Joule heating. A range of materials were considered for the anode of the VAT.

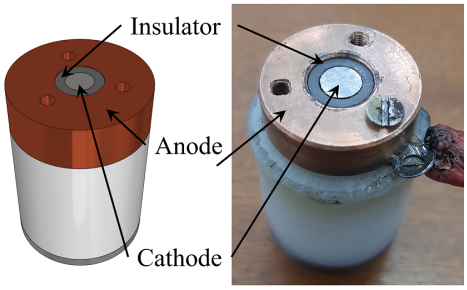

Figure 5.3: selected VAT coaxial design with inner cathode rod, ceramic alumina insulator and outer anode. UHMWPE housing with anode attached to positive terminal of PPU circuit.

Table 5.1: denisty $\rho\,(\mathrm{g/cm^3})$, electric conductivity $\sigma(\mathrm{MS/m})$, melting point $T_m\,(^\circ\mathrm{C})$, thermal conductivity $\lambda_T(\ \mathrm{W/(m\cdot K)})$ for potential anode selection for VAT design (White 2018).

Material	Type	$\rho\,(\mathrm{g/cm^3})$	$\sigma(\mathrm{MS/m})$	$T_m\,(^\circ\mathrm{C})$	$\lambda_T(\ \mathrm{W/(m\cdot K)})$
Ag	Metal	9.320	61.35	961.78	429
Cu	Metal	8.02	58.0	1084.62	401
Al	Metal	2.38	36.59	660.32	243
Fe	Metal	6.98	10.02	1538	80.2

Table 5.1 shows the typical electrical and mechanical properties of possible electrode selection. During the operation of the VAT, the anode is subjected to considerable Joule heating which is dissipated to the alumina insulator and the VAT housing. Excessive heating of the anode could potentially damage the insulator and VAT housing. In this case, the best material for the anode would be Fe given it's low thermal conductivity. However, Fe's electric conductivity is considerable lower than Cu which is disadvantageous in vacuum arc discharges. Ag is seen to have a better electrical conductivity than Cu, however is more expensive and is not readily available for machining. It was decided to use Cu as the anode given the good electrical conductivity and moderate thermal conductivity properties.

5.3 Cathode Material Selection

The selection of cathode material was based on testing materials with a wide range of mechanical and thermal properties.

Table 5.2: Ion Mass M_i (AMU), Erosion Rate E_r $(\mu g/C)$, Arc discharge voltage V_{arc} (V) and Ion velocity v_i(m/s) for potential cathode selection for VAT design (Polk et al. 2008).

Element	M_i(AMU)	$E_r(\mu g/C)$	V_{arc}(V)	v_i(m/s)
Al	26.9	28	23.6	15400
Ti	47.9	30	21.3	16700
Cu	63.55	35	23.4	12800
Fe	55.85	48	22.7	11800
W	183.85	55	31.9	14300

The decision was made to test Cu, Al, and Fe as baseline cathode materials due to their diverse thermophysical and vacuum arc properties, as well as the availability of predicted VAT performance metrics (Polk et al. 2008). Furthermore, these materials were readily accessible within the university, allowing for prompt machining if necessary.

5.4 Thrust Correction Factor

The thrust produced by the VAT can be evaluated by determining the ratio of axial momentum flux through the anode exit plane to the total momentum flux in that plasma plume. This can be done by using a thrust correction factor C_T^p. The thrust factor considers the effect of the thruster geometry as well as the the plume divergence. This expression takes into account the interference of the anode walls and ejected ions from the cathode surface. The deposition of the ejected ions onto the anode inner walls result in the deposited ions having zero contribution to the overall thrust. Experimentation conducted by Polk et al. 2008, demonstrated that for a maximum thrust factor is achieved when the anode and cathode faces are coplanar, so the anode does not shadow the plasma flux.

Assuming a perfect distribution as shown in Figure B.2a, and assuming a coplanar VAT configuration, the thrust factor is $C_T^p = 0.67$, where $C_T^p = 1$ is perfect beam collimation and all ion momentum is directed along the center line of the thruster. The derivation for the ICDD thrust factor can be found in Appendix B. The thrust factor can thus be used to evaluate the thrust performance for a given ICDD.

Despite the anode and cathode being coplanar, the magnetic coil had to be taken into consideration as the coil is placed outside of the anode which causes an additional shadowing effect of the plasma plume. This is referred to as plasma shielding. This is investigated in Section 5.5.1.

5.5 Magnetic Coil Design

A number of consideration were made in the initial design process of the magnetic coil. The first consideration was the selected design of the VAT. As the VAT had a coaxial design, a multilayer solenoid was selected to ensure the most efficient and secure fitting of the magnetic coil around the anode. The initial design of the magnetic coil was based on a first estimation model, in order to reach achievable magnetic field strengths through the center of the coil. The calculation of the magnetic field $\vec{B}$ for a given coil radius r_c and length l_c was done through the use of the Biot Savart law:

$$d\vec{B} = \frac{\mu_0}{4\pi} \frac{Id\vec{l} \times \hat{r}}{r^2} \tag{5.1}$$

where $\mu_0 = 4\pi \cdot 10^{-7}$ N/A^2.

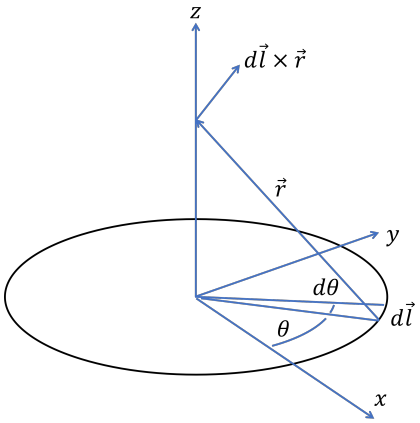

Figure 5.4: Magnetic field on axis of current carrying loop

This equation allows one to determine the magnitude and direction of magnetic fields for arbitrary current distributions such as rectangular or circular coils. The magnetic field due to the current carrying coil is found by integrating Equation 5.1 along the wire.

$$\vec{B} = \frac{\mu_0}{4\pi} \int_{\text{wire}} \frac{Id\vec{l} \times \hat{r}}{r^2} \tag{5.2}$$

This allowed for the determination of the magnetic field along the VAT center line. There were a few constraints that had to be considered in the initial design, these being:

1. The inner diameter had to be slightly larger than the outer diameter of the anode to ensure secure fitting. An inner coil diameter was 32 mm to allow for the coil holder.

2. The length had to be as small as possible to reduce the effects of plasma shielding. Plasma shielding is discussed in more detail in Section 5.5.1. A length of ∼18 mm was selected to avode coil slippage on the coil holder.

3. The radius of the copper wire used had to have an appropriate radius in order to account for resistance. It was decided to use an enameled Cu wire with a diameter of 0.5 mm.

4. The magnetic coil was attached through interference fitting, otherwise known as friction fitting or pressed fitting. This allowed for a simplified design. Slippage tests were conducted to ensure that the magnetic coil remained in place between consecutive tests.

It was found that through the adjustment of the input current, it was possible to determine the adequate magnetic field strengths required to conduct the experiment.

Figure 5.5a shows a coil with 100 loops generating a maximum magnetic field strength of 177 mT. This was achieved with a input current of 50 A.

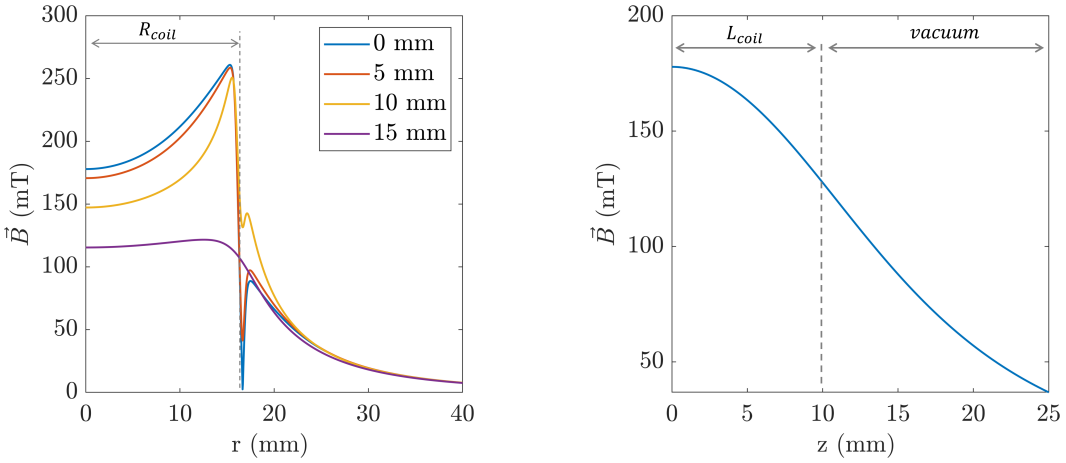

(a) **(b)**

Figure 5.5: Initial simulated magnetic field results for coil design (**a**) Radial magnetic field strength of coil with 100 loops and an inner radius of 16 mm and length of 18 mm. (**b**) Magnetic field strength along the center line of the thruster with the face of the cathode found at 0 mm.

The results above were obtained through a numerical finite element approach using MATLAB.

The constraints on the design of the coil had a significant influence on the current required to produce adequate magnetic field strengths. As the strength of the magnetic field is inversely proportional to the coil radius square, the large anode results in a large coil

current (greater than 50 A). A smaller anode was attempted, however due to the nature of heat dissipation within a vacuum chamber, the VAT was subjected to extensive heating and thus reducing the size of the anode was not acceptable.

It was decided that the ideal method of magnetic field generation would be through an capacitive discharge circuit in order to achieve high enough currents in the magnetic coil.

5.5.1 Plasma Shielding

The addition of a magnetic coil around the anode results in the deposition of ejected ions on the inner walls of the magnetic coil. Similar to that of the protruding anode, this causes a reduction in thrust due to momentum loss. Figure 5.7 shows the magnetic coil configuration for the VAT ICDD experiments.

Pietzka 2016 conducted an experiment of various plasma shielding angles of 45°, 62°, and 76° shields were tested. These angles were measured as shown in Figure 5.6. These tests demonstrated that a greater shielding angle leads to a narrowing of the ICDD of the VAT plasma. It was demonstrated that a shielding angle of 45° had the best results with minimal losses.

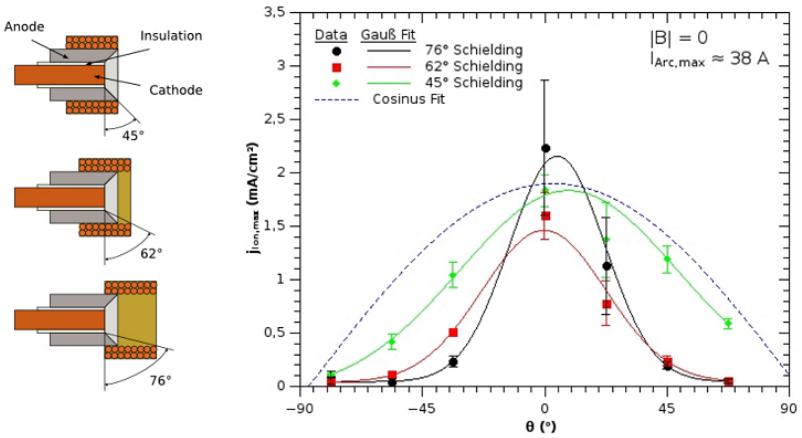

Figure 5.6: Peak ICDD for different coil configurations with various plasma shielding angles with $\vec{B} = 0$ mT and peak arc current $I_{A_{pk}=}$ 38 A. (Pietzka 2016)

The placement of the coil was based on two main reasons, the minimal thrust losses at a high angles, as well as the maximum magnetic flux which would be found at the center of the coil.

To account for the magnetic coil plasma shielding, an additional thrust correction factor due to the placement of the coil had to be included into the overall thrust factor. This was

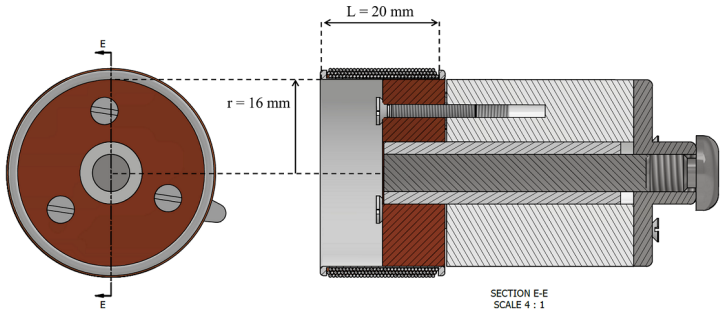

Figure 5.7: Thruster geometries of magnetic coil positioning for a coil of 20 mm length and 32 mm diameter with $\sim$ 100 turns.

one of the main considerations made in the design of the VAT as well as the magnetic coil used in generating the magnetic fields. Figure 5.8 shows the geometries of the magnetic coil and VAT.

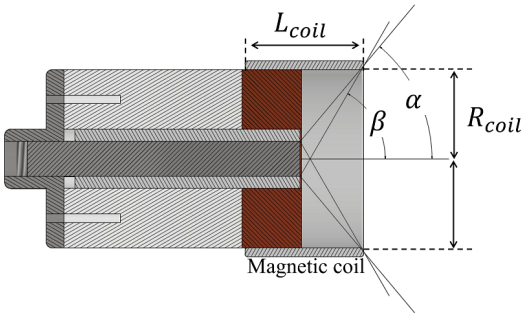

Figure 5.8: Thruster geometries of magnetic coil positioning demonstrating the plasma shielding angle. α and β represent the maximum and minimum sight angles for the variation in arc discharge along the surface of the cathode.

Based on the geometry of the thruster, the plamsa shielding thrust correction factor can be expressed as C_t^{coil}. Based on the variation in sight angle from one side of cathode surface to another, the mean sight angle was used. It was found that the maximum sight angle was $\beta = 60^\circ$ ($\pm 0.1^\circ$) and minimum sight angle was $\alpha = 50^\circ (\pm 0.1^\circ)$. The thrust correction factor for the coil was thus determined by the following expression:

$$C_t^{coil} = \frac{\int_0^{(\alpha+\beta)/2} \cos\alpha d\alpha}{\int_0^{\pi/2} \cos\alpha d\alpha} = 0.82(\pm 0.018) \tag{5.3}$$

thus resulting in a final thrust factor of:

$$C_T = C_T^p \cdot C_t^{coil} \tag{5.4}$$

This final thrust factor can thus be used in evaluating all ICDD for any given angle of plasma shielding that may be caused by the magnetic coil. This coil thrust correction

was applied to all thrust factor calculations conducted on the VAT with the magnetic coil attachment.

It must ne noted that the thrust correction for plasma shielding does not take into account the collimation of ions within the plasma plume. A significant collimation of ions would result in less momentum loss due to plasma shielding and thus an increase in thrust. This is an possible area of further study in obtaining more accurate estimates of thrust correction.

This correction could prove to be a useful correction for future work in predicting the effects of ion collimation and plasma shielding for magnetically enhanced VATs.

Chapter 6 Experimental Apparatus & Setup

All research and experimentation took place at the Wits Space Propulsion Laboratory within the School of Physics at the University of the Witwatersrand. The majority of the required instrumentation could already be found within the Wits Propulsion Lab, such as the stainless steel vacuum chamber, a number of power supplies, and function generators, however some equipment was provided by the School of Mechanical, Industrial and Aeronautical Engineering. In addition, the School of Physics carried out a portion the manufacturing of the mechanical components and diagnostic tools used within the experiments.

6.1 Vacuum Chamber and High-Pressure Pump System

All tests were performed within the stainless steel vacuum chamber. The vacuum chamber shown in Figure 6.1, had multiple feed ports along the circumference of the base which could be easily replaced with a variety of attachments. The vacuum chamber had a hemispherical lid supported by a mechanical hoist in order for the lid to easily and safely be removed and manipulated for access. Various feed ports were used throughout the testing process, mainly a viewing port, VACOM multi-pin, and high-voltage leads, and a pressure gauge. The pressure readings were taking by a low-vacuum Edwards PK-10 Pirani gauge and a high-vacuum Leybold-Haraeus PM41 Penning Gauge.

The pump system for the vacuum chamber consisted of a water-cooled oil diffusion pump (Leybold-Heraeus), and a roughing pump (Alcatel 2012A). Tests were performed at around 10^{-6} Torr.

It was desirable to have as few components within the vacuum chamber as possible to reduce the presence of outgassing. Outgassing is typically most relevant within vacuum applications, this refers to the release of gas trapped within certain materials. Moisture, sealants, lubricants, and adhesives are the most common sources, but even metals and glasses can release gases from cracks or impurities. The gas released from these materials

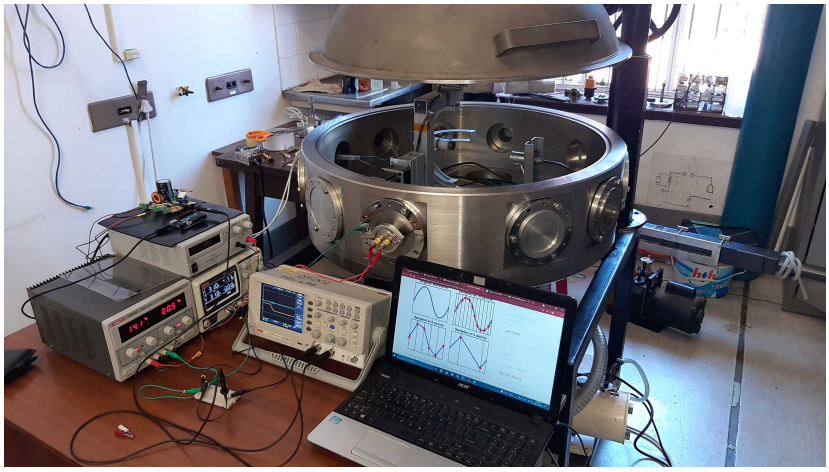

Figure 6.1: Stainless steel vacuum chamber used for VAT testing with automated real-time data collection.

lowers the vacuum quality by increasing the pressure. The gas released from the materials can also be reabsorbed onto other surfaces, creating deposits and contaminating the chamber (Chiggiato 2017). Outgassing can be avoided by selecting specific materials which are to be placed within the vacuum chamber and by minimising the material that is present within the vacuum chamber.

6.2 Pulsed Power Circuit

The Pulsed Power circuit design was based on the energy stored circuit designed by (Lun 2015), however when designing a VAT, it is important to understand how the various components affect the overall arc discharge of the VAT. In this study, the main focus was to create a reliable circuit that was capable of creating high density vacuum arc discharges with long discharge periods.

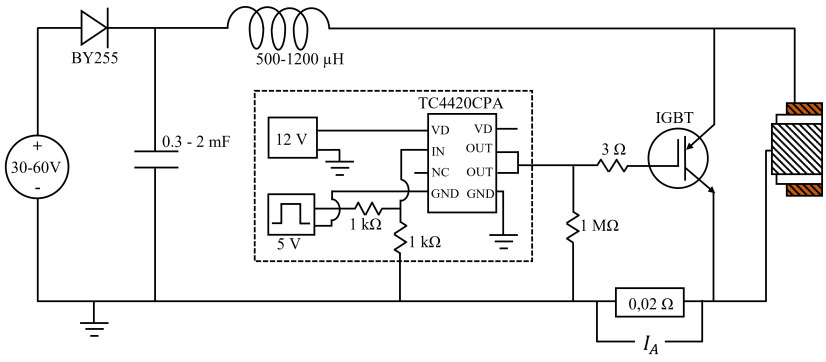

Figure 6.2: VAT PPU circuit diagram with power supply, capacitor, inductor, IGBT, pulse generator and VAT.

The PPU relies on three significant stages in generating the vacuum arc discharges.

Stage 1:

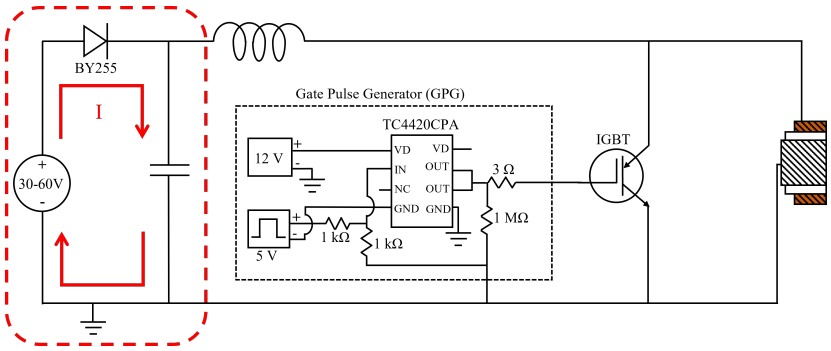

In the first stage, the pulse generator outputs a DC square wave of amplitude 2.5V with variable pulse length and frequency to the gate driver. The gate driver accepts a low-power input from the Arduino (microcontroller) and produces a high-current drive input for the IGBT. Initially the voltage supplied to the gate driver is at 0V, ensuring that the IGBT is open. As the IGBT and the VAT is open, the power supply only charges the capacitor.

Stage 2:

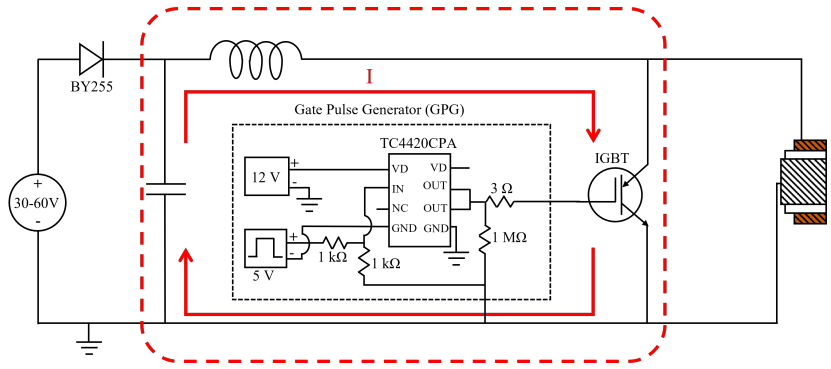

When the gate driver is supplied with a 2.5V pulse, the gate driver then supplies the IGBT with 12-14V, ensuring that the IGBT is in conduction mode. The current from the power supply and the capacitor is released through the inductor and the IGBT.

Stage 3:

In the third stage, the gate driver is again set to 0V, which opens the IGBT and allows for the capacitor to begin recharging. Simultaneously, the inductor attempts to counter the current transformation and generates a high voltage spike to maintain the initial current.

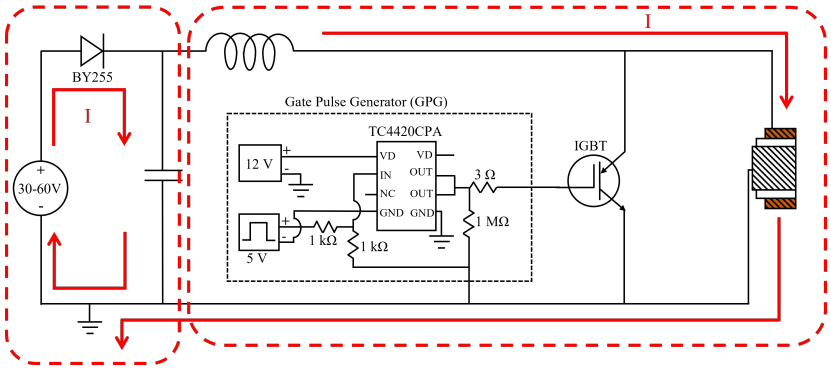

This voltage peak is applied across the anode and cathode of the VAT which causes an ignition across the graphite layer on the insulator thereby releasing the energy within the inductor causing an arc discharge to be triggered.

The operation of the entire circuit is dependent on the parameters of the pulse length, frequency as well as the capacitance and inductance of the components used within the circuit. A variety of circuit parameters were tested, such as the capacitance, inductance and supply voltage. It was found that a more capacitive circuit produced greater reliability in triggering and thus it was decided that the inductance would be approximately 500 μH. When testing the capacitance, it was found that the the greater the capacitance the greater the arc discharge length and arc current. However, in order to generate a stable and reliable arc thruster it was decided to have a capacitance of 2000 μF. A capacitance higher than 2000 μF created much longer arc pulses and resulted in both the anode and cathode heating to a point at which the ultra-high-molecular-weight polyethylene (UHWMPE) housing would melt and warp due to Joule heating.

6.2.1 Inductor Selection

When designing the PPU circuit, it was important to understand how the various components affect the overall performance of the thruster. The design process included testing various inductors and comparing these inductors with specific performance metrics. The main performance metrics which were taken into account were the arc current and the arc voltage.

It was decided that an inductor of 500μH would be implemented in the PPU circuit. This choice was made as it results in a higher arc current, and thus in a more reliable arc ignition due to the higher arc voltage.

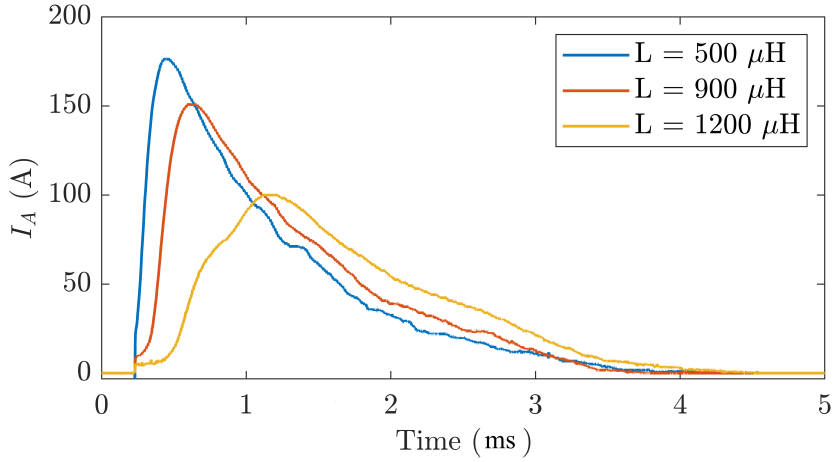

Figure 6.3: Arc Current for various inductors (500 μH, 900 μH, 1200 μH) with a supply voltage of 60 V. In these tests an Fe cathode was used with a 300 μF capacitor.

6.2.2 Capacitor Selection

The selection of the capacitor was similar to that of the inductor. A capacitor of 2000 μF was chosen for the PPU circuit as this capacitance results in a higher arc current. Having a higher arc current results in a greater production of ions within the plasma and thus a higher thrust production (Anders and Yushkov 2002).

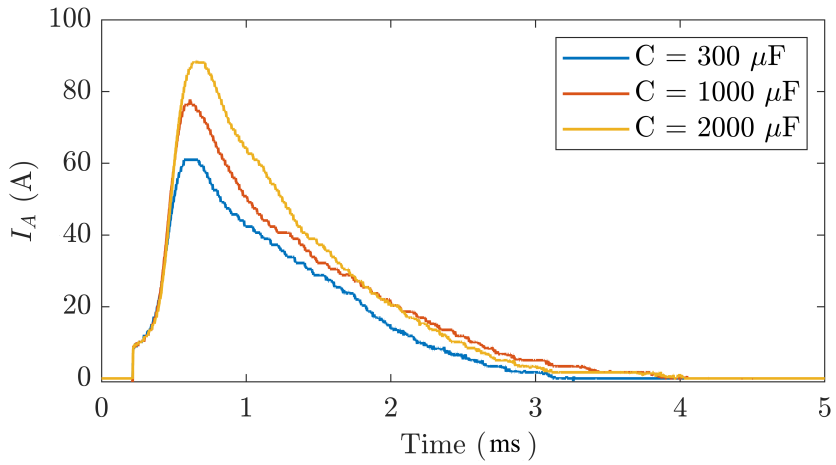

Figure 6.4: Arc Current for various capacitors (300 μH, 1000 μF, 2000 μF) with a supply voltage of 50 V. In these tests an Fe cathode was used with a 1200 μH inductor.

The main purpose of this study was to determine the influence of externally-applied magnetic fields to the ion density distribution within a vacuum arc discharge plasma, and thus a higher arc discharge which resulted in greater ion emission is desirable as a greater ion density increased the accuracy and resolution of the ion distribution readings.

6.2.3 Supply Voltage Selection

The choice of supply voltage was heavily dependent on the geometry of the thruster, as well as the inductance and capacitance of the PPU circuit. Various supply voltages were tested, and it was found that for the inductance of $I = 500\mu$H and a capacitance of $C = 1000\mu$F, as well as the geometry, ignition was only possible for voltages greater than 45 V.

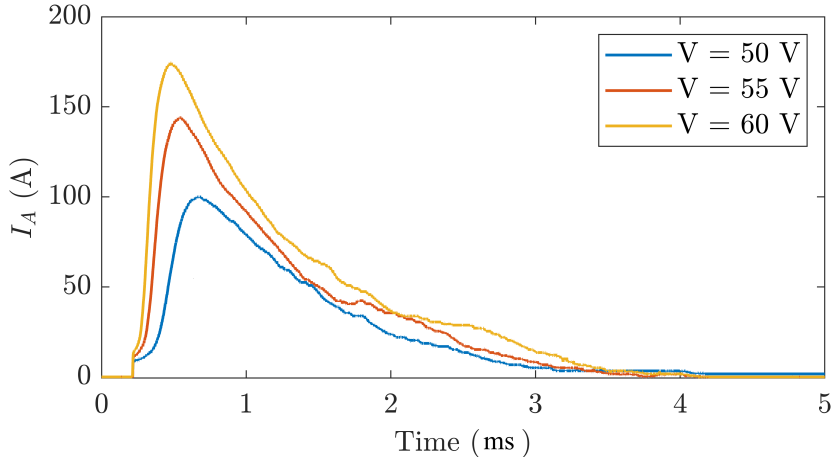

Figure 6.5: Arc Current Measurements for various supply voltages (50 V, 55 V, 60 V). These tests used an Fe cathode with a 500 μH inductor and and a 1000 μF capacitor.

Figures 6.5 shows that the supply voltage had a significant effect on the overall arc current. Supply voltages between 50-60 V were selected as these voltages had reliable ignition characteristics. Voltages greater than 60 V resulted in higher arc current which results in excessive heating of the thruster.

6.2.4 Pulse Length Study

An important aspect of VAT performance is the pulse length of the vacuum arc discharge. The pulse length has a direct influence on the cathode erosion, ion production and overall cathode life-cycle. During experimentation, it was desirable to produce a consistent arc current across all tests in order to allow for direct comparison between different materials and magnetic fields strengths. The arc current was controlled by varying the charging duration of the VAT PPU circuit, and thus by doing so it was possible directly compare the pulse length of each test. The aim of the initial testing was to produce a pulse range between 3-5 ms for each material consistently.

A peak arc current range of 250-300 A was selected in order to produce clear ion current measurements for later evaluation for the application of pulsed magnetic fields. The VAT was fired at a frequency range between 0.2 - 0.3 Hz in order to allow for continuous testing

and for each pulse length to be saved via the digital oscilloscope through an automated trigger save. Figure 6.6 shows an example of the results from the pulse length study which has been filtered to determine the average pulse duration for each material.

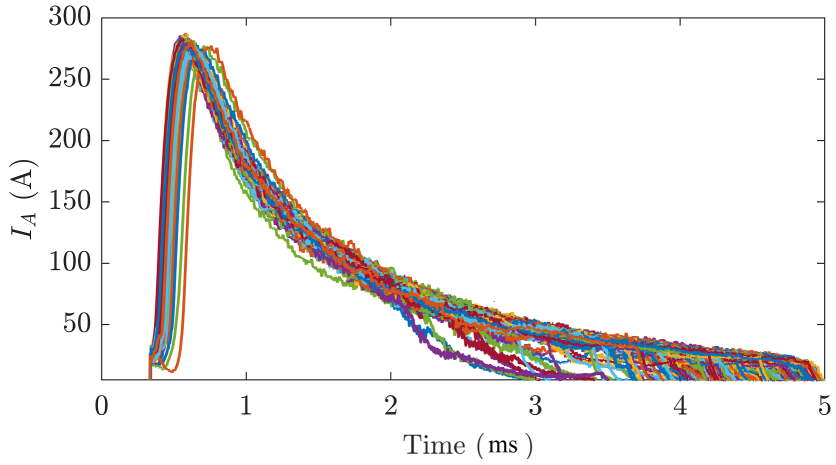

Figure 6.6: Sample pulse length study for Al cathode VAT with an average pulse length of t_p = 4.59 $\pm$ 1$\times 10^{-7}$ ms. These tests used a 2000 μF capacitor, 500 μH inductor with a supply voltage of 55 V.

These waveforms were averaged over 1000 pulses for each material in order to determine any significant pulse characteristics presented by each material.

Table 6.1: VAT pulse characteristics for various cathode materials

Material	Max I_A (A)	t_p (ms)
Fe	269 $\pm$ 0.0095	3.44 $\pm$ 9$\times 10^{-7}$
Al	277 $\pm$ 0.0032	4.59 $\pm$ 1$\times 10^{-7}$
Cu	274 $\pm$ 0.0042	3.66 $\pm$ 3$\times 10^{-7}$

The pulse length of the Al VAT was found to be $\approx$ 29.3% ($\approx$1.04 ms) longer than those of the Cu and Fe VATs. The circuit tuning successfully resulted in a consistent maximum arc current range between 260-280 A with the Fe cathode having a slightly lower arc current. This difference was dealt with by later evaluating all ICDDs as a fraction of the maximum ion-to-arc currents produced for each test.

As a result of the experiment's design, the fluctuation in pulse length did not play a significant role in assessing the impact of magnetic field strengths on angular ion density distribution. The experiment was conducted to pinpoint the primary distribution of ions during magnetic field pulsing. By focusing on the peak ion distribution and applying the magnetic field throughout the entire arc, variations in pulse length were minimized. The timing of the distribution was deemed inconsequential compared to the distribution itself.

Table 6.2 shows the range of circuit parameters tested in the initial VAT circuit prototyping.

Table 6.2: Range of baseline VAT circuit parameters in initial performance testing for various circuit components

Parameter	min	max	error
Supply Voltage (V)	50	60	$\pm$ 0.05
Capacitance (μF)	300	2000	$\pm$ 10
Inductance (μH)	500	1200	$\pm$ 10
Peak Arc Current (A)	60	280	$\pm$ 0.5
Pulse Length (ms)	3	5	$\pm$ 0.005
Pulse Frequency (Hz)	0.2	0.3	$\pm$ 0.001
Average Arc Power (W)	15.3	28.5	$\pm$ 0.109

6.3 Pulsed Magnetic Field Circuit

The implementation of a pulsed magnetic field was done by designing a capacitive discharge circuit which was capable of generating high currents through a coil. The circuit was designed to be able to discharge the built up charge through the coil for a desired pulse length. An important aspect of the design was to be able to control the pulse length of the magnetic field to ensure that the plasma is subjected to a constant magnetic field during its discharge. Various magnetic field generator circuits were explored, however the capacitive discharge circuit was more reliable and repeatable throughout.

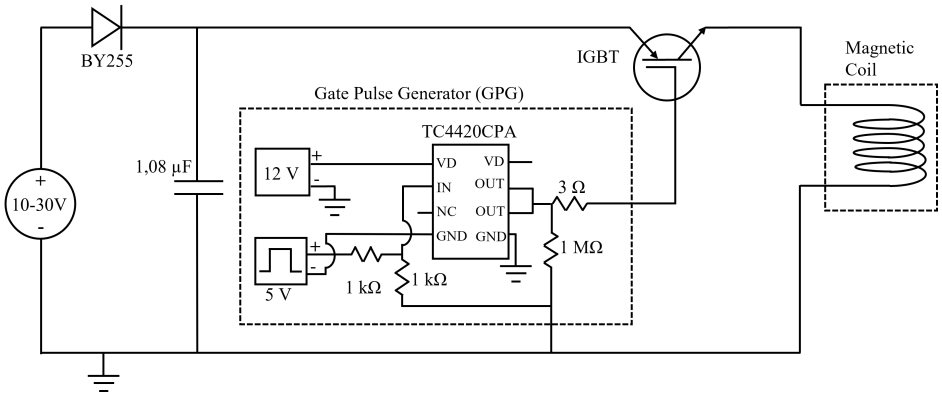

Figure 6.7: Magnetic field generator circuit with a 60 V power supply, high current IGBT and magnetic coil.

The generation of the magnetic field has two significant stages during operation.

Stage 1:

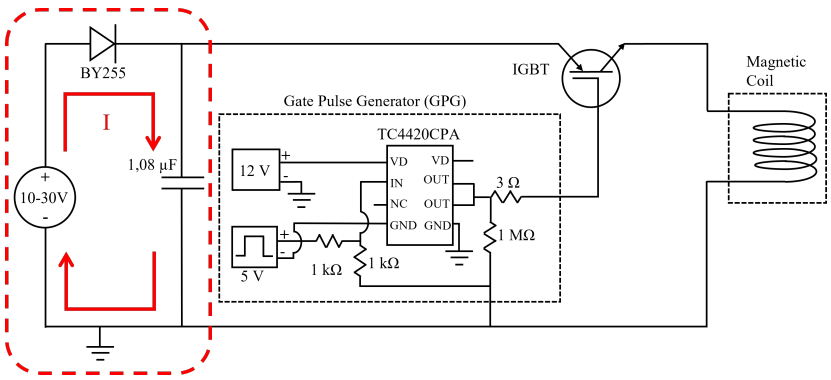

In the first stage, the pulse generator outputs a DC square wave of amplitude 2.5 V with variable pulse lengths and frequency to the gate driver. The gate driver accepts a low-power input from the pulse generator and produces a high-current drive input for the IGBT gate. Initially the voltage supplied to the gate driver is 0 V ensuring that the gate remains open,

and as the IGBT connection between the collector and emitter is open as well as the VAT, the power supply only charges the capacitor.

Stage 2:

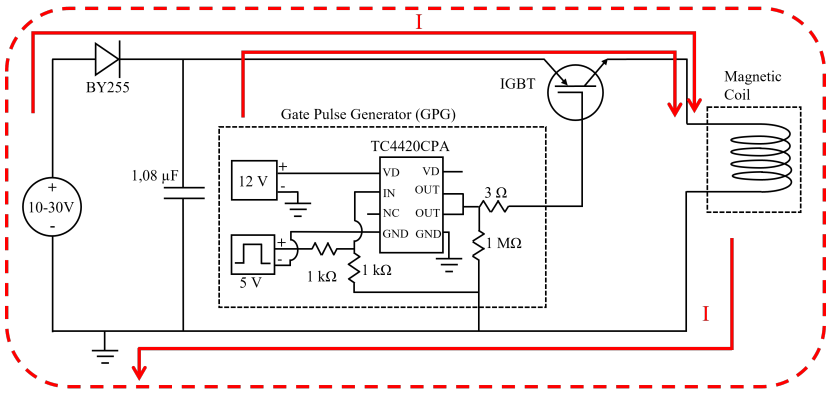

When the gate driver is supplied with a positive 2.5 V from the pulse generator, the gate driver supplied the IGBT gate with 12-13 V which swtiches the IGBT into conduction mode. This allows for the current in the capacitor and the power supply to be released through the magnetic coil which then creates a magnetic field proportional to the amount of current.

An important aspect of the magnetic field circuit design was to determine the magnetic field produced by the coil in real time. In order to do this a search coil magnetometer was used.

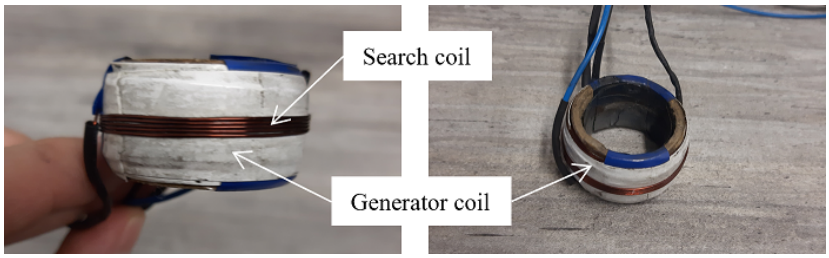

Figure 6.8: Search coil magnometer placed around the main magnetic coil with leads which could read the real-time induced voltage

A search coil magnetometer is used in numerous applications to measure magnetic field fluctuations. The search coil is a coil which is placed within a magnetic field, or in this case, around the main magnetic coil. The temporal variation in magnetic flux through N turns will induce a voltage in the search coil according to Lenz's Law:

$$V_{sc} = -N\frac{d\Phi}{dt} \tag{6.1}$$

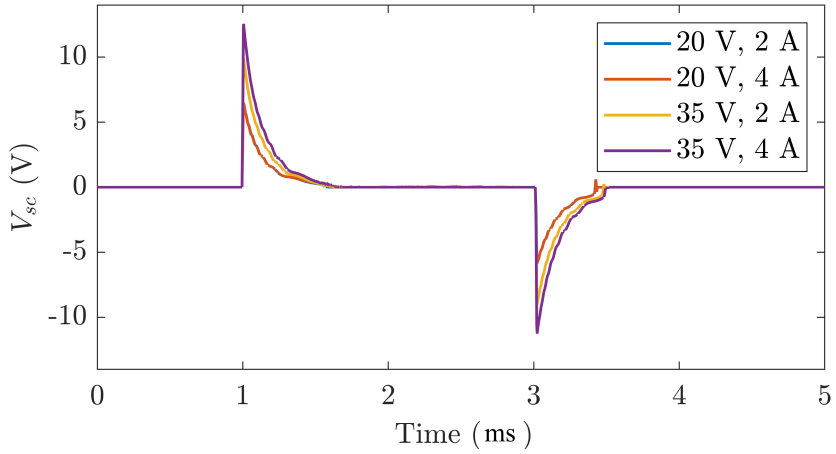

Figure 6.9: Induced voltage in search coil, for a pulse length of 3 ms and various power supply voltages and currents.

where V_c is the induced voltage in the search coil in Volts, N is the number of turns of the search coil, Φ is the magnetic flux in Weber, and t is time in seconds. This law was then used to calculate the the magnetic flux density through the integration,

$$B = \frac{1}{NA} \int V_{sc} \cdot dt \tag{6.2}$$

where B is the magnetic flux density in Tesla, and A is the area of the search coil in m^2. The induced voltage across the search coil was measured and then processed in order to determine the transient magnetic field strength experienced by the plasma within the magnetic field generator.

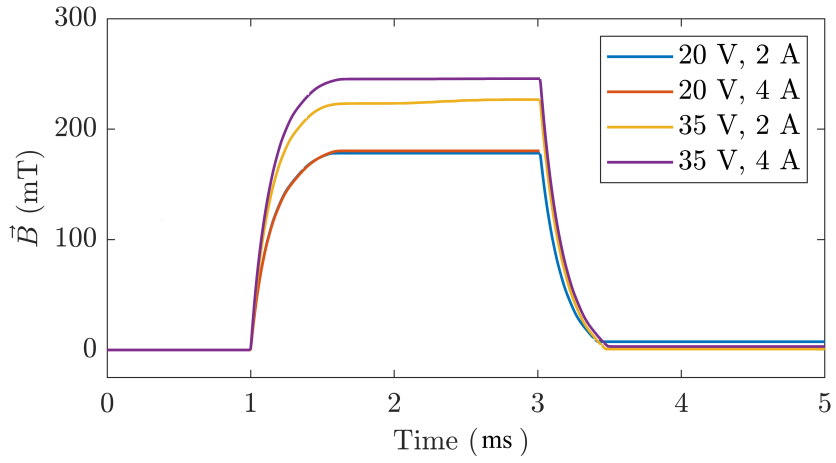

Figure 6.10: Magnetic field strengths ($\vec{B}$) of initial field generator design, with various input voltages and currents.

Figure 6.10 shows the magnetic field strength produced by the magnetic coil. The pulse lengths of the magnetic field generator were chosen to be ~2 ms long in order to ensure that the magnetic field was acting on the VAT discharge for the majority of it's arc discharge.

The magnetic fields were limited to greater pulsed periods based on the resolution of the digital oscilloscope as well as the power limitation of the fast acting switch used.

The fast acting nature of the arc discharge in comparison to the magnetic field generation required the initiation of these pulses to occur at different time intervals. Figure 6.11 shows the sequence in which the controlling IGBTs are switch on and off. This allowed for the magnetic field to be 95% fully generated at the time of the VAT arc ignition.

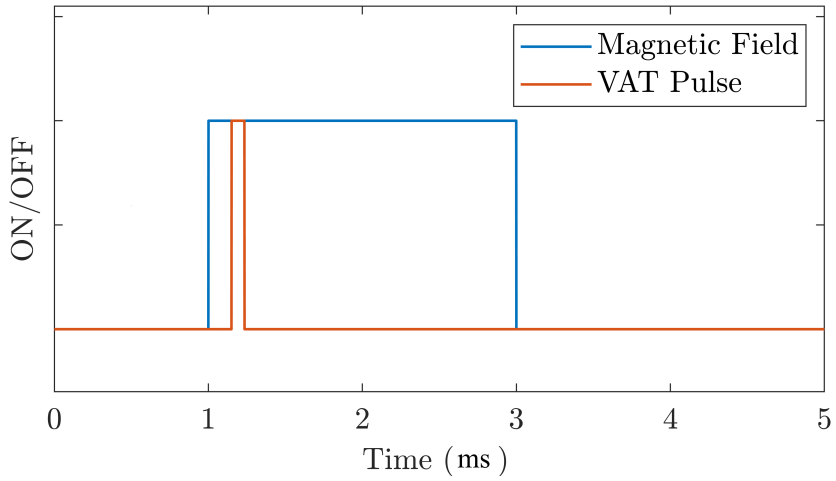

Figure 6.11: Timing sequence of vacuum arc thruster

Figure 6.12 shows an overlay of the magnetic field generation with a sample VAT arc discharge. The magnetic field is at full strength for the majority of the VAT arc discharge.

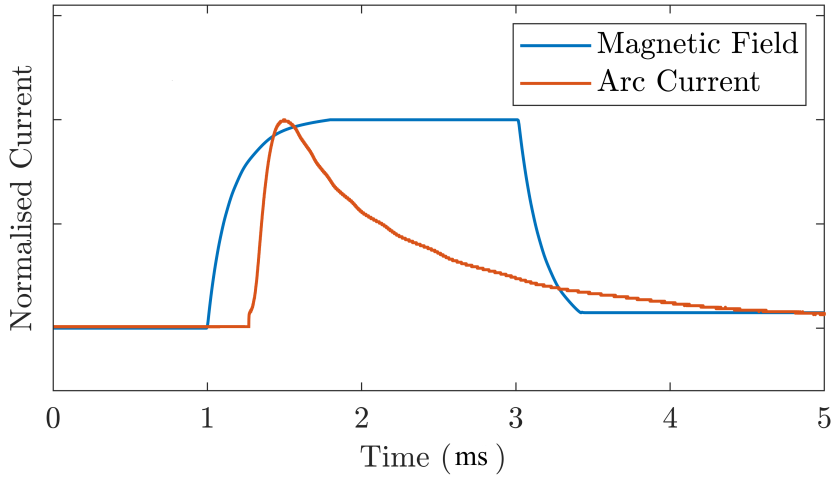

Figure 6.12: Timing sequence of vacuum arc thruster

The initial testing successfully produced magnetic field strength measurements between 150 - 250 mT through the use of the capacitive discharge current. It was decided that the magnetic field circuit would be completely separated from the VAT circuit as the added inductance of the magnetic coil would affect the operation of the VAT. The additional inductance of the magnetic coil would result in greater arc discharge lengths, as well as lower

arc current peaks due to the required power consumption. The variation in pulse length and arc current would result in difficulty in directly comparing the effects of different magnetic fields to VAT of different cathode materials.

After voltage and current adjustment, it was possible to generate desired magnetic fields which could be applied to the VAT consistently throughout the tests.

Table 6.3: Magnetic field generator parameter for various input voltages and currents for final selection and application to the magnetic vacuum arc thruster

Configuration	Voltage (V)	Current (A)	Magnetic Field Strength (mT)
$\vec{B_1}$	0	0	0
$\vec{B_2}$	17.0	4.0	150.0 ± 0.897
$\vec{B_3}$	36.0	4.0	250.0 ± 1.606

6.4 Two-Axis Rotation System

The Ion Current Density Distribution (ICDD) is an important measurement when dealing with plasma propulsion. The ICDD characterises the level of normal thrust produced by the plasma jet. As the ions are expanded into the surrounding space, a portion of the ions travel radially outwards away from the normal of the thruster and thus have significantly less contribution to the overall thrust production. Macroparticles are emitted generally at shallow angles to the normal of the cathode, and at low average velocities ($\sim$400m/s) (Daalder 1976). Thus, it can be assumed that the thrust produced can be accurately represented by the distribution of the ions within the plasma plume.

The VAT was mounted to a Two-Axis Rotation System, shown in Figure 6.13 which allowed for the VAT to be rotated about the cathode to different angles. The TARS used within this study was designed and made by (Lun 2015) which was based on the approach taken by (Sekerak 2005).

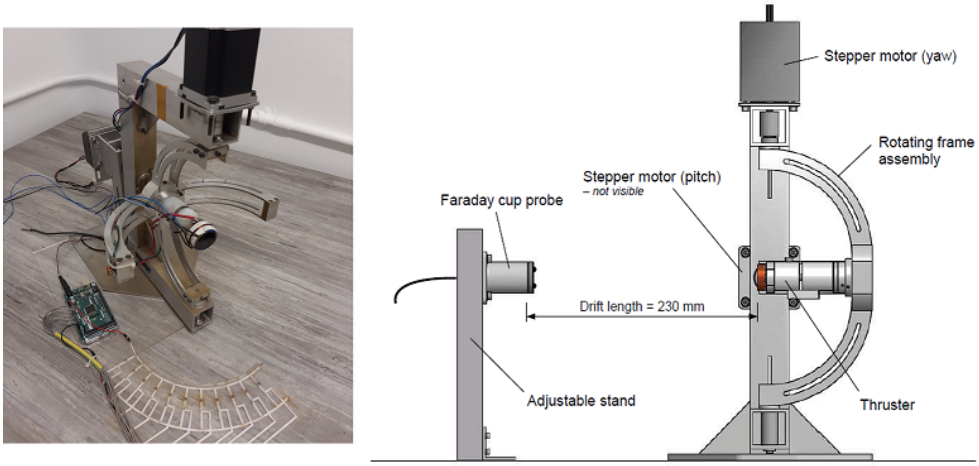

Figure 6.13: TARS with stepper motor for accurate angle variation. (left) TARS with laser optical alignment system used to ensure accurate angle positioning of VAT during testing. (Lun 2015)

The TARS provides a $\pm$ 90° pitch and yaw rotation in order to position the head of the thruster at a multitude of different angles. The rotation is about the thruster head ensuring the distance between the Faraday cup and the thruster remains constant throughout. The distance of the thruster from the Faraday cup is manually positioned for each test.

6.5 Thruster Positioning

The position of the thruster was controlled by an Optical-Alignment-System (OAS). The OAS used an attached laser emitter connected to the TARS which emitted a 650 nm wavelength beam onto the laser printed board with 11 light dependent resistors (LDR) which were spaced in increments of 9° $\pm 8.4 \times 10^{-4}$ ° from 0° to 90°.

This initial design only allowed for a 90° positioning range, however it was found that by rotating the OAS it was possible to increase the range to 180° about the thruster.

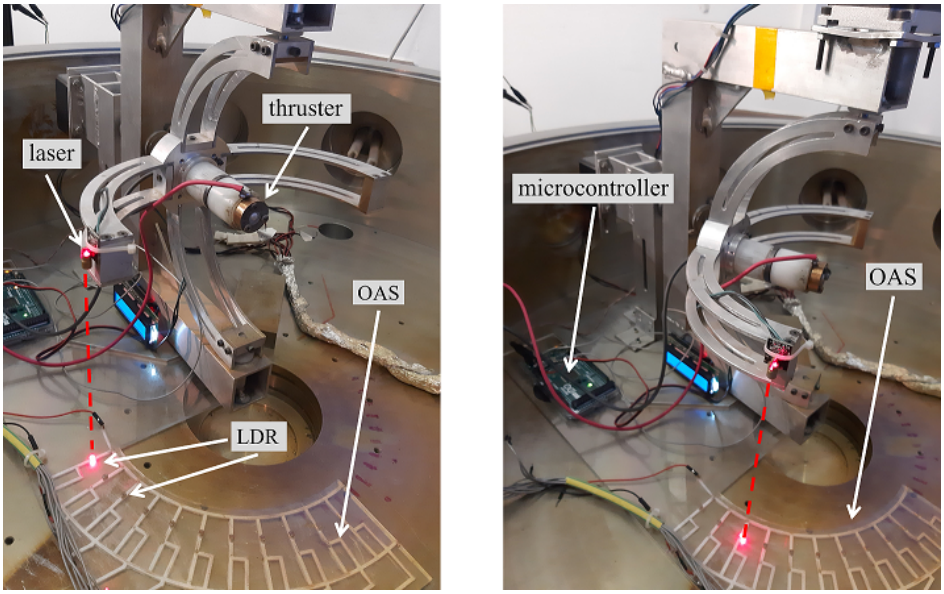

Figure 6.14: Optical Alignment System used during the experiment to vary the angle od the thrust for ICDD readings. Laser and microcontroller connected to 11 LDRs shown with LCD displaying the angle of the TARS.

The connected microcontroller was used use to process the analog readings on each LDR within the vacuum chamber. The LDR which exceeded a specific analog reading directly proportional to the light intensity was then displayed on the LCD screen in order to ensure that the angle could be read from outside of the vacuum chamber.

The LDRs were embedded into a laser cut perspex board which could be placed against the TARS with clips to ensure the perspex board did not move during the TARS rotation. Although the TARS was capable of two axis rotation, only the yaw rotation was used in this experiment due to the expected errors in pitch displacement with an applied load and the eccentricity of the TARS design.

6.6 Faraday Cup Probe

6.6.1 Background

One of the more important aspects of this research is the ICDD of the plasma created by the vacuum arc discharge. In order to obtain these ICDDs, a reliable method for measuring the number of ions about the vacuum arc discharge needs to be carried out. An ideal method of ion current measurement is through the use of a Faraday cup. The Faraday cup is shown in Figure 6.15.

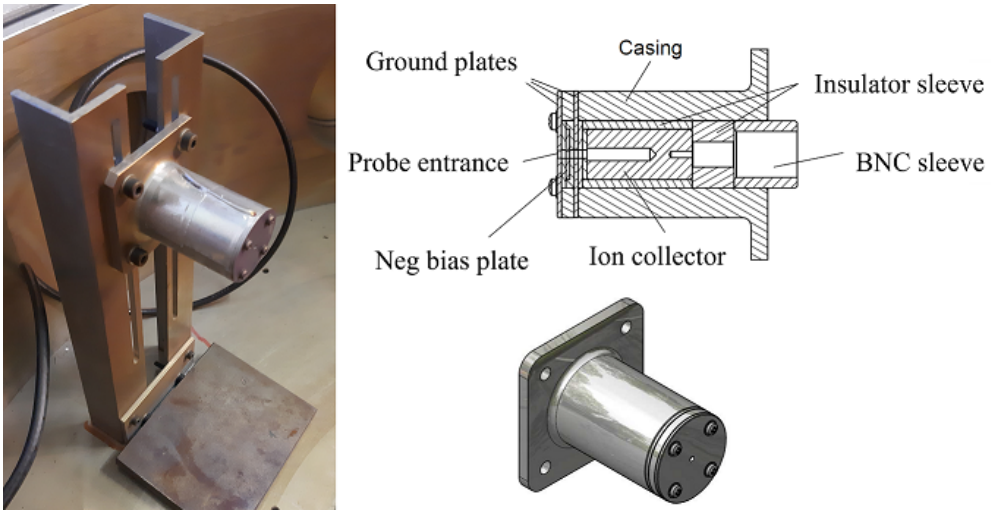

Figure 6.15: Faraday cup set up within the vacuum chamber and engineering drawing for the design.

Faraday cup probes are used to measure the ion charge flux at various points about the VAT plasma plume emission. The ion current is generally measured with a plate, cup or grid. A Faraday cup was used in this study as it allows for a greater accuracy and precision on a smaller scale due to the measurement of emitted ions through smaller areas. This approach does have several drawback which must be noted. The Faraday cup cannot distinguish between single and multiple ions in the ion current, and therefore a mass spectrometer to measure the ion charge-to-mass ratio would be required. Another important consideration to make is the electron emission from the plasma itself. As the plasma produced at the VAT is quasi-neutral, the charge of the ions and electrons cancel each other out. For this reason it is important to negatively bias the Faraday cup to repel the electrons.

The working principle of a Faraday cup probe is relatively simple, a negative potential is applied to the metal collector of the Faraday cup to attract and collect incoming positively charged ions and repel negatively-charged electrons. The moment the ions strike the collector of the Faraday cup, electrons flow from ground in order to neutralize the ions. The current flow from ground to the Faraday cup is measured by reading the voltage change

across a terminating (shunt) resistor in the probe circuit. It is possible to determine the number of electrons required to neutralize the positive ions and thus the number of ions entering the Faraday cup by measuring the voltage change across the terminating resistor.

The unique property of a Faraday cup is the due to the cylindrical shape of the collector surface. The implementation of a cylindrical Faraday cup provides many advantages to the overall accuracy. A Faraday cup with a depth 5 times greater than its diameter aids in preventing the escape of secondary electrons. Secondary electron emission occurs when the incoming ions have enough energy to release electrons from the surface. This would result in an inaccurate ion current measurement because a higher ion current would be measured than actually existed.

As a consequence of the limited surface and orifice area of the Faraday cup, only a fraction of the total ion current emitted by the thruster is measured. As a result the measurements should be presented as ion current densities (A/m^2) thus acknowledging and taking into account the finite area.

6.6.2 Faraday Cup Probe Setup

The main intention of the Faraday cup probe is to measure the ion current densities both at various angles about the plasma plume and at various distances from the plasma. Measuring the ion density distributions at various angles and distances from the thruster will provide insight into the thrust plume distribution, which will provide knowledge of the shape of the thrust-producing plasma jet and how this affects the performance of the thrust. An additional feature of this method of ion measurement is the ability to find the most likely ion velocity using the Time-of-Flight (TOF) method. The TOF method measures the time delay between the arc current peak and the Faraday cup ion peak to determine the time taken for the particle to travel from the thruster to the Faraday cup. This is advantageous as this provides characteristics on the ion velocities of various metal cathodes.

6.6.3 Faraday Cup Circuit Design

A schematic of the Faraday cup probe in Figure 6.16 included a DC to High Voltage DC Converter which converts an input voltage of 2 V to 200 V which is used to negatively bias the Faraday cup via a BNC cable.

A Digital DAQ measured the voltage drop across the terminating resistor to determine the ion current. However, the resistance of oscilloscope must be taken into consideration when

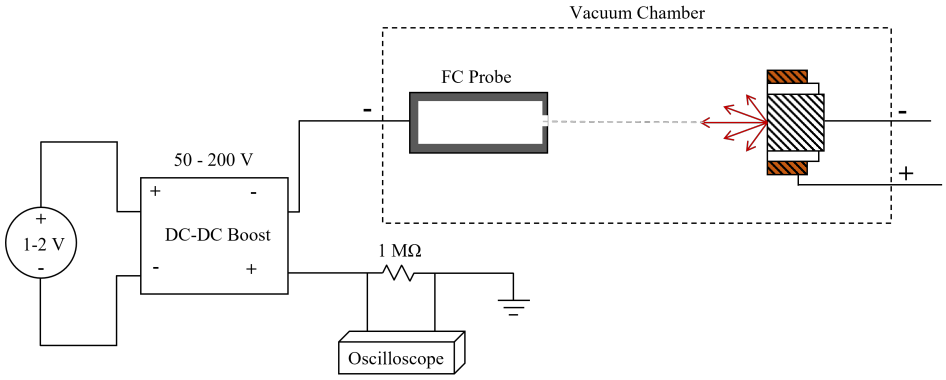

Figure 6.16: Faraday cup system set up with DC boost, Faraday cup, and shunt resistor to measure ion current for a given angle during testing.

using a large terminating (shunt) resistance. The true resistance of the terminating resistor is:

$$R_{true} = \frac{R_o R}{R_o + R} \tag{6.3}$$

where R_o is the resistance of the oscilloscope and R is the resistance of the terminating resistor. The terminating resistor value may range from kΩ to MΩ to ensure a good range of signal strengths. The ion current captured by the Faraday cup probe is

$$I_i = \frac{V_{CF}}{R_{true}} \tag{6.4}$$

where V_{CF} is the voltage drop measured across the terminating resistor.

The implementation of the Faraday cup requires a series of verification and validation checks in order to ensure that the Faraday cup was operating in the correct manner.

1. The probe ion current waveform was similar to that of the arc current measurement.
2. The probe received zero signal during testing when the aperture of the Faraday cup probe was blocked to all incoming ions.
3. The measurement of the ion current density decreased with increasing distance between the Faraday cup and the thruster.
4. A change in bias voltage changed the ion current signal. An increase in negative potential resulted in a higher ion collection due to the electrons being repelled.
5. A variation in Faraday cup angles results in a ion distribution that follows a Gaussian or Exponential distribution.

6.6.4 Faraday Cup Performance

Ion Density Distributions

The ICDD was measured over a range of ±90 ° in increments of 9° using a stepper motor. At each position, 150 signals for ion current and arc current were captured for processing. It was found that an increase sampling size affected the readings as their was a significant amount of cathode erosion which directly affected the performance of the thruster during the test. Initial tests were carried to determine the ICDD about the centreline of the VAT. Figure 6.17 shows the normalised ICDD for angles between 0-90° for initial validation. The data was normalised such that the distribution fit could be applied for all probe distances, cathode materials and arc currents.

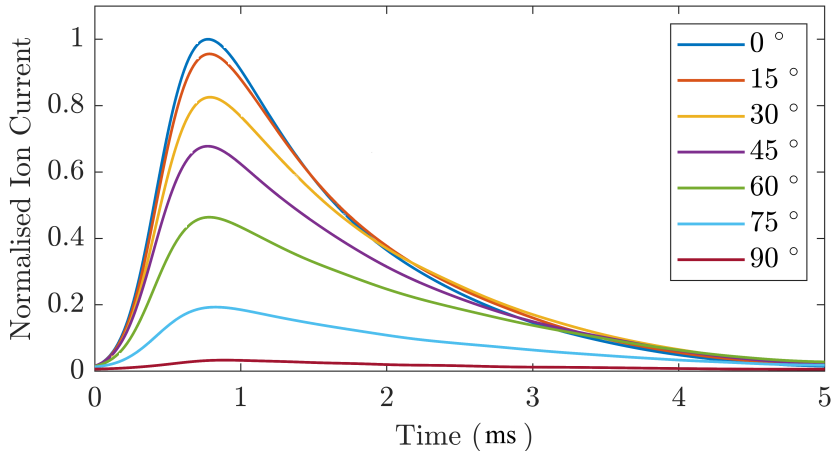

Figure 6.17: Ion Current measurements for various angles from the thruster normal (0°, 15°, 30°, 45°, 60°, 75°, 90°). These tests used an Fe cathode with the selected circuit parameters for the PPU. A 750 kΩ resistor was used with a Faraday cup voltage of -250 V.

Once all the data had been captured and processed, it was then possible to determine the max ion current for each angle, this could then be correlated to the max ion current at various angles about the centreline. A similar process was performed for various probe distances from the cathode. As stated before, the theoretical radial variation in max ion current is inversely proportional to the distance square, and thus by changing the distance of the angle and normalizing the max ion current, it was possible to determine the correlation to the experimental data with the stated theoretical angular distributions presented by Polk et al. 2008, and Lun 2015.

Measurements of the ion current signals at various probe positions (70 ±0.05, 160±0.05 and 300±0.05 mm) demonstrated that the max ion current correlates to the theoretical radial distribution ($1/z^2$) shown in Section 3.3. Angular measurements of the max ion current demonstrate that the angular distribution correlates closely with the suggest typical

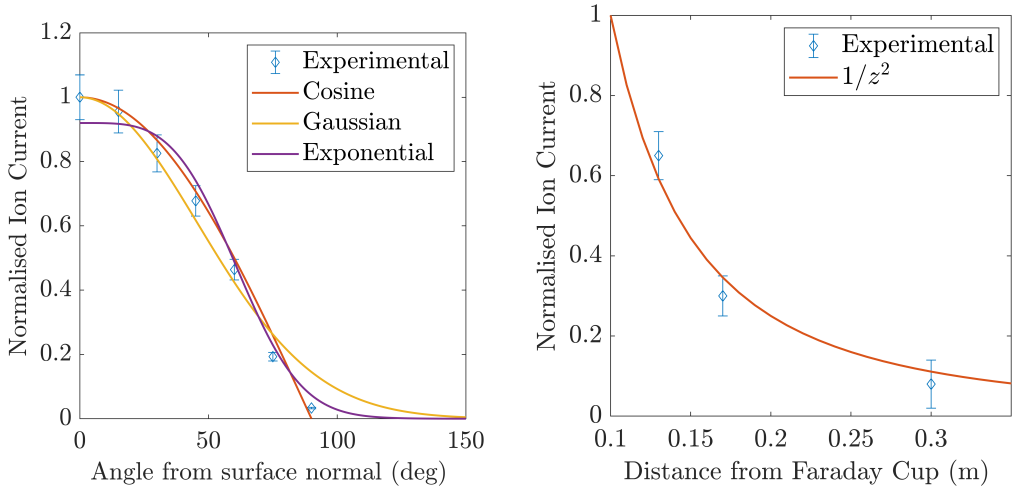

(a) **(b)**

Figure 6.18: ICDD measurements of VAT without the magnetic coil (a) Normalised angular ion distribution with fitted theoretical distributions with the closest correlation to the cosine ICDD. (b) Normalised radial ion density distribution for various probe distances which drops according to $1/z^2$.

Table 6.4: Surface fitting results for angular and radial ion distributions

Fit	RMSE	Spread Factors	R^2
Cosine	0.032	-	0.99
Exponential	0.047	3.6 ± 0.48	0.98
Gaussian	0.063	0.77 ± 0.11	0.97

ICDD in Section 3.3. The results show the highest amount of correlation with the cosine distribution, which is the most ideal distribution with the ion traveling in all directions at equal rates. Table 6.4 shows the results from the surface fitting analysis and shows that the cosine distribution has the highest R^2 which represents the proportion of the variation in the ion current that is predictable from the independent variables, and thus has the closest correlation between theoretical and experimental data.

These tests provided an initial verification of the procedures to be followed in the main experiment in which the magnetic field would be applied to the vacuum arc plasma.

Thrust Correction Factor

The thrust factor was calculated based on the ICDD for each set of experiments. The thrust factor C_T was obtained through an Adaptive Simpson quadrature and trapezoidal integration for each specific ICDD with imputs being the VAT geometries. Additionally,

the plasma shielding correction was applied for each VAT configuration with the presence of a magnetic coil. The final expression in determining the thrust factor for a ICDD ($\bar{J}$) with it's specified spread factors is shown as,

$$C_T = \frac{\bar{L}^2}{\pi} \int_0^{2\pi} \int_0^{2\pi} \int_0^{\bar{r}_a} \int_0^{1} \bar{J} \frac{1}{\bar{l}^2} dA_1 dA_2 \tag{6.5}$$

The derivation of this equation is shown in Appendix B.

The associated uncertainty of the thrust factor originated from various measurements:

- Uncertainty in thruster position ($\pm 1.8^\circ$)
- Noisy ion signals
- Uncertainty in spread factors for each ICDD
- Uncertainty in VAT dimensions and cathode height (± 0.01 mm)
- Plasma shielding correction factor (± 0.0183)

A Monte Carlo error propagation technique (Zhang 2020). was used in determining the effects of the mention uncertainties on the final thrust factor. A set of random data were generated within the limits of the uncertainties which follow a Normal distribution. These data were propagated through the curve fitting procedure as well as the analytical thrust factor calculation to determine the error for the worst cases. The results from the Monte Carlo error propagation were compared to those of the experimental error which was based purely on the uncertainties of the spread factors. The worst-case error of these data were then used in the results.

Shunt Resistor Selection

The tests conducted suggests that the circuit response is not only determined by the ions alone, but as well at the Faraday cup system itself. Various shunt resistor sizes were tested to evaluate the effects on the Faraday cup response to the plasma. Measurements of the ion current were taken with four different shunt resistors; 100 kΩ ($\pm 5\%$), 750 kΩ ($\pm 5\%$), 1 MΩ ($\pm 5\%$), and 2 MΩ ($\pm 5\%$).

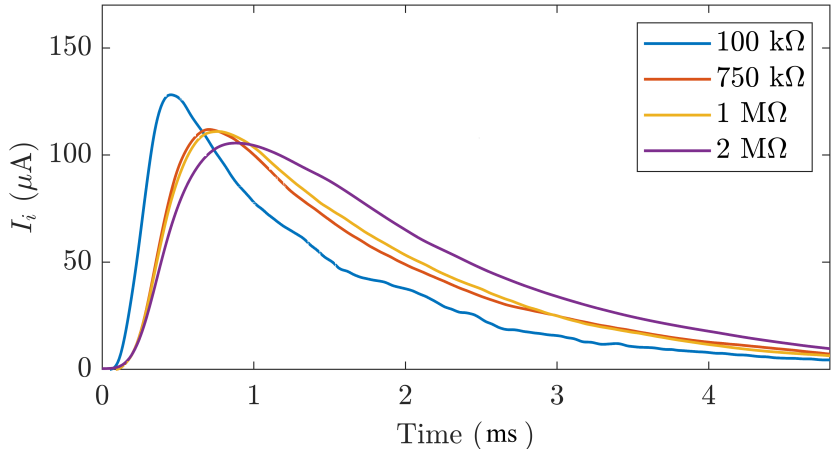

Figure 6.19: Observed ion current signals for four different shunt resistor values, these signals were processed and filtered to obtain maximum ion current values.

These tests revealed that the shunt resistor effected the response of the ion current signal produced by the same plasma configuration. The larger shunt resistor had a slower response time and lower ion current amplitude in comparison to that of the lower resistor which had a faster response time and higher ion current amplitude.

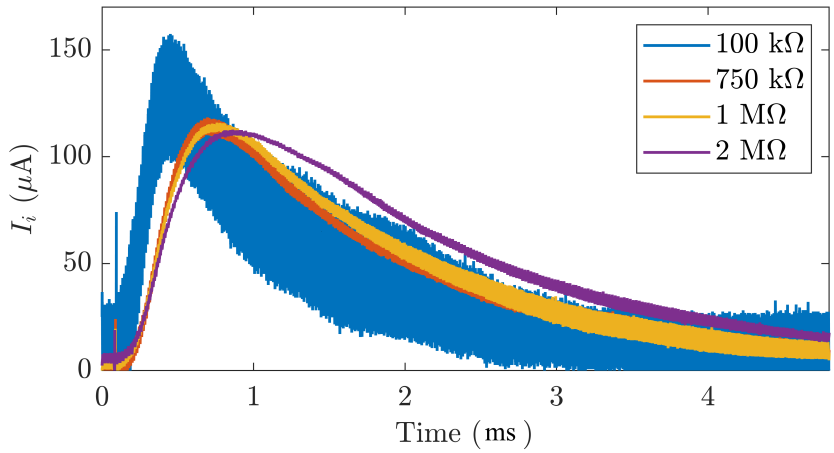

Figure 6.20: Raw data from ion current signals for four different resistor values.

The unfiltered data from the shunt resistors is shown in Figure 6.20. The lower shunt resistor produced a much worse signal-to-noise ratio than the rest. This measures the level of a desired signal to the level of background noise, and thus is important in obtaining accurate measurements of the ion current. It was decided that the 750 kΩ resistor was to be used to ensure a better signal-to-noise ratio with a compromise on the response time of the ion current signal.

Faraday Cup Current and Voltage

A DC boost converter was used with a typical dc power supply to bias the Faraday cup. Due to the AC to DC conversion from the mains, it was necessary to filter and clean the data in order to obtain accurate responses from the Faraday cup probe. To determine the proper biasing voltage for the Faraday cup to repel the impinging electrons, several tests were conducted with varying bias voltages. These tests were all conducted with the same material (Fe) at the same incidence angle (0°) while the Faraday cup was biases at 0 V, -80 V, -115 V, -200 V, -250 V, and -350 V. These results are shown in Figure 6.21.

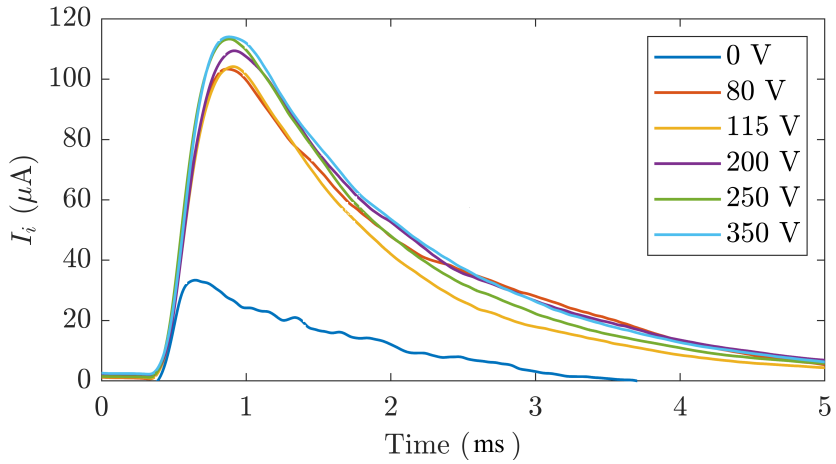

Figure 6.21: Various Faraday cup bias voltages between 0 - 350 V for baseline VAT with an iron cathode with a 750 kΩ shunt resistor for measurement.

The first observation made was that the increase in biased voltage correctly repelled the electrons away from the Faraday cup allowing the Faraday cup to generate a signal induced by the ions and a mixture of ions and electrons. A 0 V Faraday cup voltage shows to have a much lower voltage response as the cup is not repelling any of the electrons and thus is generating a signal induced by a mixture of ions and electrons. The mixture of electrons and ions result in lower ion signals due to the electrons canceling out a portion of the ion charges. The 80-115 V negative bias voltages produced very similar responses, which repel a the majority of the electrons within the plasma, however an increase to -200 V proved to increase the repulsion of the electrons from the Faraday cup. An increase in bias voltages greater than -250 V proved to have no increase in electron repulsion. It was concluded that a bias voltage of -250 V would be adequate for the biasing of the Faraday cup in order to obtain reliable results.

Chapter 7 Experimental Results

As mentioned in Section 6.6.4, the distribution of ions emitted from the vacuum arc discharge can be described by a cosine, exponential or Gaussian distribution. Polk et al. 2008 concluded that these distributions have a correlating thrust factor which relate ion distribution to the theoretical VAT thrust. The unmagnetised distributions result in approximately two thirds of the ions' momentum contributing to the overall thrust. The remaining ion momentum is thus self-canceling and has zero effect on the axial thrust. This quasi-neutral plasma generated by the VAT can be influenced by magnetic fields in order to guide the ions towards the center line of the thruster, increasing the overall axial thrust. To understand and analyse the effects of magnetic fields on VATs with different cathode materials, the unmagnetised VATs were tested to create a baseline for comparison. The main aim of these tests were to determine the variation in ion current distribution of a VAT with applied pulsed magnetic fields. These variations in ICDD can provide insight into possible improvements to VATs used today.

For each selected material (Fe, Al, and Cu), the peak ion-to-arc current ratio was normalised to a specified baseline ion-to-arc current ratio for each angle. These ratios are represented by $(J_{pk})_{ion}$. This produced an ICDD for each material for a given magnetic field strength. The process of normalising the ion-to-arc current was performed to gain a qualitative understanding of the variation in ICDD for each material and applied magnetic field. All tests were performed with identical circuit parameters, arc currents and sample sizes. A best surface fit was used to extrapolate and capture each distribution to a known ICDD function which can be directly evaluated in comparison to magnetised ICDDs.

7.1 Unmagnetised Ion Distribution

The unmagnetised baseline VAT tests demonstrated the effects of plasma shielding on the ICDD shown in Figure 7.1.

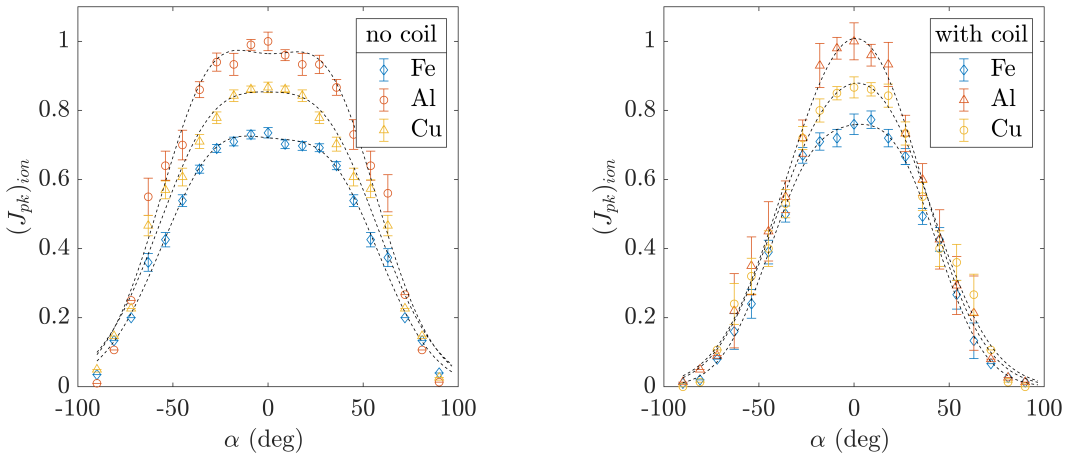

(a) **(b)**

Figure 7.1: Surface fits of ICDD data for baseline VAT operating with peak arc currents of 270 A with trend lines. (**a**) represents the surface fit for the baseline VAT without the magnetic coil attached. (**b**) represents the surface fit for the baseline VAT with the magnetic coil ($\vec{B}$ = 0 mT) to demonstrate plasma shielding.

The ICDDs were normalised to the peak ion-to-arc current ratio of the Al unmagnetised ICDD shown in Figure 7.1b.

Table 7.1: The surface fitting analysis for the unmagnetised ICDD witout the magnetic coil shows the fit type, spread factors, sum of squared errors (SSE), the coefficient of determination (R^2) and the root mean square error.

Cathode Material	Fit	Spread Factor	SSE	R^2	RMSE
Fe	Exponential	3.905 ± 0.141	0.010	0.992	0.023
Fe	Cosine	-	0.012	0.991	0.024
Fe	Gaussian	0.823 ± 0.056	0.050	0.962	0.050
Al	Exponential	3.899 ± 0.239	0.049	0.981	0.050
Al	Cosine	-	0.044	0.983	0.046
Al	Gaussian	0.819 ± 0.077	0.182	0.930	0.095
Cu	Exponential	3.997 ± 0.235	0.035	0.980	0.042
Cu	Cosine	-	0.024	0.987	0.033
Cu	Gaussian	0.829 ± 0.062	0.084	0.953	0.065

A surface fitting performance conducted on the unmagnetised ICDD without the magnetic coil was performed and can be found in Table 7.1. The surface fitting analysis was shown to

correlate closely to the typical ICDD functions presented in current literature. Fe was found to fit an exponential distribution where Al and Cu was best fitted to a cosine distribution.

The ICDD representd that angular variation in ion density which is directly related to the momentum properties of the ions. Significantly larger ICDD peaks were observed for the Al cathode for both unmagnetised baseline VATS. It is evident that this is a result of longer pulse lengths shown in Section 6.2.4. In general, it is understood that the ion production has a linear relationship to the arc current. Despite this, it is clear that the ICDD is effected by the arc pulse length as the effects of the arc currents were mitigated by evaluating all VAT performances with ion-to-arc current ratios. The Al cathode produces arc discharges of considerable longer pulse lengths which result in larger ion peaks and ICDDs which is present in Figure 7.1. The highest density of ions are found along the center line of the arc thruster with a drop off at higher angles from the center line.

The effects of plasma shielding are shown to have a significant effect on the shape of the ICDD distribution. The plasma shielding results in a narrower distribution of ions whilst the magnitude of the peaks remain consistent for each material. This however does not explain the drastic drop in ion current between $\pm 18^{\circ}$ and $\pm 36^{\circ}$. This occurrence could be a result of the plasma generating a current within the magnetic coil itself due to the emission of high velocity electrons. As the electrons travel at much greater velocities than the ions, the initial electrons emission could induce a current within the magnetic coil. The induced current within the magnetic coil in turn would generate a magnetic field directed along the center line of the thruster. The momentary magnetic field could could slight collimation of the slower ions under Lorentz forces.

Table 7.2: Results of best surface analysis with peak arc current, fit type, spread factors and correlation of determination as well as thrust factor for Fe, Al, and Cu unmagnetised ICDD without the attached magnetic coil.

Material	I_A (A)	Fit	Spread	R^2	t_p (ms)	C_T
Fe	269 $\pm$ 0.010	Exp	3.905 $\pm$ 0.141	0.992	3.44 $\pm$ 9$\times 10^{-7}$	0.67 $\pm$ 0.009
Al	277 $\pm$ 0.003	Cos	-	0.983	4.59 $\pm$ 1$\times 10^{-7}$	0.67
Cu	274 $\pm$ 0.004	Cos	-	0.987	3.66 $\pm$ 3$\times 10^{-7}$	0.67

The results obtained through the experiments allowed for a curve fitting analysis to be performed and thus be compared to published data on thrust factors. The ICDD for Fe was found to best fit an exponential distribution with C_T = 0.668 (4.4% higher than C_T published by Polk et al. 2008). Al and Cu was best fitted to a cosine distribution with C_T = 0.667 which is in agreement to the published C_T by (Polk et al. 2008). These tests were conducted without the presence of the magnetic coil.

Once the unmagnetised VAT ICDD was measured, it was imperative to determine the ICDD of the VAT with the magnetic coil. This was done to establish a baseline ICDD for later qualitative comparison.

The thrust factor for the unmagnetised ICDD with the magnetic coil attached was considerable influenced by the magnetic coil, these are shown in Table 7.3. The thrust factor of the magnetised baseline VAT with the attached magnetic coil required the inclusion of the thrust factor for plasma shielding as shown in Section 5.5.1.

Table 7.3: Results of best surface analysis with peak arc current, fit type, spread factors and correlation of determination as well as thrust factor for Fe, Al, and Cu unmagnetised ICDD with the attached magnetic coil.

Material	I_A (A)	Fit	Spread	R^2	t_p (ms)	C_t
Fe	277 $\pm$ 0.06	Exp	2.505 $\pm$ 0.164	0.986	3.43 $\pm$ 9$\times10^{-6}$	0.63 $\pm$ 0.012
Al	278 $\pm$ 0.06	Gaus	0.602 $\pm$ 0.018	0.994	4.32 $\pm$ 5$\times10^{-6}$	0.59 $\pm$ 0.008
Cu	277 $\pm$ 0.01	Gaus	0.640 $\pm$ 0.030	0.985	3.58 $\pm$ 1$\times10^{-6}$	0.58 $\pm$ 0.013

As can be seen in Table 7.3, the effects of plasma shielding effect the ICDD distribution. The thrust factor of the magnetised plasma with the magnetic coil prove to be lower due to plasma shielding with consistent peak ion currents. These tests provided a baseline for magnetic testing in which direct comparison could be made.

7.2 Magnetic Ion Current Density Distributions

Once the unmagnetised baseline VAT configurations were tested, the magnetised VAT configurations were tested in order to correlate the change in ICDD with magnetic field strengths. The magnetic field strengths applied in the experiment were 0 mT, 150 mT, and 250 mT. It must be noted that all ICDDs have been normalised to Al's unmagnetised maximum ion current for direct qualitative comparison.

7.2.1 Magnetised Fe ICDD

It was observed that the application of a magnetic field had a considerable effect on the Fe ICDD as shown in Figure 7.2. The initial application $\vec{B} = 150$ mT resulted in a 28.5% increase in peak ICDD. The application of a $\vec{B} = 250$ mT resulted in an additional increase in peak ICDD of 12.2%, with a total increase of 41% increase from the baseline unmagnetised ICDD. This is a significant increase as the number of ions along the center line has increased dramatically in comparison to the unmagnetised VAT.

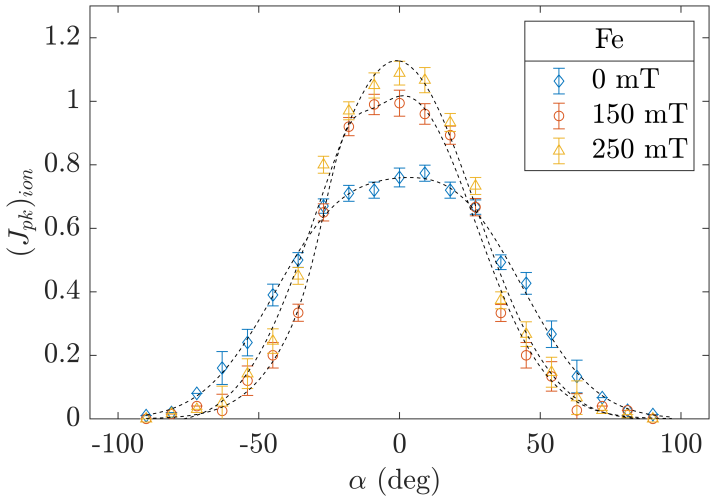

Figure 7.2: Experimental results of normalised Fe ICDD with $\vec{B} = 0$ mT, $\vec{B} = 150$ mT, and $\vec{B} = 250$ mT with trend lines.

A summary of the curve fitting analysis for Fe is presented in Table 7.4.

Table 7.4: Surface fitting analysis for magnetised Fe ICDD with fit type, spread factors, correlation of determination, RMSE, peak ICDD and percentage increase relative to baseline ICDD.

Fit Type	$\vec{B}$ (mT)	Spread Factors	R^2	SSE	RMSE	Max $(I_{pk})_{ion}$	% increase
Exp	0	2.505 $\pm$ 0.164	0.986	0.026	0.036	0.77 $\pm$ 0.03	-
Gaus	150	0.449 $\pm$ 0.024	0.988	0.039	0.044	0.99 $\pm$ 0.04	28.5
Gaus	250	0.469 $\pm$ 0.022	0.991	0.035	0.042	1.09 $\pm$ 0.04	40.7

The curve fitting analysis shows that both magnetised VAT configurations was best fit to a Gaussian distribution.

7.2.2 Magnetised Cu ICDD

Figure 7.3 shows the Cu ICDD, and demonstrates that the effect of the applied magnetic field has a less significant effect on comparison to that of the Fe cathode VAT. The maximum percentage increase for the Cu VAT is shown to be ∼20% which is a significantly lower percentage increase in maximum ion current at $\vec{B}$ =250 mT in comparison to that of the Fe cathode. However, the magnitude of the maximum ICDD was similar to that of the Fe cathode.

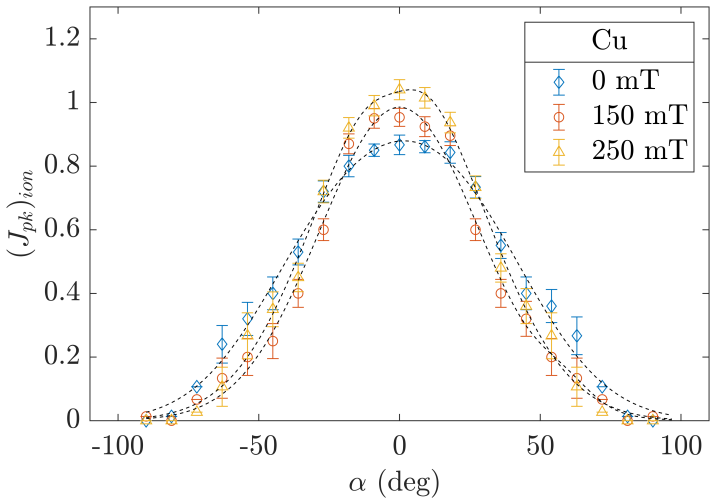

Figure 7.3: Experimental results of normalised Cu ICDD with $\vec{B}$ = 0 mT, $\vec{B}$ =150 mT, and $\vec{B}$ =250 mT with trend lines.

The curve fitting analysis shows that all magnetic configurations follow a Gaussian distribution with R^2 values between 0.985 - 0.993. Similar to that of the Fe VAT, the peak of the magnetised ICDDs were increased in comparison to the unmagnetised baseline VAT.

Table 7.5: Surface fitting analysis for magnetised Cu ICDD with fit type, pread factors, correlation of determination, RMSE, peak ICDD and percentage increase relative to baseline ICDD.

Fit Type	$\vec{B}$ (mT)	Spread Factor	R^2	SSE	RMSE	Max $(I_{pk})_{ion}$	% increase
Gaus	0	0.641 ± 0.032	0.985	0.032	0.040	0.867 ± 0.03	-
Gaus	150	0.506 ± 0.024	0.989	0.031	0.039	0.953 ± 0.028	9.9
Gaus	250	0.526 ± 0.021	0.993	0.023	0.034	1.040 ± 0.03	20.0

At angles beyond ±27°, the ICDD magnitudes are shown to reverse such that as higher the magnetic field strength configurations have lower ion currents. This suggests that the ions within the plasma are diverted from higher angles to lower angles along the center line, thus resulting in a lower ion current at higher angles from the center line.

7.2.3 Magnetised Al ICDD

Similar to that of the Cu cathode, the Al percentage increase between magnetic field strengths is increased consistently in ∼10% increments. Al has the highest max ICDD of the materials with a normalised ion current of 1.23 with $\vec{B} = 250$ mT.

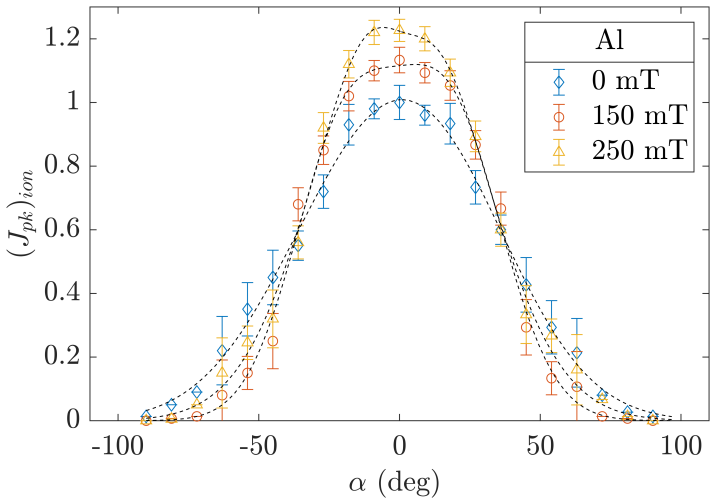

Figure 7.4: Experimental results of normalised Al ICDD with $\vec{B}$ =0 mT, $\vec{B}$ =150 mT, and $\vec{B}$ =250 mT with trend lines.

The Al VAT curve fitting analysis shows that the $\vec{B}$ =250 mT ICDD is best fitted with a Gaussian distribution with an R^2 value of 0.992 with an percentage increase in max ICDD of 22.3%. This is significantly less than that of the percentage increase of the Fe VAT however remains to have the highest overall ICDD of all the materials tested.

Table 7.6: Surface fitting analysis for magnetised Al ICDD with fit type, pread factors, correlation of determination, RMSE, peak ICDD and percentage increase relative to baseline ICDD.

Fit Type	$\vec{B}$ (mT)	Spread Factor	R^2	SSE	RMSE	Max $(I_{pk})_{ion}$	% increase
Gaus	0	0.602 ± 0.018	0.994	0.016	0.029	1.000 ± 0.054	-
Exp	150	1.651 ± 0.097	0.991	0.037	0.043	1.133 ± 0.040	13.3
Gaus	250	0.514 ± 0.020	0.992	0.035	0.042	1.227 ± 0.035	22.67

7.2.4 Magnetic Field Performance

The results demonstrate that the magnetic field has a considerable effect on the overall ICDD for each material. Figure 7.5 shows the ICDDs for the applied magnetic fields on each material VAT. A consistent observation for all cathode materials is the angle at which the unmagnetised ICDD exceeds that of the magnetised ICDDs. The magnetised ion currents are greater at angles between -33° and +29° for Fe, between -38° and +38° for Al, and between -29° and +29° for Cu. In all cases the unmagnetised ion current is greater beyond these limits providing insight into the behavior of the ejected ions within the plasma.

In attempting to answer the research question, the relationship between the peak ICDD and the magnetic field was done. Figure 7.5 shows the ICDDs for each magnetic field for a given cathode material.

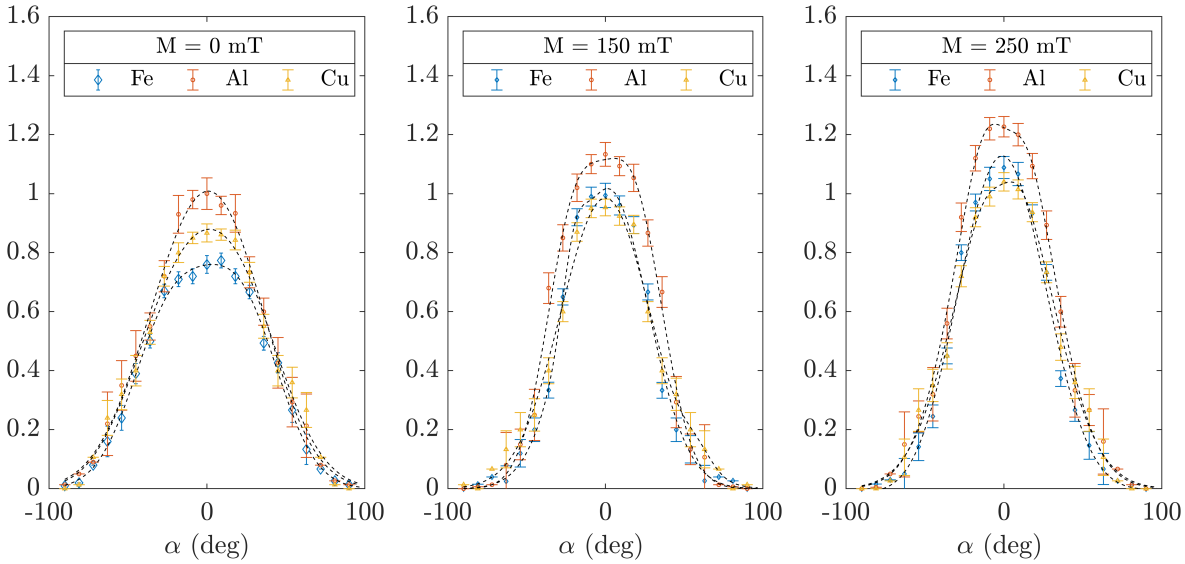

Figure 7.5: Experimental results of normalised ICDDs for Fe, Al and Cu for (**a**) $\vec{B}$ =0 mT, (**b**) $\vec{B}$ =150 mT and (**c**) $\vec{B}$ =250 mT. All results were normalised to the maximum Al unmagnetised ICDD with the magnetic coil attached with trend lines.

The application of the magnetic field resulted in a narrowing of the ICDD for each cathode material. The magnetic peak ion current for Al proves to remain the highest for all magnetic fields with the Fe having a greater peak ion current that Cu when magnetised. This can be seen in Figure 7.6.

The relationship of the max ICDD and magnetic field strengths were found to be linear for all cathode materials tested as shown in Figure 7.6. The Al cathode has the highest max ICDD for all magnetic field strengths, with Fe have the greatest percentage increase of all the materials.

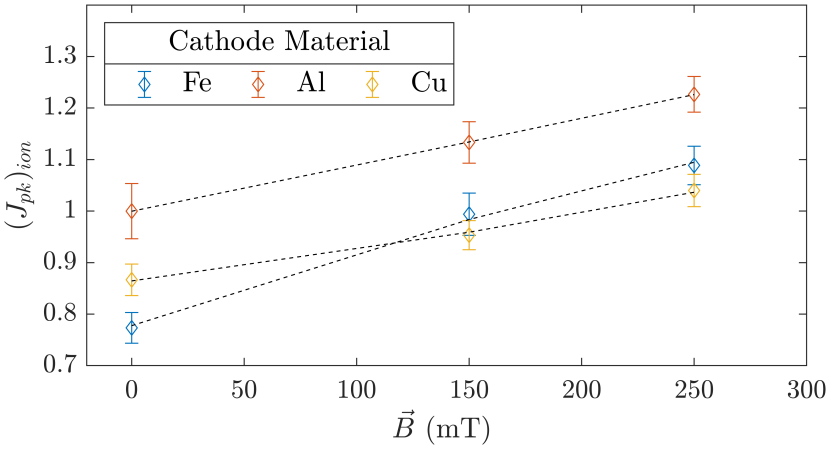

Figure 7.6: Summary of max ICDDs for Fe, Cu and Al for all magnetic field strengths and fitted slopes for each relationship.

Figure 7.6 represents the relationship between the peak ion current and magnetic field for Fe, Al, and Cu, however this is of less importance in comparison to the associated theoretical thrust factors.

Table 7.7: Results of best surface analysis with peak arc current, fit type, spread factors and correlation of determination as well as thrust factor for Fe, Al, and Cu magnetised ICDD woth applied magnetic field strength of 150 mT

Material	I_A (A)	Fit	Spread	R^2	t_p (ms)	C_t
Fe	274 $\pm$ 0.51	Gaus	0.449 $\pm$ 0.024	0.988	3.38 $\pm$ 6$\times 10^{-5}$	0.68 $\pm$ 0.013
Al	280 $\pm$ 0.21	Exp	1.651 $\pm$ 0.097	0.991	4.21 $\pm$ 4$\times 10^{-5}$	0.70 $\pm$ 0.007
Cu	279 $\pm$ 0.07	Gaus	0.506 $\pm$ 0.024	0.989	3.72 $\pm$ 6$\times 10^{-6}$	0.65 $\pm$ 0.013

Percentage increases in thrust factors of 6.3%, 16.4% and 10.8% for Fe, Al and Cu respectively were observed when applying a pulsed magnetic field of 150 mT. These percentage increases were based on the thrust factors of the unmagnetised plasma VATs with the coil attached. The Al VAT had the greatest percentage increase, where the Fe cathode had the lowest. It was observed that the magnetic field has insignificant affects on the peak arc current and pulse length. Higher arc current and pulse lengths are generally observed by the application of a magnetic field to the PPU circuit. The power requirement of including the magnetic coil to the PPU reduce the power load to the thruster and thus decrease the arc current and increase to pulse length due to added inductance of the coil. The magnetic field, in this study, was powered by a completely separate driving circuit and thus had minimal influence on the arc currents and pulse lengths of the arc discharge.

Table 7.8 show the results for the magnetised ICDD with $\vec{B}$ =250 mT. The application of $\vec{B}$ =250 mT showed to produce a lower thrust factor for all materials in comparison to $\vec{B}$ =150 mT.

Table 7.8: Results of best surface analysis with peak arc current, fit type, spread factors and correlation of determination as well as thrust factor for Fe, Al, and Cu magnetised ICDD with $\vec{B}$ =250 mT

Material	I_A (A)	Fit	Spread	R^2	t_p (ms)	C_t
Fe	270 ± 1.61	Gaus	0.469 ± 0.0215	0.991	$3.32 \pm 2\times10^{-4}$	0.66 ± 0.011
Al	277 ± 0.40	Gaus	0.514 ± 0.020	0.992	$4.29 \pm 7\times10^{-5}$	0.64 ± 0.010
Cu	279 ± 0.21	Gaus	0.526 ± 0.019	0.993	$3.69 \pm 2\times10^{-5}$	0.63 ± 0.009

This is supported by the findings in Kronhaus, Chowdhury and Laterza 2019, who found that the greatest increase in thrust was observed for magnetic field strengths of 120 mT, with substantially lower values either higher or lower magnetic fields. Despite a decrease in thrust factor from $\vec{B}$ = 150 mT to $\vec{B}$ = 250 mT, the application of $\vec{B}$ = 250 mT yields an improvement to the unmagnetised VAT.

Chapter 8 Discussion

As shown in Section 7, the application of a pulsed magnetic field demonstrably affected the overall ICDD of a VAT plasma plume of various materials. It was demonstrated that the there is a linear relationship between the maximum ICDD and the magnetic field strength applied to the plasma plume, this in turn affect the directional momentum of the ions and thus increases the thrust.

8.1 Baseline VAT Performance

An inductive energy storage PPU was implemented in generating the vacuum arc discharges for the VAT. The operation of the VAT during experimentation was found to be reliable with consistent arcing with Fe, Al, and Cu cathodes. The initial design process of the PPU required the testing of various inductors, capacitors and supply voltages. The PPU design with a 500 μH inductance, 2000 μF capacitance with an inductor charging time between 85-100 μs proved to produce reliable, high vacuum arc discharge at low frequencies. The inductance charging periods were varied to eliminate misfires which were found to be predominant with the Al cathode VAT. Misfiring was observed for tests which were run for $>$ 3000 pulses.

8.2 Ion Current Density Distribution

The ICDDs for the unmagnetised baseline VAT proved to correlate closely with typical distribution functions in current literature. The ICDDs were considerably influenced by the presence of an attached magnetic coil around the anode of the baseline thruster. This influence is a result of plasma shielding in which the ejected ions are deposited onto the inner walls of the magnetic coil. The ions deposited on the inner walls thus have zero contribution to the overall momentum of the plasma plume. The thrust factor was found

to decrease for each material due to plasma shielding of ions at high angles from the normal, regardless of the current within the magnetic coil. This finding is supported by the ICDDs found by Chowdhury and Kronhaus 2020. However, a higher degree of collimation was found for plasma shielding by a magnetic coil. This could be due to the initial current induced within the magnetic field due to fast emission electrons within the plasma which generates a magnetic field resulting in ion collimation. The induction of the magnetic field resulted in collimation, however is not great enough to result in any considerable increases in ion-to-arc current ratios.

An additional consequence of plasma shielding is the continuous deposition of ions on the inner walls of the magnetic coil. This would prove to be detrimental for any thruster design which is required to operate for long periods of time. The ion deposition would accumulate after time and result in a layer of cathode metal on the inner wall of the coil.

Larger ion-to-arc current ratios were observed for the Al cathode. The larger ratios are due to the longer average arc pulse lengths produce by the Al cathode. It must be noted that the pulse lengths of the arc discharges for the materials are a consequence of the PPU parameters required to produce a desired peak arc current. This was discussed by Lun 2015 where the increase in pulse length results in an increase in ion production based on a material's thermal properties.

8.3 Magnetic VAT Performance

Increase ICDDs were observed with the application of a pulsed magnetic field to the VAT plasma plume. The application af the applied magnetic field had minimal effects on the pulse length of the VAT discharges and thus the increase ICDD cannot be attributed to an increase pulse length duration. The application of the magnetic field resulted in an increase number of ions being collected at angles close to the normal of the thrust. This suggests that the ions within the plasma are are subjected to accelerations which diminish the influence of ion acceleration on the charge separation.

As stated by the Lorentz Equation, (Equation 3.19), the acceleration of the charged particle is directly proportional to the charge-to-mass ratio as well as the ejection velocity. These can be found in Table 8.1. The thrust presented in Table 8.1, was determined by Polk et al. 2008, and demonstrates the relative thrust performance of these cathode materials for an unmagnetised VAT.

Table 8.1: Ion charge-to-mass ratios, ion velocity and thrust predicted performance of Vacuum Arc Thrusters (Polk et al. 2008).

Material	Q/M (C/mg)	V (m/s)	T (mN)
Fe	3.14	11800	2.5
Al	6.16	15400	3.2
Cu	3.09	12800	2.7

Al has both the highest charge-to-mass ratio and ejection velocity which in turn results in a higher degree of ion collimation. As the ions are ejected from the cathode spot, the influence of the magnetic field causes the ions to travel in a helical path in the direction of the magnetic field lines. The charged particles are magnetically confined to a helical path, the greater the magnetic field, the smaller the helical radius, or the Larmor radius. This results in a greater ion density along the thruster center line. Percentage increases in thrust factors of 6.3%, 16.5% and 10.8% for Fe, Al and Cu respectively were observed when applying a pulsed magnetic field of $\vec{B} = 150$ mT. The Al VAT had the greatest percentage increase, where the Fe cathode had the lowest. This supports the theory of an ion being subjected to greater accelerations with a greater charge-to-mass ratio.

An interesting observation made was the effects of higher magnetic fields on the VAT plasma discharge. The application of $\vec{B} = 250$ mT showed to produce a lower thrust factor for all materials in comparison to $\vec{B}$ =150 mT. Percentage increases in thrust factors of 4.3%, 6.9% and 8.8% for Fe, Al and Cu respectively were observed when applying $\vec{B} = 250$ mT. Despite the increase in thrust in comparison to the unmagnetised VAT, the resultant thrust factors are lower than that of $\vec{B}$ =150 mT. Kronhaus, Chowdhury and Laterza 2019, found that the greatest increase in thrust was observed for magnetic field strengths of $\vec{B} \approx 120$ mT, with substantially lower values either higher or lower magnetic fields.

The ICDDs results show that the application af a $\vec{B} = 250$ mT result in a greater peak in ion-to-current ratio. However, a focus on the ion-to-current ratios at higher angles from the center line suggest that the ion-to-arc ratios are lower for the application of $\vec{B} = 150$ mT. This suggests that the application $\vec{B} = 250$ mT has a lower degree of ion collimation than that of $\vec{B} = 150$ mT.

A lower degree of ion collimation could be attributed to several factors:

1. One reason could be due to the acceleration of the electrons. The strong magnetic field results in a narrow collimation of electrons which are accelerated by the magnetic field. The applied magnetic field strengthens the charge separation between the ions and electrons which increase electric field. However in a strong magnetic field, the

electrons are subjected to accelerations which cause the charge separation to have diminished influence of the ion acceleration. This effect would be most predominant with ions ejected at angles perpendicular to the magnetic field. This would result in a greater acceleration of ions parallel to the center line and a lower acceleration of ion perpendicular to the center line.

2. Another reason could be due to the magnetisation of ejected electrons. The magnetic field may be strong enough to magnetise the electrons and guide them along the magnetic field lines. The charge separation results in the ions to diverge from the center line and eject at higher angles. This would result in an increase in ion distribution at higher angles from the center line.

The correlation between the thrust factor and the actual thrust can not be made by the ICDD functions alone. The effects of the magnetic fields on the ion velocity would need to be investigated in order to determine the momentum parameters of a magnetic VAT plasma plume. As derived by Polk et al. 2008 shown in Section 3.3.

The application of a magnetic field would result in an increase ion velocity due to increased charge separation and electric field strength. The determination of the ion velocity was out of the scope of this research, due to the ion signal distortions and short probe distances between (0.2 - 0.3 m) as well as long pulse lengths. Based on the pulse lengths, the resolution of the digital oscilloscope was inadequate for acceptable measurements.

8.4 Summary

The application of a pulsed magnetic field to a VAT discharge proved to collimate the ion expansion resulting in lower momentum losses. The magnetic field improvement was counteracted by the ion momentum loss through plasma shielding. Despite the losses in ion momentum, increases in thrust factor for all magnetic fields were observed for all cathode material The application of $\vec{B} = 150$ mT yielded the greatest improvement in thrust factor with a percentage increase in 6.3% for Fe, 16.4% for Al, and 10.8% for Cu. Al had the greatest improvement in thrust factor due to it's thermal and electrical properties.

This increase in thrust factor would result in an increase in VAT thrust, purely based on the distribution of ions within the plasma plume. A quantitative comparison of actual thrust production for these configurations would require the measurement of the ion velocity due axial magnetic fields, however this was out of the scope of the research.

8.5 Further Development

Apart from the investigated measures for the application of pulse magnetic field to vacuum arc discharges, several potential areas could be further investigated to either increase VAT performance, or gain insight into VAT operation.

Investigations on the effects of magnetic fields were found to have a correlation to typical VAT cathode materials. A study on a wider range of cathode materials could aid in understanding what material property is most beneficial for magnetic VATs. This could be achieved by incorporating metal alloys which have a wider range of properties that can be altered to incorporate physical properties of various materials. Copper-impregnated graphite compounds allows for a much wider range of metal alloys and could be considered as options for further improving thermal and electrical property performance of cathodes.

Arc current performances could be extended to understand the effects of arc current magnitudes and pulse lengths on magnetised VAT performances. Peak arc discharge currents and pulse lengths were kept relatively consistent throughout this study and a further investigation could provide beneficial alternatives and understanding to magnetised VAT operations for various arc currents and pulse lengths.

The consequential plasma shielding due to the magnetic coil prove that a more efficient magnetic field generator would increase thrust drastically. This could be achieved by creating a tighter magnetic coil closer to the arc discharge, allowing for less turns required and a lower power requirement. The use of a tighter magnetic field in this study was not applicable due to the thermal heating of a smaller anode, which gives rise to another field of improvement.

Heat management of the VAT components could be investigated in the case of high arc currents with smaller anodes and cathodes. High currents result in high thermal heating, and thus a possible solution to this could increase the life-cycle of the VAT and the performance of a magnetised VAT with a tighter magnetic coil.

Direct thrust measurements of magnetised VATs could aid in understanding the consequence of plasma shielding. The indirect thrust measurement approach often taken relies on surface fitting of ion current distributions, this can be improved by directly measuring the thrust production as well as the associated ion velocity of magnetised VATs. In this study, ion velocity was out of the scope, however would provide a greater insight into the dynamics of magnetised ions within the plume and how the ion velocity could affect the overall thrust of the magnetised VAT.

Chapter 9 Conclusions

In this study, we set out to investigate the effects of magnetic fields on ion density distribution within a vacuum arc plasma and how these distributions respond to different cathode materials. Our research objectives were centered around understanding the relationships between axial magnetic field strength and ion density distribution for various cathode materials with differing physical and thermophysical properties.

Through systematic experimentation and analysis, we made several significant observations:

- Plasma Shielding and Ion Density Distribution: We observed that the placement of the coil around the anode resulted in plasma shielding, causing the deposition of emitted ions onto the inner walls of the magnetic coil. This effect led to a narrower spread in the ion density distribution along the center line, maintaining a higher ion-to-arc current ratio. This phenomenon was consistent across different materials and independent of the applied current through the coil.
- Impact of Pulsed Magnetic Fields: Introducing a pulsed magnetic field to the vacuum arc thruster (VAT) had a profound impact on ion distribution. Increasing the magnetic field strength led to higher ion-to-arc current ratios along the normal direction and lower ratios perpendicular to the normal. This indicated that the magnetic field enhanced ion collimation and momentum along the thruster center line. The peak performance improvement was observed at a magnetic field strength of 150 mT.
- Performance Enhancement: The application of an externally-applied magnetic field yielded a substantial improvement in VAT performance. This enhancement, observed for all tested cathode materials (Fe, Al, and Cu), was attributed to ion acceleration under Lorentz forces. Cathode materials with higher charge-to-mass ratios exhibited the most significant improvement, achieving the highest peak ion-to-arc current ratios at all tested magnetic field strengths.

- Optimal Magnetic Field Strength: Our results indicated that an optimal magnetic field strength of around 150 mT produced the best overall performance improvement across different cathode materials. This finding underscores the importance of carefully selecting magnetic field parameters to achieve maximum enhancement without compromising the system's efficiency.

In conclusion, our study demonstrates that the application of pulsed magnetic fields can effectively modify ion density distributions within vacuum arc plasmas, resulting in enhanced thrust performance for various cathode materials. Our research sheds light on the intricate relationships between axial magnetic field strength, ion density distribution, and cathode material properties. The findings underscore the potential of magnetic field manipulation as a technique to optimize the efficiency of vacuum arc thrusters. Future investigations could delve deeper into ion velocities, erosion rates, and the broader implications for space propulsion systems.

Overall, this study contributes valuable insights to the field of plasma propulsion and presents avenues for further exploration and refinement of magnetized propulsion technologies.

Appendix A

Technical Drawings

Assembled VAT

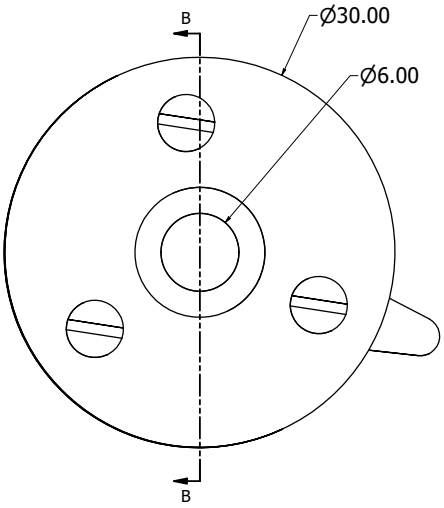

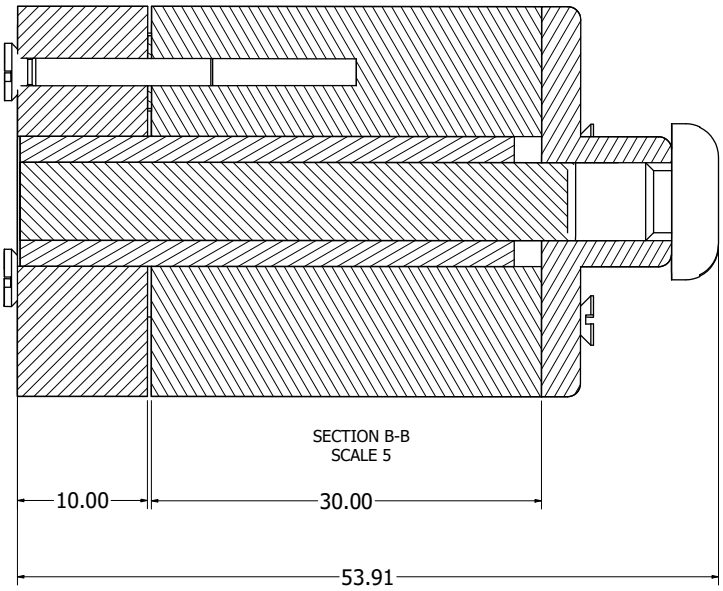

Front

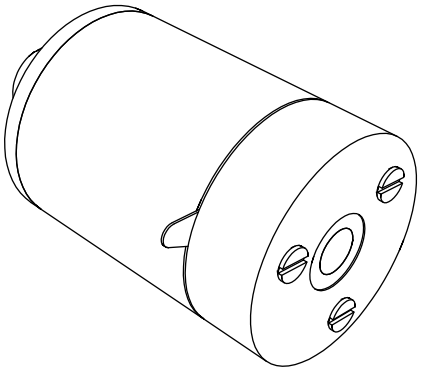

Back

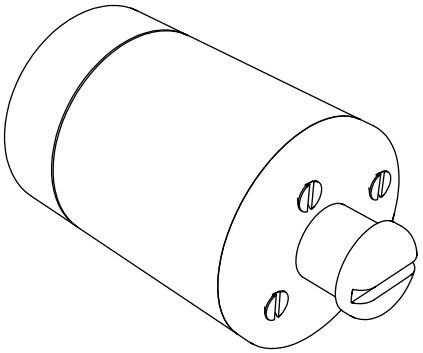

DRAWN Tristan Rencken	2023/03/09		
CHECKED		TITLE	VAT Assembly
QA			
MFG			
APPROVED		SIZE D	DWG NO ThrusterAssemblyCoilfull REV
		SCALE 5	SHEET 1 OF 4

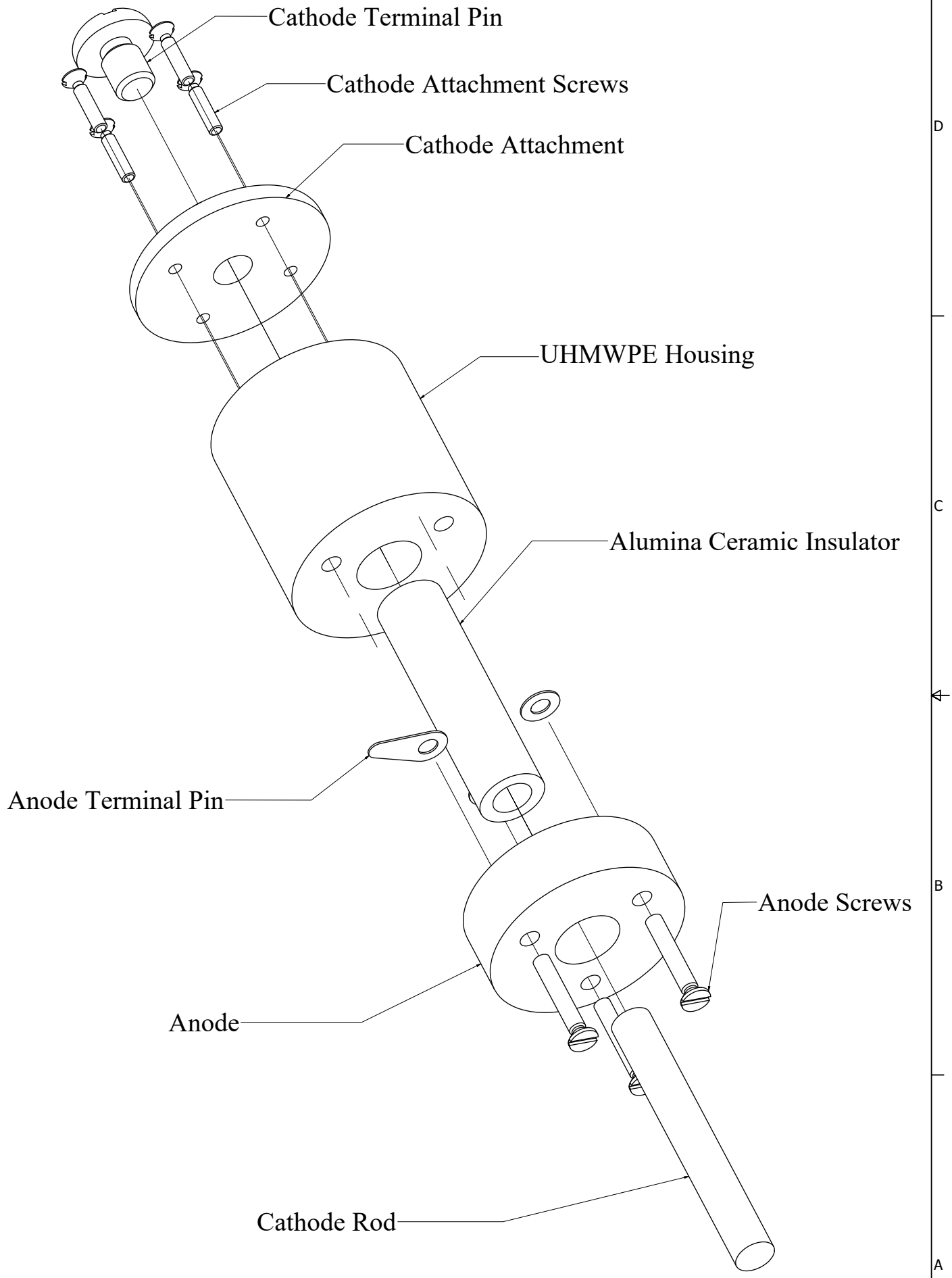

DRAWN Tristan Rencken	2023/03/09	
CHECKED		TITLE: VAT Exploded View
QA		
MFG		
APPROVED		
		SIZE D · DWG NO ThrusterAssemblyCoilfull · REV
		SCALE 4 · SHEET 2 OF 4

Anode

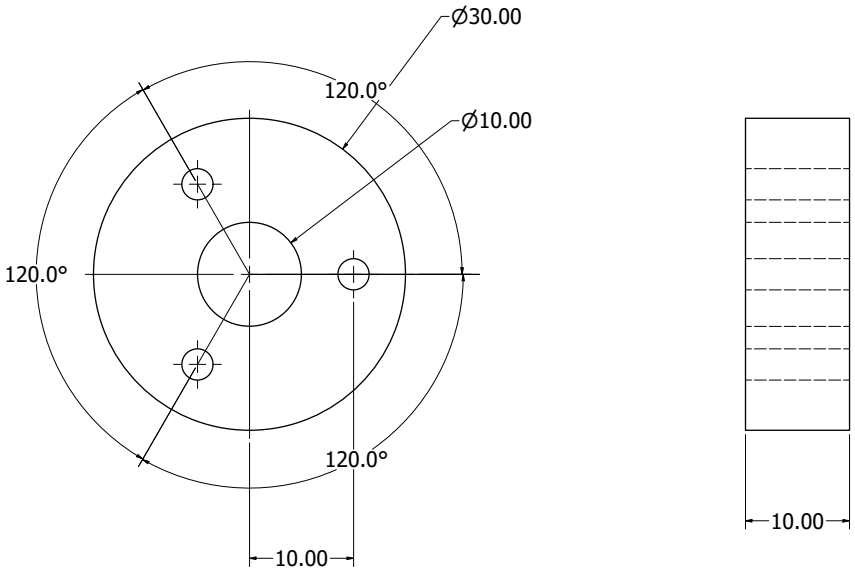

Insulator

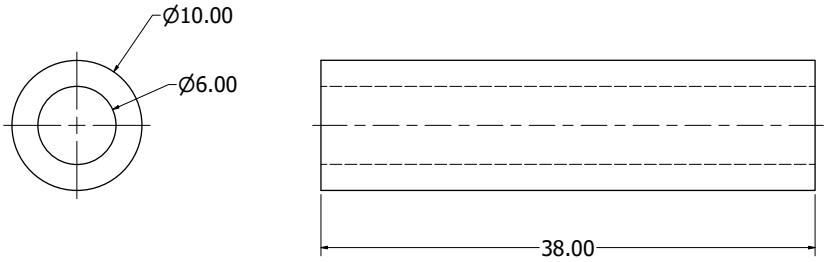

Cathode

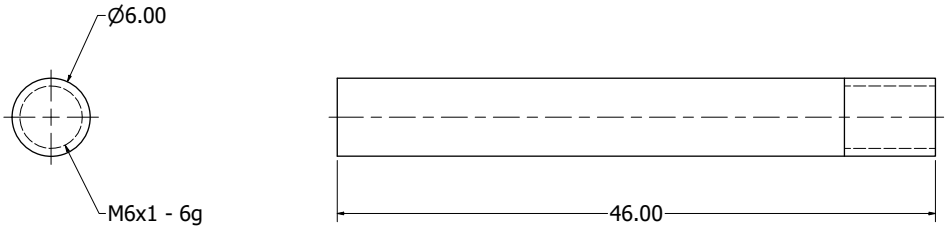

DRAWN Tristan Rencken	2023/03/09		
CHECKED		TITLE	VAT Components
QA			
MFG			
APPROVED		SIZE D	DWG NO ThrusterAssemblyCoilfull REV
		SCALE 4	SHEET 3 OF 4

Assembled Magnetic VAT

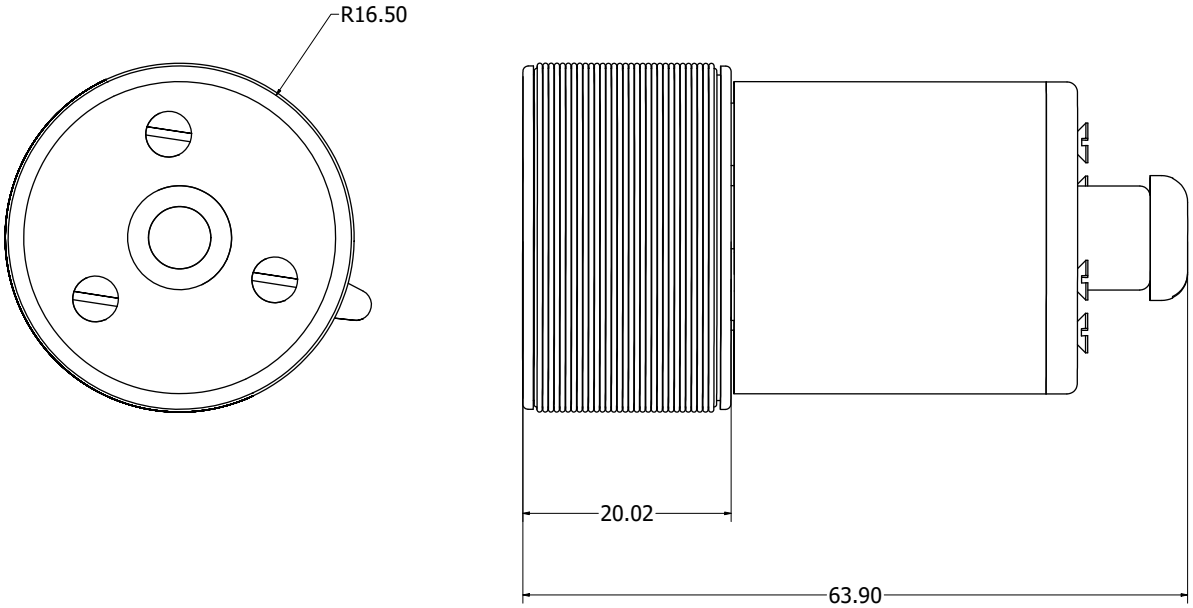

Front

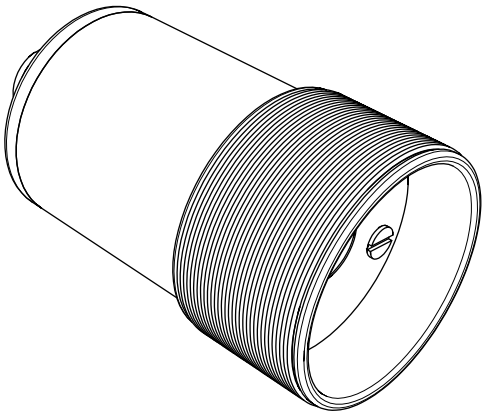

Back

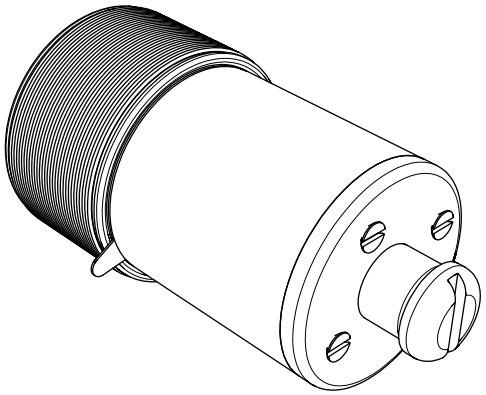

Magnetic Coil

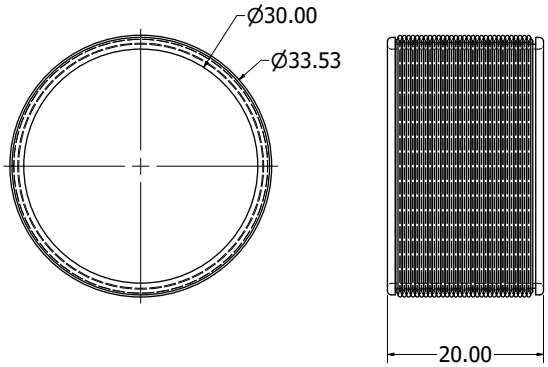

DRAWN Tristan Rencken	2023/03/09	
CHECKED		TITLE Magnetic VAT Assembly
QA		
MFG		
APPROVED		SIZE D / DWG NO ThrusterAssemblyCoilfull / REV
		SCALE 3 : 1 / SHEET 4 OF 4

Appendix B

Thrust Correction Factor

The thrust correction factor is used to calculate what proportion of the ions' total momentum is directed along the normal of the thruster which contributes to the overall thrust.This takes into account the plasma plume divergence, as well as the ion deposition of the cathode material on the inner walls of the anode. The cathode surface is assumed to uniformly emit ion current over the surface, which is only correct when represented by a large sample set mean. Each differential area on the cathode surface is assumed to produce an ion distribution which follows a cosine, Gaussian or exponential spacial distribution.

An expression for the ion density at a radius l and angle ϕ from the surface normal due to the mass generated in area dA_1 in the cathode surface can be described in polar coordinates based on Figure B.1,

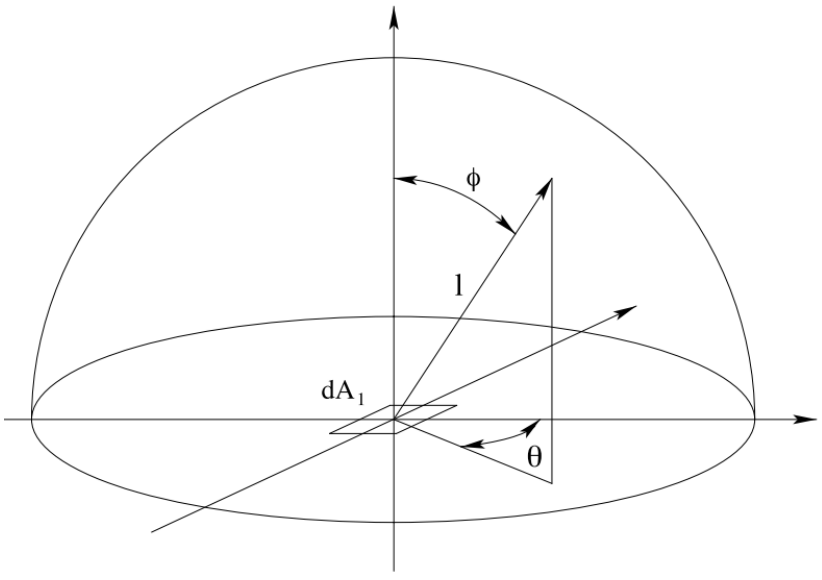

Figure B.1: Geometry used in defining ion current distribution (Polk et al. 2008)

and by the following distribution functions:

Exponential distribution (Polk et al. 2008):

$$j_{ip}(l,\phi) = \frac{j_{ic}2dA_1}{\sqrt{\pi}l^2 k\,\mathrm{erf}(2\pi/k)} \exp(-[2\pi(1-\cos\phi)]^2/k^2) \tag{9.1}$$

Gaussian distribution (Lun 2015):

$$j_{ip}(l,\phi) = \frac{j_{ic}dA_1}{\pi l^2} \exp\left(-\frac{\phi^2}{2w^2}\right) \tag{9.2}$$

Cosine distribution (Polk et al. 2008):

$$j_{ip}(l,\phi) = \frac{\cos\phi}{\pi l^2} j_{ic}dA_1 \tag{9.3}$$

These functions are graphically presented in Figure B.2, for the angular distribution and radial distribution of ions within a VAT plume. These functions have been normalised in order to present the shape of the distribution rather than the actual distribution of the ion density as this is dependent on a number of physical properties in experimentation. These functions were thus normalised to a value of $j_{ic}dA_1 = 1$.

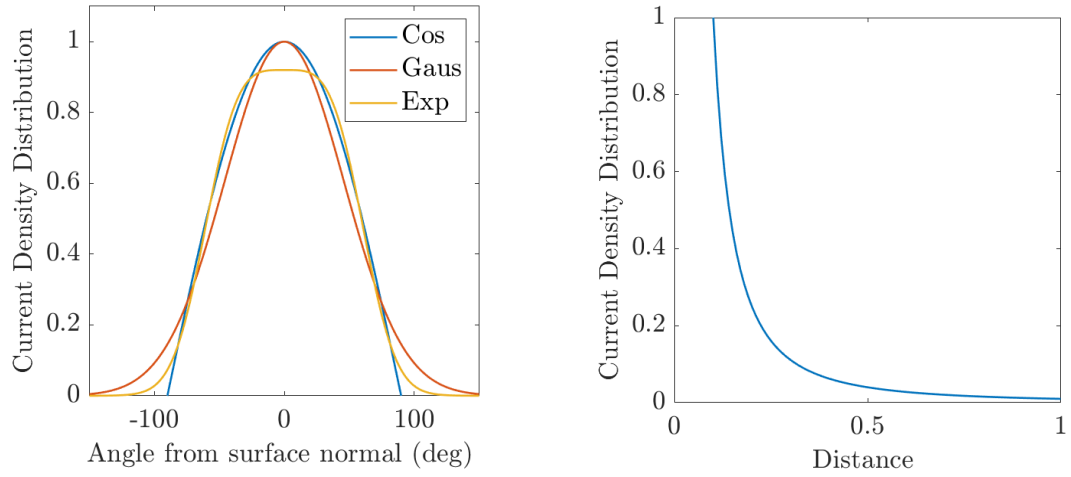

Figure B.2: Cosine, Gaussian and exponential distributions (**a**) Normalised angular ion density distributions for known typical VAT ICDDs. (**b**) Normalised radial ion distribution of theoretical distribution of $1/z^2$.

With the use of the above distribution functions, it is possible to determine the thrust correction factor to account for plume divergence and ion deposition on the anode walls.

The thrust factor is the ratio of axial ion momentum to total ion momentum emitted from the cathode surface dA_1. Ions are assumed to be emitted through the cathode surface i of area dA_1 with a normal vector n_i. Ions then travel through the anode plane j with area dA_2 and normal vector n_j. Defining a view factor between the surfaces can be represented by the line l between the anode and cathode, forming the angles θ_1 and θ_2. These are shown in Figure B.3.

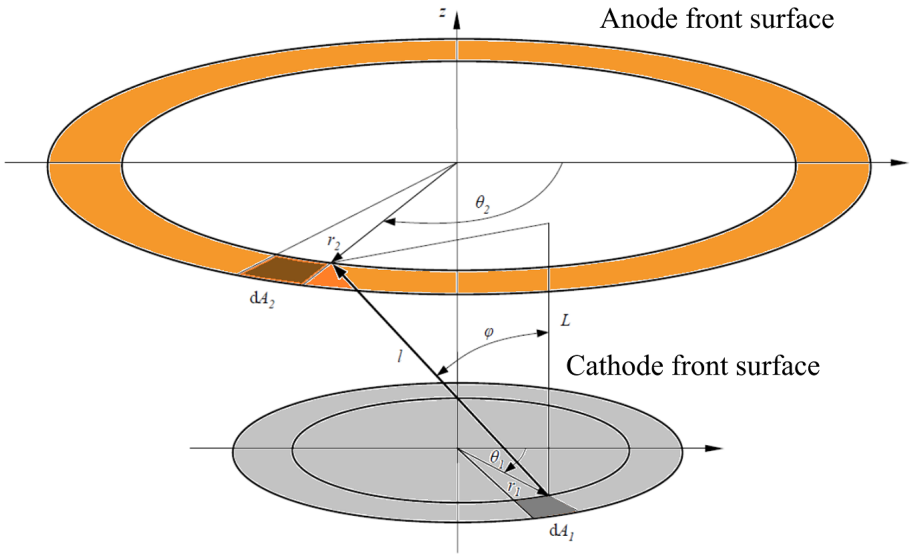

Figure B.3: Geometry used to calculate the momentum flux through the anode plane

By considering the rate of emission of ions from dA_1 and through dA_2, the current density J_{ij} can be represented as the rate of emission along the line l, per unit of emitting surface normal to this direction, per solid angle about this direction,

$$J_{ij} = \frac{dI_{ij}}{dA_1 cos\theta_1 d\omega_{ji}} \tag{9.4}$$

where ω_{ji} is the unit solid angle subtended by dA_2 viewed from dA_2,

$$d\omega_{ji} = \frac{cos\theta_2 dA_2}{l^2} \tag{9.5}$$

thus resulting in,

$$dI_{ij} = J_{ij} \frac{cos\theta_1 cos\theta_2}{l^2} dA_1 dA_2 \tag{9.6}$$

integrating over the cathode and anode surfaces provides the total rate of emission from polar coordinates,

$$I_{ij} = \int_{A_1} \int_{A_2} J_{ij} \frac{\cos\theta_1 \cos\theta_2}{l^2} dA_1 dA_2 \tag{9.7}$$

As mention previously, the thrust correction factor is the ratio of current emitted from the cathode (A_1) and travels through the exit plane of the anode (A_2),

$$C_T = \frac{I_{ij}}{A_1 J_{ic}} \tag{9.8}$$

for cases in which the cathode and anode planes are coplanar, $\theta_1 = \theta_2$. The distribution functions mentioned before are then normalised for unit drift length $l = 1$ and $J_{ij} = 1$, thus C_T can be expressed as,

$$C_T = \frac{1}{A_1} \int_{A_1} \int_{A_2} J' \cos^2\theta_1 dA_1 dA_2 \tag{9.9}$$

where $J' = J_{ij}/I_{ic}$. Based on the dimensions of the geometry shown in Figure B.3, the following expressions can be defined as,

$$\begin{aligned} A_1 &= \pi r_c^2 \\ \cos\theta_1 &= \frac{L}{l} \end{aligned} \tag{9.10}$$

which results in the simplified expression,

$$C_T = \frac{1}{\pi} \int_{A_1} \int_{A_2} J' \frac{L^2}{l^2} dA_1 dA_2 \tag{9.11}$$

Further non-dimensionalising the expression for any given sized circular geometry results in the following expression,

$$C_T = \frac{\bar{L}^2}{\pi} \int_0^{2\pi} \int_0^{2\pi} \int_0^{\bar{r}_a} \int_0^1 \bar{J}' \frac{1}{\bar{l}^2} \bar{r}_1 \bar{r}_2 d\bar{r}_1 d\bar{r}_2 d\theta_1 d\theta_2 \tag{9.12}$$

where,

$$
\begin{aligned}
r_c &= 1 \\
\overline{r_a} &= \frac{r_a}{r_c} \\
\overline{r_1} &= \frac{r_1}{r_c} \\
\overline{r_2} &= \frac{r_2}{r_c} \\
\bar{L} &= L/r_c \\
\bar{l}^2 &= \bar{L}^2 + \bar{r}_1^2 + \bar{r}_2^2 - 2\bar{r}_1\bar{r}_2\cos\left(\theta_1 - \theta_2\right)
\end{aligned}
\tag{9.13}
$$

and J' is any given distribution function.

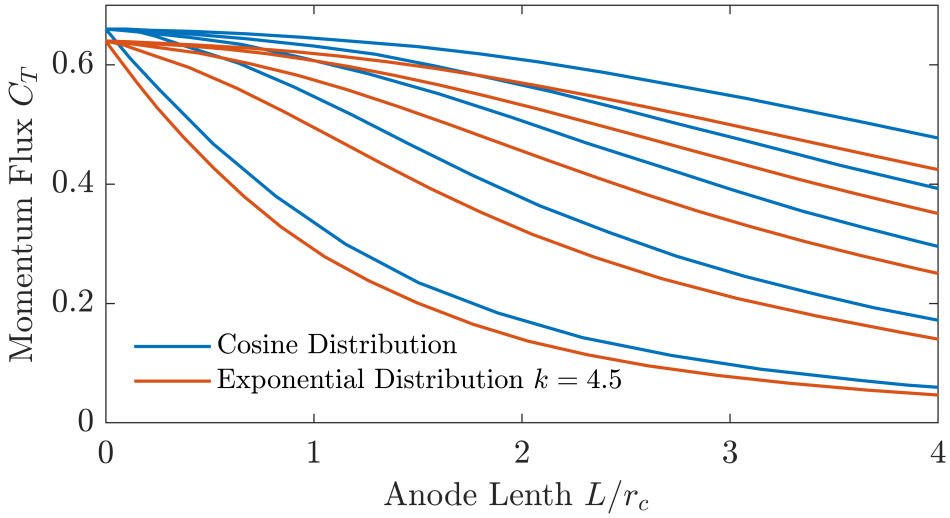

Figure B.4: Thrust factor which corrects for plume divergence and loss of plasma to anode walls for cosine distribution and exponential distribution with spread factor $k = 4.5$. (Polk et al. 2008)

Figure B.4 shows that a coplanar cathode and anode configuration results in the maximum C_T of 0.67 and 0.64 for cosine and exponential distributions respectively. In this study, a coplanar configuration was used for all tests and ensure by implementing a threaded connection on the cathode rod which could be adjusted after significant erosion.

The quadruple integral was solved numerically with an Adaptive Simpson quadrature and trapezoidal integration method. This was done such that the error could be specified to a specific tolerance though iterative methods.

Appendix C

Empirical VAT performance metrics

Properties for various cathode Vacuum arc thrusters used in performance estimation are presented in Table C.1. These samples were measured for 100 A pulsed discharges. The ion mass M_i is the mass of a singular ion species in AMU. The mean inverse charge represents the associated charge on a singular ion species with relation to the charge of an electrons in Coulombs. These values were not directly used in the determination of the thrust factors within this paper, however provided a baseline for early material selection based on their performances. These performance metrics were obtain by Polk et al. 2008, who concluded that comparisons with experimental data and semiempirical models reproduce the actual performance with reasonable accuracy and can be used for VAT thruster designs.

Table C.1: Material and Arc Properties for Potential Cathode Materials (Polk et al. 2008)

Species	Mass M_i (AMU)	Mean Inverse Charge State $< Z^{-1} >$	Erosion Rate Er $Er(\mu g/C)$	Ion-Fraction F_i	Discharge Voltage V_d	Ion Velocity u_i (m/s)
Li	6.941	1.00			23.5	23800
C	12	1.00	17	0.732	29.6	29700
Mg	24.305	0.66	31	0.528	18.8	30600
Al	26.981	0.58	28	0.577	23.6	29900
Si	28.086	0.72			27.5	25800
Ca	40.08	0.52			23.5	25900
Sc	44.96	0.56			19.1	
Ti	47,9	0.49	30	0.815	21.3	16700
V	50.94	0.47			22.5	19300
Cr	52	0.47	20	1.265	22.9	19400
Mn	54.94	0.66			22	10800
Fe	55.85	0.55	48	0.663	22.7	11800
Co	58.93	0.58	44	0.802	22.8	11800
Ni	58.71	0.56	47	0.736	20.5	10900
Cu	63.55	0.49	35	0.914	23.4	12800
Zn	65.38	0.83	320	0.176	15.5	10400
Ge	69.74	0.71			17.5	11000
Sr	87.62	0.50			18	
Y	88.91	0.44	45	0.898	18.1	14300
Zr	91.22	0.39	53	0.691	23.4	15700
Nb	92.91	0.33			27	15500
Mo	95.94	0.33	36	0.903	29.3	17400
Pd	106.4	0.53			21.3	15700
Ag	107.87	0.47	140	0.373	23.6	12500
Cd	112.41	0.77	620	0.142	16	6800
In	114.82	0.73			17.5	5500
Sn	118.69	0.66	295	0.273	17.5	7500
Ba	137.33	0.50			18.3	6700
La	138.91	0.45			17.2	7000
Ce	140.12	0.47			17.9	7000

Table C.2: Material and Arc Properties for Potential Cathode Materials (Polk et al. 2008)

Species	Mass M_i (AMU)	Mean Inverse Charge State $< Z^{-1} >$	Erosion Rate Er $Er(\mu g/C)$	Ion-Fraction F_i	Discharge Voltage V_d	Ion Velocity u_i (m/s)
Pr	140.91	0.44			20	8700
Nd	144.24	0.46			19.7	
Sm	150.4	0.47			14.6	7400
Gd	157.25	0.45	55	1.347	21.6	7400
Dy	162.5	0.43			19.8	7400
Ho	164.93	0.43			20	8300
Ho	164.93	0.43			20	8300
Er	167.26	0.42			19	8200
Yb	173.04	0,49			14.4	
Hf	178.49	0.34			24.3	9200
Ta	180.95	0.34	56	1.143	28.7	11100
W	183.85	0.32	55	1.111	31.9	14300
Ir	192.22	0.38			24.5	
Pt	195.09	0.48			22.5	6800
Au	196.97	0.51			19.7	5800
Pb	207.2	0.62	510	0.257	15.5	5400
Bi	208.98	0.84			15.6	4200
Th	232.04	0.17			23.3	9900
U	231.04	0.31			23.5	11400

References

Almurr, J. et al. (2022). 'Numerical investigations on the electric arc behavior upon contact opening in a low-voltage switch under the effect of external magnetic field'. In: *Electr. Power Syst. Res.* 209. ISSN: 03787796. DOI: 10.1016/J.EPSR.2022.107945.

Anders, A. (1998). 'Ion charge state distributions of pulsed vacuum arcs-interpretation of their temporal development'. In: *IEEE Trans. Plasma Sci.* 26.1, pp. 118–119. DOI: 10.1109/27.659541.

Anders, A. and G. Y. Yushkov (2002). 'Ion flux from vacuum arc cathode spots in the absence and presence of a magnetic field'. In: *J. Appl. Phys.* 91.8, pp. 4824–4832. ISSN: 00218979. DOI: 10.1063/1.1459619.

Bai, S. et al. (2021). 'Performance model of vacuum arc thruster with inductive energy storage circuit'. In: *Acta Astronaut.* 186, pp. 426–437. ISSN: 0094-5765. DOI: 10.1016/J.ACTAASTRO.2021.06.008.

Camps, A. (2019). 'Nanosatellites and Applications to Commercial and Scientific Missions'. In: *Satell. Mission. Technol. Geosci.* DOI: 10.5772/INTECHOPEN.90039.

Chiggiato, P. (2017). 'Outgassing properties of vacuum materials for particle accelerators'. In: *Glumslov*. arXiv: 2006.07124.

Chowdhury, S. and I. Kronhaus (2020). 'Characterization of Vacuum Arc Thruster Performance in Weak Magnetic Nozzle'. In: *Aerospace* 7.6. ISSN: 2226-4310. DOI: 10.3390/aerospace7060082.

Cui, W., W. Liu and Y. Gao (2019). 'A "self-triggered" arc initiation applied in vacuum arc thrusters'. In: *Europhys. Lett.* 125. DOI: 10.1209/0295-5075/125/15001.

Daalder, J. E. (1976). 'Components of cathode erosion in vacuum arcs'. In: *J. Phys. D Appl. Phys* 9. DOI: 10.1088/0022-3727/9/16/009.

Dennison et al. (2018). 'Real-Time Video Processing of Arcing Events to Determine Coincidence'. In.

Dethlefsen, R. (1968). 'Performance measurements on a pulsed vacuum arc thruster.' In: *https://doi.org/10.2514/3.4713* 6.6, pp. 1197–1199. ISSN: 00011452. DOI: 10.2514/3.4713.

Forster, R., C. Kirner and J. Schein (2023). 'Plasma Expansion Characterization of a Vacuum Arc Thruster with Stereo Imaging'. In: *Appl. Sci. 2023, Vol. 13, Page 2788* 13.5, p. 2788. ISSN: 2076-3417. DOI: 10.3390/APP13052788.

Gilmour, A. S. and D. L. Lockwood (1972). 'Pulsed Metallic-Plasma Generators'. In: *Proc. IEEE* 60.8, pp. 977–991. ISSN: 15582256. DOI: 10.1109/PROC.1972.8821.

Henry, G. N. et al. (1995). *Space Propulsion Analysis and Design*. Ed. by W. J. L. Gary N. Henry, Ronald W. Humble. illustrate. College custom series. McGraw-Hill. ISBN: 9780070313293.

Hiemstra, C. P. (2020). *Design, production, and validation of a vacuum arc thruster for in-orbit proximity operations*.

Keidar, M. et al. (2005). 'Magnetically enhanced vacuum arc thruster'. In: *Plasma Sources Sci. Technol.* 14.4, p. 661. ISSN: 0963-0252. DOI: 10.1088/0963-0252/14/4/004.

Kolbeck, J., A. Anders and I. I. Beilis (2019). 'Micro-propulsion based on vacuum arcs'. In: *J. Appl. Phys* 125, p. 220902. DOI: 10.1063/1.5081096.

Kolbeck, J., M. Keidar and A. Anders (2016). 'Micro-propulsion based on vacuum arcs: A review of physics and technology'. In: *52nd AIAA/SAE/ASEE Jt. Propuls. Conf. 2016*. American Institute of Aeronautics and Astronautics Inc, AIAA. ISBN: 9781624104060.

Kronhaus, I., S. Chowdhury and M. Laterza (2019). 'Axial Magnetic Field Effect on Vacuum Arc Thruster Performance'. In: *36th Int. Electr. Propuls. Conf.* arXiv: 1912.11657.

Kühn, M. and J. Schein (2022). 'Development of a High-Reliability Vacuum Arc Thruster System'. In: *https://doi.org/10.2514/1.B38202* 38.5, pp. 752–758. ISSN: 15333876. DOI: 10.2514/1.B38202.

Kühn, M., C. Toursel and J. Schein (2021). 'Thrust Measurements on the High Efficient and Reliable Vacuum Arc Thruster (HERVAT)'. In: *Appl. Sci.* 11.5. ISSN: 2076-3417. DOI: 10.3390/app11052274.

Kulu, E. (2023). *Spire - Satellite Constellation - NewSpace Index*.

Lafferty, J. M. (2003). 'Vacuum Arcs'. In: *Encycl. Phys. Sci. Technol.*, pp. 359–370. DOI: 10.1016/B0-12-227410-5/00804-8.

Larangot, B. et al. (2002). 'Solid Propellant MicroThruster : an alternative propulsion device for nanosatellite'. In.

Lee, Z. T. (2017). 'CubeSat constellation implementation and management using differential drag'. In.

Li, Y. H., J. Y. Pan and G. Herdrich (2020). 'Design and demonstration of micro-scale vacuum cathode arc thruster with inductive energy storage circuit'. In: *Acta Astronaut.* 172, pp. 33–46. ISSN: 0094-5765. DOI: 10.1016/J.ACTAASTRO.2020.03.012.

Lun, J. (2015). 'Performance Improvement of Vacuum Arc Thrusters'. In.

Michaux, E., S. Mazouffre and A. Blanchet (2022). 'Time evolution of plasma parameters in the jet of a low-power vacuum arc thruster'. In: *J. Electr. Propuls.* 1.1, p. 7. ISSN: 2731-4596. DOI: 10.1007/s44205-022-00007-w.

NASA (2018). *NASA Mission Supports Launch of CubeSats Built by Students — NASA*.

Pietzka, M. (2016). 'Development and Characterization of a Propulsion System for CubeSats based on Vacuum Arc Thrusters'. In.

Polk, J. E. et al. (2008). 'A Theoretical Analysis of Vacuum Arc Thruster and Vacuum Arc Ion Thruster Performance'. In: *IEEE Trans. Plasma Sci.* 36.5 PART 1, pp. 2167–2179. ISSN: 00933813. DOI: 10.1109/TPS.2008.2004374.

Qi, N. et al. (1998). 'A vacuum arc ion thruster for space propulsion, Technical report, Alameda Applied Sciences Corporation. SBIR Phase-I Final Report'. In.

Rumburg, J. (2014). *NASA's Science Mission Directorate Cubesat Initiative — NASA*.

Russel, J. (2020). *The Propulsion We're Supplying, It's Electrifying — NASA*.

Schein, J., N. Qi et al. (2002). 'Inductive energy storage driven vacuum arc thruster'. In: *Rev. Sci. Instrum.* 73.2 II, p. 925. ISSN: 00346748. DOI: 10.1063/1.1428784.

Schein, J., J. Zierhut et al. (2007). 'Improved plasma spray torch stability through multi-electrode design'. In: *Contrib. to Plasma Phys.* 47.7, pp. 498–504. ISSN: 08631042. DOI: 10.1002/CTPP.200710064.

Schein, J., A. Gerhan et al. (2003). 'Vacuum Arc Thruster for CubeSat Propulsion'. In: *28th Int. Electr. Propuls. Conf.*, IEPC–0276.

Sekerak, M. J. (2005). *Plasma plume characterization of a vacuum arc thruster*. Tech. rep. United States – California: California Institute of Technology. DOI: 305005127.

Spire, G. (2023). *Spire Weather - Spire : Global Data and Analytics*.

Tang, B. et al. (2005). 'Thrust Improvement of the Magnetically Enhanced Vacuum Arc Thruster (MVAT)'. In: *29th Int. Electr. Propuls. Conf. Princet. Univ.*

Tsiolkovsky, K. E. (1903). 'The Exploration of Cosmic Space by Means of Rocket Devices'. In: *Sp. Rev.* 5.

Velicu, I. L. et al. (2021). 'New concept of metal ion thruster based on pulsed thermionic vacuum arc discharge'. In: *Plasma Sources Sci. Technol.* 30.1, p. 015006. ISSN: 0963-0252. DOI: 10.1088/1361-6595/ABD0DD.

White, M. A. (2018). *Physical properties of materials*. 3rd ed. CRC Press, p. 496. ISBN: 9781138605107.

Xia, Q. et al. (2019). 'The influence of external magnetic field on the plume of vacuum arc thruster'. In: *Acta Astronaut.* 164, pp. 69–76. ISSN: 0094-5765. DOI: 10.1016/J.ACTAASTRO.2019.07.015.

Yang, W. et al. (2021). 'The role of double ionization on the generation of doubly charged ions in copper vacuum arcs: insight from particle-in-cell/direct simulation Monte Carlo methods'. In: arXiv: 2109.00214.

Zhang, J. (2020). 'Modern Monte Carlo Methods for Efficient Uncertainty Quantification and Propagation: A Survey'. In: arXiv: 2011.00680v1.

Zhuang, T., A. Shashurin, L. Brieda et al. (2009). *Development of Micro-Vacuum Arc Thruster with Extended Lifetime*. Tech. rep. Ann Arbor, Michigan: University of Michigan.

Zhuang, T., A. Shashurin, T. Denz et al. (2009). *Micro-Vacuum Arc Thruster with Extended Lifetime*. Tech. rep.